THE SYNTHESIS AND APPLICATIONS OF BORON NITRIDE NANOTUBES AND HEXAGONAL BORON NITRIDES AS NANOCARRIERS AND THERAPEUTIC AGENTS

by
Melis Emanet

Submitted to Graduate School of Natural and Applied Sciences
in Partial Fulfillment of the Requirements
for the Degree of Doctor of Philosophy in
Biotechnology

Yeditepe University
2019

THE SYNTHESIS AND APPLICATIONS OF BORON NITRIDE NANOTUBES AND HEXAGONAL BORON NITRIDES AS NANOCARRIERS AND THERAPEUTIC AGENTS

APPROVED BY:

Prof. Dr. Mustafa Çulha
(Thesis Supervisor) .....

Assoc. Prof. Dr. Gözde İnce .....

Assoc. Prof. Dr. Kaan Keçeci .....

Assist. Prof. Dr. Gülengül Duman .....

Assist. Prof. Dr. Hüseyin Çimen .....

DATE OF APPROVAL: ..../..../2019

Dedicated to my little hearth ***Miço***
left an immense love in our hearth…

ACKNOWLEDGEMENTS

First of all, I would like to thank my supervisor Prof. Dr. Mustafa Çulha to gave me opportunity to be a part of exciting projects (Project No: 112M480) COST Actions (Project No: 214Z129) founded by TUBITAK. He has been a great advisor for me to learn robust and patient in the way of my goals.

I am also grateful to my thesis monitoring committee members Dr. Gülengül Duman and Assoc. Prof. Dr. Kaan Keçeci for their constructive comments and promising ideas which made great contributions to my thesis.

I also separated an individual paragraph to my dear collaborators Özlem Şen and Melike Belenli. We have grown up together in the challenging conditions of scientific world with an always brilliant idea against problems we faced and with an endless fun even in the most difficult days. They are one of the most important achievement of mine that I gained in these six years.

I also thank to my collaborator Mine Altunbek who has a great contribution in my improving period at the beginning of my PhD program. I also thank to my other collaborators Zehra Çobandede and Şaban Kalay we spend very joyful working hours and we wrote many good articles together.

I am also grateful to my beloved love Gianni Ciofani. I always feel his constant support behind of me that encouraged me to play a role in scientific world not only with his professionality in work life but also his love filling my hearth. He deserves armful thanks for his numberless contributions to my thesis together with his both patience and scientific ideas.

Moreover, I also give my greater thanks to my big family including my beloved sister Merve Emanet, my parents Müzeyyen and Süleyman Emanet, my sweet grandmother Havva Bagana, with his innovative idea's uncle Muharrem Bagana, my cousin Elif Bagana Akın and uncle Ahmet Emanet. I also would like to thank to my other sweet grandmother Fatma Emanet who cannot be with us anymore but her love always in our hearts. Then, I am also

thankful to my new family Daniela Busco, Giuseppe Ciofani and uncle Mirco Busco who always show their supports and love. I made what I could with all your endless patience and compassions.

Lastly, I would like to send my kisses to my little hearth Miço whose place cannot be filled in my hearth. I am also grateful to him for the wonderful days with him left in the past.

ABSTRACT

THE SYNTHESIS AND APPLICATIONS OF BORON NITRIDE NANOTUBES AND HEXAGONAL BORON NITRIDES AS NANOCARRIERS AND THERAPEUTIC AGENTS

In recent years, boron-based nanomaterials, boron nitride nanotubes and hexagonal boron nitrides (BNNTs and hBNs) have gained significant interest for their use in medical and biomedical fields owing to their nanometer size and unique physicochemical properties including biocompatibility, high mechanical strength and chemical stability. These properties make them particularly suitable nanomaterials for their interaction with biomacromolecules and variety of successful biomedical applications. This thesis aims at addressing drug carrying and therapeutic effects of BNNTs and hBNs.

Considering their potential applications as drug carriers and therapeutic agents, the route of their interaction with biological environment should be understood at cellular level. Their biocompatibility evaluation revealed that the BNNTs and hBNs are good candidates for medical applications with their non-toxic nature on healthy cells even at relatively high concentrations. In an attempt to use the BNNTs and hBNs as drug carriers, they were modified with doxorubicin (Dox) and folate through nonspecific interactions. Folate was used to increase cellular uptake of BNNT by targeting folate receptors on the cell surface. It was found that the Dox conjugated BNNTs behave as the free Dox molecules while folate conjugation significantly enhanced (2 fold) cancerous cellular uptake. A purer and catalyst free hBNs batch was synthesized to use in the studies. Then, the hBNs were evaluated for their carrier and therapeutic effects. The data obtained from in vitro studies revealed that the level of reactive oxygen species (ROS) in the hBN exposed prostate cancer cells increased 62 per cent, cell death toward apoptosis was 4-fold enhanced and metastasis capacity of cells reduced significantly. These results envision the exploitation of hBNs as therapeutic agents against prostate cancer and pave the way to carry out *in vivo* studies to disclose their potential as drug carrier and therapeutic agents in cancer treatment.

ÖZET

BOR NİTRÜR NANOTÜP VE HEXAGONAL BOR NİTRÜRLERİN SENTEZİ, NANOTAŞIYICI VE TEDAVİ AMAÇLI UYGULAMALARI

Bor bazlı nanomateryallerden bor nitrür nanotüpler (BNNT'ler) ve hexagonal bor nitrürler (hBN'ler) küçük boyutları, eşsiz fizikokimyasal yapıları ve biyouygunlukları, yüksek mekanik ve kimyasal dayanıklılıkları sayesinde son yıllarda tıp ve biyomedikal alanlarında ilgi çeken yapılar olmuşlardır. Bu özellikleri BNNT ve hBN'leri özellikle biyomakromoleküllerle etkileşimde uygun yapılar haline getirmektedir. Tez kapsamında, BNNT ve hBN'lerin ilaç taşıyıcı ve terapötik ajan olarak araştırılması amaçlanmıştır.

İlaç taşıyıcı ve terapötik amaçlı kullanımları göz önüne alınarak, biyolojik uygulamaları amaçlanan BNNT ve hBN'lerin biyolojik çevre ile olan etkileşimleri hücresel boyutta açıklığa kavuşturulmalıdır. Yüksek konsantrasyondaki uygulamalarına rağmen sağlıklı hücrelerde biyouygun etki göstermeleri BNNT ve hBN'lerin biyomedikal alanda kullanımları için uygun yapılar olduğunu göstermektedir. BNNT ve hBN'lerin ilaç taşıyıcı ajan olarak değerlendirildiği çalışmada, yapılar doxorubisin (Dox) ve folat ile hidrofobik olarak etkileştirilmiştir. Kanser hücre yüzeyindeki artırılmış folat reseptörleri nedeniyle kanser hücresini hedeflemek amacıyla yapı folat ile etkileştirilmiştir. Çalışmanın sonucunda Dox ile etkileştirilmiş BNNT'lerin serbest Dox molekülleri ile aynı oranda etki ettiğini fakat folat sayesinde hücresel alımının iki kat arttığı görülmüştür. Sonraki kısımlarda ise temiz bir sentez yöntemi olarak katalizör kullanılmadan sentezlenen hBN'ler ile çalışmalara devam ettik. Çalışmanın ikinci kısmında, reaksiyon ortamında katalizör kullanılmadan sentezlenen hBN'lerin taşıyıcı ve terapötik etkileri incelenmiştir. Elde edilen sonuçlarda, hBN ile muamele edilen prostat kanser hücrelerinde reaktif oksijen türlerinin (ROT) yüzde 62 oranında arttığı, apoptoziz ile hücre ölümlerinin 4 kat arttığı ve hücrelerin metastaz kapasitelerinin önemli ölçüde azaldığı görülmüştür. Bu sonuçlar hBN'lerin prostat kanserinin tedavisinde terapötik ajan olarak öngörülmesinde cesaretlendirici olmaktadır. Bu gelecek vadeden sonuçlar hBN'lerin kanser tedavisinde ilaç taşıyıcı ve terapötik ajan olarak çalışmalarını *in vivo* evreye taşınmasında bizleri cesaretlendirmektedir.

TABLE OF CONTENTS

LIST OF FIGURES

LIST OF TABLES

LIST OF SYMBOLS/ABBREVIATIONS

ºC	Degrees Celsius
cm^{-1}	Wavenumber
ml	Milliliter
nm	Nanometer
µL	Microliter
µM	Micromolar
µm	Micrometer
3T3-L1	Mouse adipocyte-like cell line
A549	Human adenocarcinomic alveolar basal epithelial cell line
Ag	Silver
Al	Aluminum
Al_2O_3	Aluminum oxide
As	Arsenic
B	Boron
BA	Boric acid
BBB	Blood-brain barrier
BCA	Bicinchoninic acid assay
BNCT	Boron neutron capture therapy
BPA	Boronophenylalanine
BSH	Sodium borocaptate
Ca	Calcium
CaF_2	Calcium fluoride
Cd	Cadmium
CED	Convection enhanced diffusion
CH	Chitosan
CNS	Central nervous system
CNT	Carbon nanotubes

CO_2	Carbon dioxide
Cu	Copper
CT	Computed tomography
CVD	Chemical vapor deposition
DAPI	4',6-Diamidino-2-Phenylindole, Dihydrochloride
DCF	2′,7′–dichlorofluorescein
ddH_2O	Double distilled water
DLS	Dynamic light scattering
DMEM	Dulbecco's Modified Eagle's Medium
DNA	Deoxyribonucleic acid
Dox	Doxorubicin
DU145	Human androgen independent prostate cancer cell line
EDTA	Ethylenediaminetetraacetic acid
EGF	Epidermal growth factor
EGFR	Epidermal growth factor receptor
FBS	Fetal bovine serum
Fe	Iron
Fe_3O_4	Iron oxide
FITC	Fluorescein isothiocyanate
FTIR	Fourier transform infrared
GA	Glucosamine
GBM	Human glioblastoma multiforme cell line
GC	Glycol chitosan
H_2O_2	Hydrogen peroxide
HDF	Human dermal fibroblast cell line
He	Helium
HEK293	Human embryonic kidney cell line
HER2	Human epidermal growth factor receptor 2
HNO_3	Nitric acid
HRTEM	High-resolution transmission electron microscopy
ICP-MS	Inductively coupled plasma mass spectrometry
LbL	Layer by layer
LET	Linear energy transfer

Li	Lithium
LMS	Lysosome mimicking solution
LNCaP	Human androgen dependent prostate cancer cell line
mAb	Monoclonal antibody
MCF-7	Human breast cancer cell line
MET	Metastatic melanoma
MoO_3	Molybdenum trioxide
MR	Magnetic resonance
MRC-5	Human fibroblast cell line
MWBNNT	Multi-walled boron nitride nanotube
MWCNT	Multi-walled carbon nanotube
N	Nitrogen
NaCl	Sodium chloride
$NaGdF_4$:Eu	Gadolinium fluoride
NH_3	Ammonia
Ni	Nickel
PBS	Phosphate buffer saline
PC3	Human androgen independent prostate cancer cell line
PEG	Polyethilene glycol
PEI	Polyethylenimine
PI	Propidium iodide
PLGA	Poly(lactic-co-glycolic acid)
PLL	Poly-L-lysine
PNT1A	Human prostate cell line
PSA	Penicillin-Streptomycin
PSMA	Prostate specific membrane antigen
PSS	Poly(styrenesulfonate)
RAW-264	Mouse leukemic monocyte-macrophage cell line
RES	Reticuloendothelial system
Rho123	Rhodamine 123
RNA	Ribonucleic acid
RNase	Ribonuclease
ROS	Reactive oxygen species

RunX	Runt-Related Transcription Factor
SEM	Scanning electron microscopy
SH-SY5Y	Human neuroblastoma cell line
Sr	Strontium
SWBNNT	Single-walled boron nitride nanotube
SWCNT	Single-walled carbon nanotube
T98	Human glioblastoma cell line
TEM	Transmission electron microscopy
TfR	Transferrin
TGA	Thermogravimetric analysis
TNM	Tumor node metastasis
Tris-HCl	Tris hydrochloride
U87MG	Human glioblastoma cell line
UV/Vis	Ultraviolet/Visible
WST-1	Water-soluble tetrazolium-1
YPD	Yeast extract peptone dextrose medium
Zn	Zinc
ZnO	Zinc oxide

1. INTRODUCTION

1.1. DRUG DELIVERY APPROACHES AGAINST CANCER

In recent years, scientists are diligently working to find an effective drug delivery method to target cancerous tissues. Several drug administration routes are established including intranasal [1], intra-arterial [2] intrathecal [3] and intraventricular drug administration [4] and intra-tumoral delivery [5]. Moreover, several drug delivery approaches including passive diffusion [6] carrier-mediated [7], receptor-mediated [8] and adsorption-mediated transport [9], and disruption of the barriers including blood brain barrier (BBB) and blood testis barrier (BTB) [10, 11] are established for accumulation of drugs in tumors as shown in Figure 1.1. The clinical trials by using intra-arterial, intrathecal and intraventricular drug administration show minimal improvement in terms of drug delivery effectiveness apart from the intra-arterial injection of monoclonal antibodies, where successful trials have been achieved [12,13]. Further, the convection enhanced diffusion (CED) technique, an intratumoral delivery approach, is explored to increase the effective infiltration of drug into tumor region [14]. Microdialysis is another example of intratumoral drug delivery method, where drugs passively diffuse to the tumor tissue so exposing the tumor to enough drug compounds [15].

Another drug delivery technique is the modification of the drug molecules with small sized (smaller than 500 Da), low charged (should have low hydrogen binding capacity), and high lipophilic compound, to make them more appropriate for accumulation in tumor [16]. Additionally, the drugs are modified as analogue of the ligands that are specific for the receptor present on the tumor cells surface for adequate drug accumulation in the tumor tissue [17]. For example, transferrin receptor mediated endocytosis is an efficient technique for passing drugs through the BBB. Due to the localization of transferrin receptors on the endothelial cell in BBB and overexpression at tumor cells provide selective uptake of transferrin functionalized structure by brain cancer cells [18]. Therefore, a number of nanoparticles were functionalized with transferrin for passing through the BBB such as solid lipid nanoparticles [19], dendrimers, polymeric nanoparticles [20].

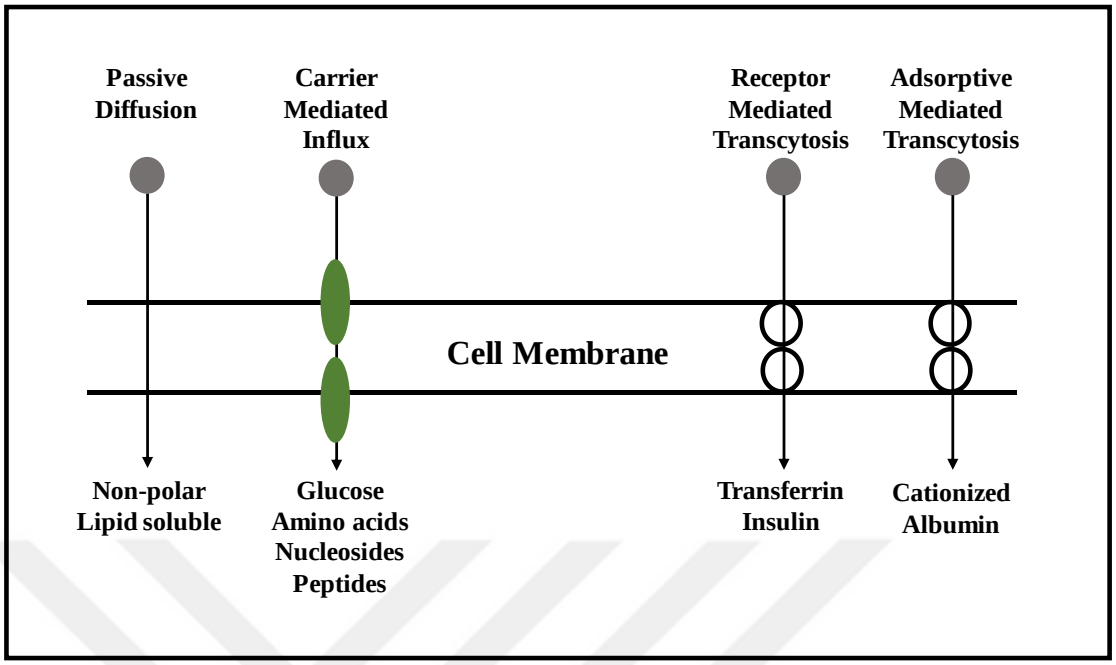

Figure 1.1. Passive diffusion, carrier-mediated, receptor-mediated and adsorptive-mediated transport pathways through the cancer cell membrane.

The cytotoxicity and genotoxicity of drugs used in cancer therapy is also a major obstacle causing unbearable side effects in patients [21]. One of the most commonly cancer-inhibiting strategy is preventing the cell proliferation by cytotoxic drug such as maytansine that displays antimitotic activity. With a highly cytotoxic nature, maytansine has been functionalized with cancer cell specific antibodies providing high target-specific cytotoxicity in cancer cells at *in vitro* studies [22].

The intervention of drugs such as doxorubicin (Dox) and epirubicin with the DNA replication process occurs either with their direct intercalation into the DNA helix or inhibition of DNA replication enzymes such as topoisomerase, which leads to apoptosis in cancer cells [23,24]. Several intelligently designed cytotoxic and genotoxic agents serve the purpose as single or complex therapies to fight against cancer. However, the limited delivery of the drugs to cancerous cells is an obstacle for the effective use of these drugs due to low accumulation of the drugs below efficient doses in cancerous cells. Therefore, effective targeting and delivery of toxic cancer drugs is a critical matter in their clinical applications.

In recent years, nanomaterials have gained significant interest in the medical and biomedical fields, owing to their small size and unique chemical and physical properties, including their

intrinsic optical, magnetic, electronic and mechanical features, often different from the bulk material counterparts [25]. These properties make them particularly suitable for interaction with biological molecules, and thus successful for many biomedical applications, including medical imaging, diagnosis, drug delivery, and tissue engineering [26].

The nanomaterials are widely investigated for efficient drug delivery strategies [27]. In this context, nanomaterials are generally developed as colloidal carriers that consist of liposomes, polymeric nanoparticles, solid lipid nanoparticles, polymeric micelles, dendrimers or ceramic nanoparticles [28-34]. These nano-systems generally use passive diffusion [35] through the cancer cell membrane as well as receptor mediated [36] and adsorptive [37] transcytosis processes.

These nanocarriers can also be decorated with targeting agents such as folate, HER2 and EGFR antibodies for specific cancer cell targeting. The designed systems have a high potential to eliminate side effects of the drugs, but also to increase their efficiency [38, 39]. In a study, radio-labeled carbon nanotubes (CNTs) were functionalized with amino groups for targeting cancer cell membrane and the system was tested on BBB model consisting of brain endothelial cells, and in *in vivo* experiments. The results of the experiments showed that the functionalized CNTs with the brain targeting ligands can be used as drug delivery agent to the brain [40]. Moreover, Ciofani et al. developed a transferrin functionalized boron nitride nanotubes (BNNTs) as a model structure for BBB targeting as shown in Figure 1.2 [41].

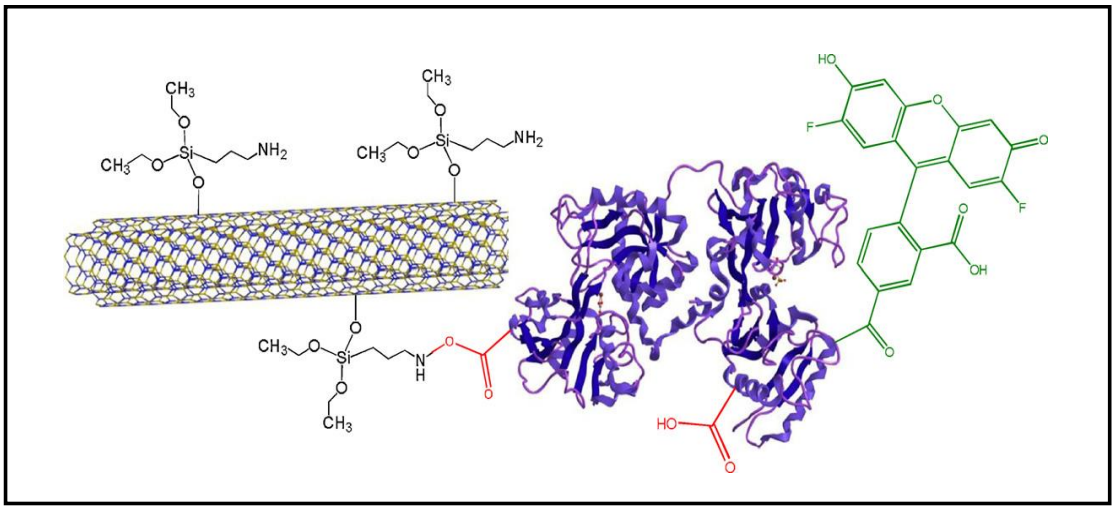

Figure 1.2. Graphical schematization of a TfR-BNNTs [41].

In a study, Dox was complexed with CNTs through π-π stacking following the functionalization with PEG to increase their blood circulation time and to decrease their toxicity [42]. It was found that the PEG–Dox–CNTs accumulated more in Raji lymphoma xenograft tumors of SCID mice compared with free dox. In another study, single walled CNTs were functionalized with Dox, a monoclonal antibody for targeting and a fluorescence marker for visualization [32]. The results indicated that cancer cells efficiently took up the complex. While Dox was effectively released and accumulated in the nucleus, the CNTs remained in the cytoplasm. This result indicates that the high loading capacity of the CNTs is due to its large surface area and effective noncovalent interaction between CNTs and drug molecules. However, the relatively low biocompatibility of CNTs required PEG functionalization but coating with PEG did not completely eliminate its toxicity [43]. Furthermore, another type of tubular nanostructures, halloysite clays nanotubes (HNTs), have been shown to be good candidates for nanoarchitectural composites due to their biocompatible nature. The inner lumen of HNTs can be loaded with drugs or proteins [44]. BNNTs were also tested for their delivery potential following functionalization with folate molecules, which showed promising results for imaging and drug targeting applications [45]. The results of the study indicated that the folate was a good candidate to target BNNTs to cancer cells allowing a selective internalization of the BNNT–folate complex by the cancer cells through overexpressed folate receptors on cancer cell plasma membrane [45,46].

Consequently, a wide variety of approaches for effective drug administration in tumor region have been developed. Despite the drug targeting efficiency has been enhanced with the new generation drug delivery approaches, it is still not enough to face with the detrimental effects of brain tumors.

1.1.1. Drug Delivery Approaches in Glioblastoma Multiforme (GBM)

Among the brain cancers, glioblastoma multiforme is the most common type, the most aggressive and lethal, characterized by extensive infiltration into the brain parenchyma. GBM is a tumor of the glia, a group of cells that protect and support neurons in central nervous system. GBM belongs to a group of brain tumors known as astrocytomas, as shown in Figure 1.3. According to the World Health Organization (WHO) criteria, astrocytomas

are classified into four grades (grades I, II, III and IV) based on their histopathological features. GBM is the highest grade astrocytomas, because of the features of this tumor, including cell necrosis localization, presence of hyperplastic blood vessels and highly pleomorphic cell nuclei showing a high proliferation index [47].

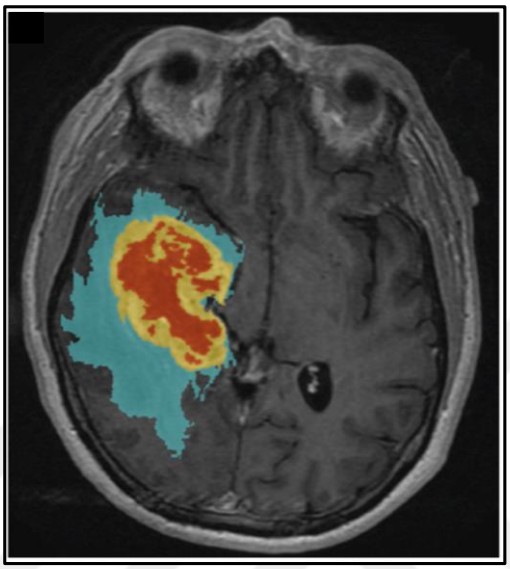

Figure 1.3. MRI image of grade IV glioblastoma multiforme cancer [48].

Despite the cause of the disease is not entirely clear, uncommon risk factors include genetic disorders such as neurofibromatosis, Li Fraumeni syndrome and previous radiation therapies [49]. Its diagnosis can be performed by computed tomography scanning (CT), magnetic resonance scanning (MR) and tissue biopsy [50]. The standard treatments of the GBM include the removal of tumor tissue by surgery and, after that, various chemotherapy and radiotherapy administration to the tumor region [51]. However, all the traditional therapy approaches to the GBM present extremely poor success: the average survival time following diagnosis of GBM is only 12 months; furthermore, the 3-year survival rate of GBM is about 3-5 per cent [52]. Despite the dramatic efforts to develop diagnostic and therapeutic tools, the treatment of GBM remains a huge challenge in neuro-oncology, and successful treatments are still far from being attained. The major obstacles include i) the structural complexity of the central nervous system (CNS), ii) the heterogeneous and invasive nature of the tumor, iii) the difficulty of identifying tumor margins and the disseminated tumor burdens during surgical resection, iv) the insufficient accumulation of therapeutic agents at

the disease site, v) the recurrence of the pathology, and vi) the acquired drug resistance during chemotherapy [53].

The radiotherapy for treatment of GBM has been a standard approach for thirty years [54]. It is also common to combine the radio therapy with surgery, chemotherapy, hormone therapy and immunotherapy [55]. In general, after removal of the tumor mass with surgery, the radiotherapy to the tumor region shows significant benefits as compared to the patients who are not treated with radiotherapy [56]. In the mechanism of radiotherapy, the cancerous cells in tumor are exposed to radiation that exploits oxygen in the organism as radiosensitizer to produce reactive oxygen species and thus to damage DNA structure in the cells [57]. As result of the irreparable damages in the DNA structure, the growth of the tumor can be slowed down by killing cancer cells. In this technique, shaped radiation beams are used to direct the radiation from several angles to the tumor region in the body to enhance the therapy yield and to decrease the radiation exposure of normal healthy tissues to prevent their damage [58]. The combination of radiotherapy with nitrosourea-based chemotherapy or temozolomide-based chemotherapy shows certain benefits, showing 7.259 patients a 14.2-month average survival rate relative to standard radiotherapy alone, in which 6.673 patients showed a 12-month average survival rate [59]. The nitrosourea and temozolomide are used as chemotherapy drugs owing to their DNA alkylation tendency [60]. Due to their lipophilic nature, they are useful for treatment of GBM, given that they can penetrate through the blood-brain barrier (BBB) freely. [61,62]. Despite a relative success of all these therapies, advantages with respect to plain radiotherapy are still small and remain poor in terms of long-term survival [63]. In this regard, boron neutron capture therapy (BNCT) presents great hope in the treatment of GBM [64].

1.1.2. Drug Delivery Approaches in Prostate Cancer

Prostate cancer is one of the most detrimental form of cancer in men. Statistical analysis show that the 1.9 million men is suffering from prostate cancer and unfortunately 6.7 million men died in 2012 in worldwide [65]. It is the most commonly seen solid organ tumor in Turkey and one of each twelve men is suffering from this illness [66]. The risk factors that increase the possibility to catch prostate cancer are family history and presence of lower urinary tract syndromes [67]. The basic diagnosis methods of the prostate cancer are

searching serum prostate specific antigen (PSA) level in blood, echography, and biopsy [68]. The UICC 2002 Tumor Node Metastasis (TNM) used a classification system to grade the prostate cancer based on extent of the primary tumor and its metastasis extent in lymph nodes [69]. Initial treatment techniques are prostatectomy and radiation therapy to remove or destroy the tumor when it is already in prostate capsule [70]. When the tumor is still inside the prostate capsule, it indicates the first grades of cancer. In this grade, it produces androgen that induces cell proliferation as well as inhibition of apoptosis [71]. Accordingly, key point of the therapy is ablation of the androgen that prevents tumor progression and causes regression of prostate tumor [72]. However, it cannot generally be cured in these grades and diagnosed after cancer spread from prostate capsule. In high grades of the illness, prostate cancer cells make metastasis to other tissues including bone and lymph nodes [73]. It becomes less controllable and more aggressive due to the androgen independency. It is the lethal form of the prostate cancer due to the lack of efficient treatment method in the literature.

Androgen dependent grade of the prostate cancer therapy is more determined that androgen ablation to control tumor growth and then tumor removing by surgery [74]. However, therapy at the androgen independent grade of prostate cancer is more complicated and difficult as shown in Figure 1.4. Therapy is developed depends on the metastasis region of cancer and differentiation of cells from their origin to target prostate specific antigens [75]. Therefore, more powerful and smart anti-cancer agents, carrying and targeting systems are required like nanodrugs including polymeric [76], dendrimeric [77], metallic [78] or lipid-based [79] drugs. Polymeric nanoparticles are good candidates as a carrying agent since their controlled drug release properties and surface modification capability [80]. In a study, paclitaxel loaded small poly(lactide-co-caprolactone-co-glycolide) (PLGA) nanoparticles, in 100 nm size, were used for controlled drug release in prostate cancer. They revealed that the structures were showed high intracellular activity in PC3 chemoresistan and hormone independent cells as compared to free paclitaxel drugs [81]. In another study, prostate specific membrane antigen (PSMA) targeted PLGA–poly (ethylene glycol) (PEG) polymers were used for controlled cisplatin drug release in LNCaP cells [82]. Moreover, metallic nanoparticles are also good candidates as drug carrying agents with their relatively biocompatible nature and easy functionalization with drugs and targeting agents [83]. Gold nanoparticles were developed as drug carrying agents by functionalization with androgen or

G protein receptor for hormone insensitive and chemotherapy resistant prostate cancer cells [84]. According to the promising results of nanodrugs on prostate cancer cells, they represent exploitable nanodrugs to test in *in vivo* applications. In another study, hollow boron nitrides (BN) were used as boron reservoir to fight against prostate cancer. The result indicated that the degradation products of BNs decreased the cell viability and stimulated the cell death by apoptosis. Moreover, promising results were obtained from in vivo anti-cancer studies of the BNs against prostate cancer [85].

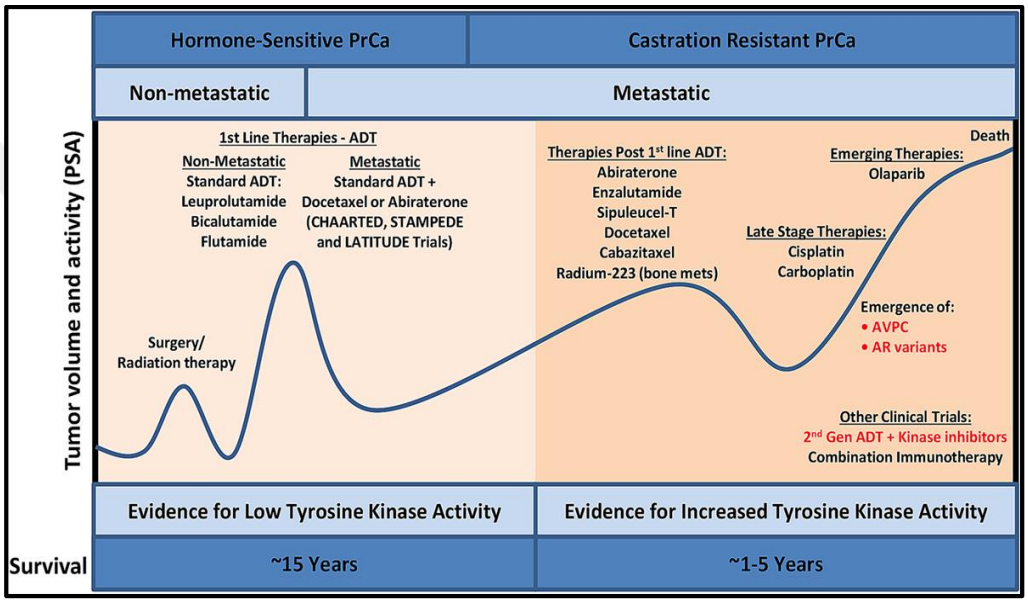

Figure 1.4. Schematic representation of prostate cancer therapies [86].

1.2. BORON-BASED THERAPEUTIC APPROACHES

Boron has been known as an essential element for life cycle (growth, development and maturation) of organisms in all phylogenetic kingdoms [87]. Boric acid, as a chemical form of boron in physiological conditions, has tendency to make an ester bonds with the hydroxyl groups of organic compounds [88]. Therefore, hydroxyl group including structures such as sugars are good candidates to internalize into their structures [89]. When the complexation performed with structurally and functionally important sugars such as ribose in adenosine or adenosine precursors cause adverse effects by affecting the presence or activity of the structure [90]. These biomolecules include diadenosine phosphates (signal nucleotide) and

S-adenosylmethionine that have high affinities to boric acid [91]. S-adenosylmethionine is generally used in methylation reactions that shows its interaction with boric acid affects the all functions of DNA, RNA, protein and phospholipids in cell structure [92].

A recent study has been performed with arthritic people fed with a diet including 6 mg/d boron supplement in form of calcium fructoborate for six weeks. After the process, 80 per cent of the people with mild or moderate osteoarthritis were reported having reduced or eliminated their painkiller drugs. Moreover, their joint rigidity disappeared, inflammation reduced, and movements significantly increased. In another study, the inflammation biomarkers were investigated on people whose diet was supplemented with 3, 6, 9 and 12 mg/d calcium fructoborate for 15 days. Then, it was realized that inflammatory biomarkers including serum C-reactive protein, plasma fibrinogen and erythrocyte sedimentation rate were significantly improved [93].

In another study effects of boron on bone formation was investigated with *in vitro* studies. The cells that were exposed to 1 and 10 ng/mL of boric acid showed improved bone formation, increased mRNA profile of type 1 collagen, osteopontin, bone sialoprotein, osteocalcin, and RunX as compared to controls [94].

Another finding showed that boric acid-exposed people exhibited improved central nervous system psychomotor skills, like processes of attention and short-term memory [95]. Furthermore, several studies indicated positive effects of boric acid on hormonal regulation of the organisms including vitamin D, estrogen, thyroid hormone, insulin, and progesterone production [96-98].

Boron-including agents such as calcium fructoborate, borax, boric acid, boronic acid and their esters were also studied in plenty of investigations of prostate cancer treatment [99]. These studies show that boron-including agents has remarkable inhibiting effects on prostate cancer proliferation [100,101]. In a study, it was indicated that the boric acid decreased proliferation of the cells by manipulating Ca^{2+} release to the cytosol, which is proliferation stimulant, and cell migration by inhibiting F-actin polymerization in cytoskeleton [102]. In another study, it was shown that the calcium fructoborate induces increased calcitriol level in the blood that activates apoptosis and inhibits angiogenesis, invasion and metastasis of breast cancer cells [93]. Moreover, boronic acids as trivalent boron including agents that has alkyl group in place of hydroxyl group in its structure plays very important role in cancer

treatment. Phenylboronic acid and diphenylboronic esters as boronic acid samples are more effective on prostate cancer cell proliferation and migration thanks to their structure that mimics organic compounds [103].

Boron neutron capture therapy is a therapeutic application exploited to selectively destroy cancer cells, and it is based on nuclear capture and fission reaction of the ^{10}B isotope that is in its nonradioactive form in nature. It is irradiated with low energy thermal neutrons to yield high linear energy transfer (LET) of alpha particles (^{4}He) and recoiling ^{7}Li nuclei [104] as shown in Figure 1.5.

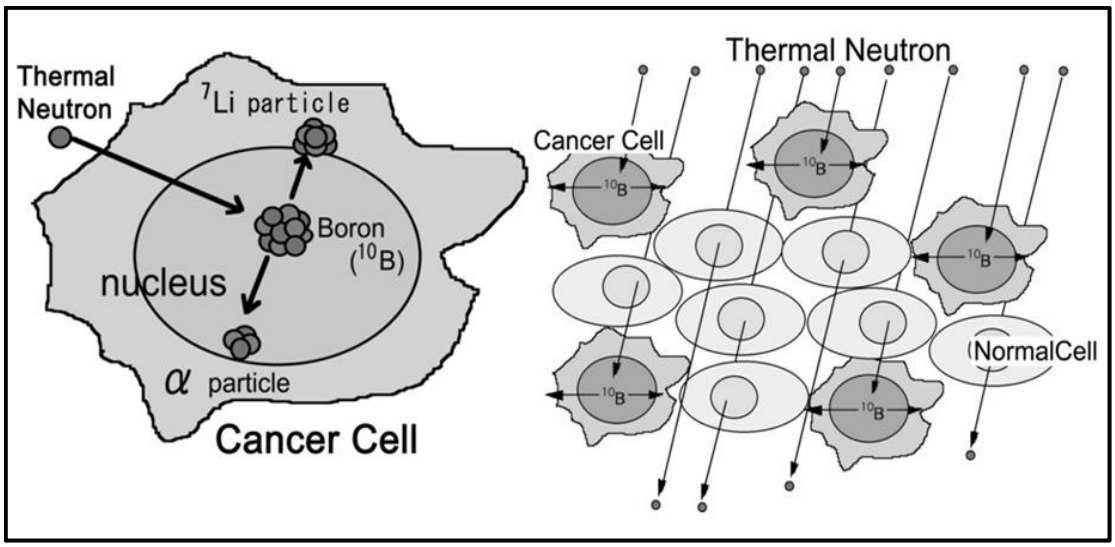

Figure 1.5. The principle of boron neutron capture therapy [105].

Treatments with BNCT technique have been first explored in Japan, Europe and United States [106]. Clinical trials with BNCT have primarily focused on the high grade GBM and cerebral metastasis of melanoma (MET) that are most common malignant brain tumors [107]. The treatments first consist of de-bulking surgery to remove tumor masses as fully as possible, followed by BNCT treatments at different times after surgery. The clinical potential of the BNCT was theoretically realized in 1930s [108], and first successful outcomes have been obtained during the 1950s [109]. However, given the disappointing outcomes of the trials, experiments were stopped in 1961 [110]. The main problems were a) inadequately targeting of inorganic boron-including agents to the cancer tissue b) limited penetration of the thermal neutrons and c) accumulation of boron-including agents in normal brain vasculature that cause damages of scalp and vascular system [111].

The most important requirements of a boron-delivery agent are: low systemic toxicity, high tumor and brain/normal tissue uptake ratio, high tumor concentration of ^{10}B/g tumor, rapid clearance from blood and normal tissue, and persistency in tumor during the BCNT application process [112]. However, new chemical synthetic techniques, new biological and biochemical knowledge were exploited to develop more effective boron-including agents [113]. The biggest challenge in their development is the requirement of an effective targeting of the tumor tissue [114]. Further, the targeting of the glioblastoma is an even bigger challenge compared to the malignancies of other tissues, due to its highly infiltrative and histologically complex nature [115].

In the clinical trials of the BNCT, boric acid (BA) was used as boron-including agent between 1950-1960 [109], as a first-generation compound. This simple chemical compound was not selective, showing low tumor retention. Then, in 1960s two other low molecular weight boron compounds were exploited, which are (L)-4-dihydroxy-borylphenylalanine (BPA) and another one based on a newly discovered polyhedral borane anion [116], sodium mercaptoundecahydro-closo-dodecaborate (BSH) [117] (Figure 1.6). These second-generation boron-including compounds were low toxic and showed high persistency in tumor throughout the BNCT process.

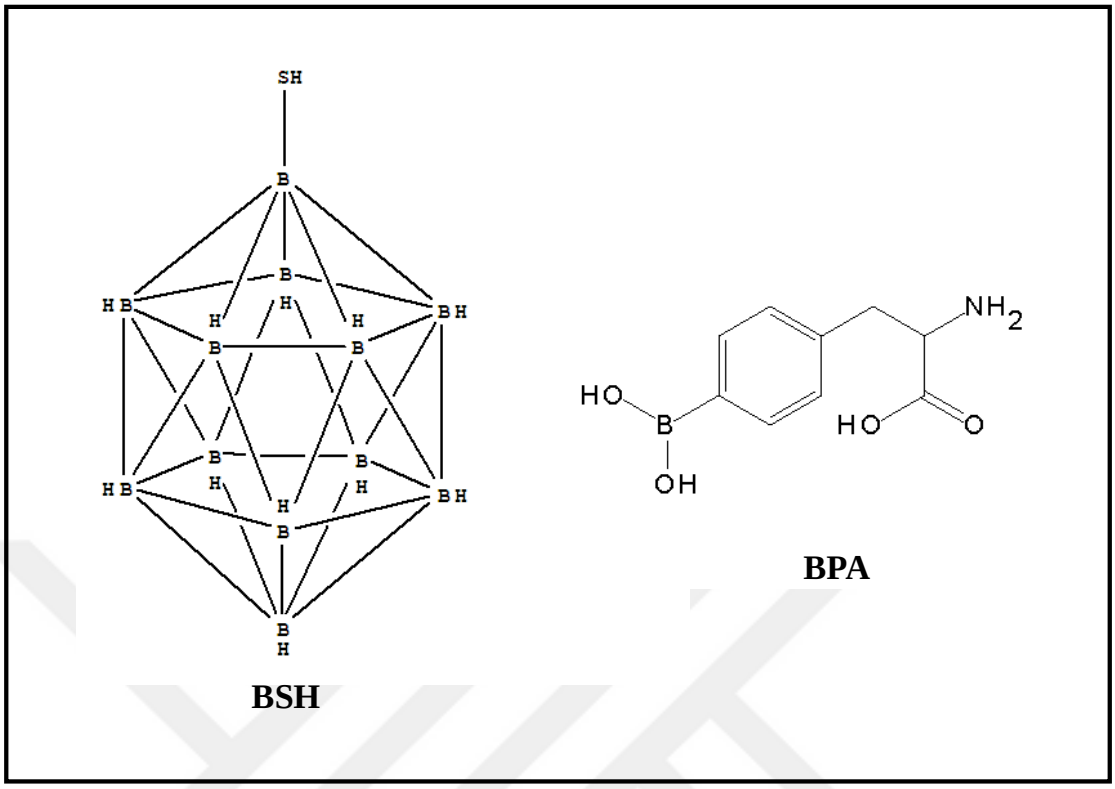

Figure 1.6. Chemical structure of BSH and BPA.

Then, clinical studies were carried out by Hatanaka in Japan in 1967 by using a thermal neutron beam and BSH [118]. In this treatment, first the tumor was removed as soon as possible with surgery, and thereafter BNCT was applied by the administration of BSH by a slow intra-arterial infusion, and then intravenously. After 12-14 h, BNCT was carried out with several nuclear reactors. Because the thermal neutrons have limited penetration depth through the tissue, it was obligation to remove the bone flap to increase the irradiation doses at the exposed tissue [119].

Then, Miyatake *et al.* have improved this technique by combined administration of BPA and BSH intravenously for 12 h. 11 patients with high-grade gliomas were treated with this approach. The MRI and CT results of their tumor showed a 17 per cent to 51 per cent reduction respect to the initial volume after the treatment. The tumor volume reduction reached a maximum of 30 per cent to 88 per cent in the following trials [120].

In 1994, higher energy epithermal neutron beams were used instead of low-energy thermal neutron irradiation, thus eliminating the needing to remove the bone flap step before the

treatment [121]. This eliminates the damage in the scalp structure and permits the treatment of the cancer area in the brain [122].

Although the compounds were safe for normal tissues, they were not ideal as boron delivery agent. Thus, a third-generation of boron-containing compounds was designed, which are combination of low molecular weight molecules and monoclonal antibodies (mAb) [123]. For example, the epidermal growth factor (EGF) and transferrin (TfR) receptors that are overexpressed in glioma tumor cells were chosen to exploit specific ligands bonded to boron-including agents [124,125].

In order to be successful in BNCT, sufficient amount of ^{10}B should reach to the tumor cells ($\sim 10^9$ atoms/cell), and enough thermal neutrons must be absorbed to sustain a lethal $^{10}B(n,\alpha)^7Li$ capture reaction. Thus, depending on the success of cancer tissue targeting and overcoming, the BNCT can be considered as a safe and effective treatment technique.

1.3. BORON NITRIDE-BASED NANOMATERIALS

1.3.1. Boron Nitride Nanotubes (BNNTs)

Boron nitride nanotubes (BNNTs) were first synthesized in 1995 by Chopra et al. [126] after the discovery of carbon nanotubes (CNTs) in 1991 by Iijima [127]. Due to the same honeycomb structures, BNNTs are regarded as structural analogues of CNTs as shown in Figure 1.7. There is a considerable charge transfer between B and N atom since their different electronegativity that cause partially ionic character [128]. This leads to van der Waals interactions between layers, that is the primary reason of difficulties in synthesizing single-walled BNNTs with respect to easy synthesizing techniques of single-walled CNTs [129]. Furthermore, the inherent characteristics of BNNTs are at the base of their intrinsic physical and chemical properties [130]. They are increasingly gaining attention because of their unique physicochemical features, including high resistance to oxidation and heating, constant electric properties, high hydrophobicity, and considerable hydrogen storage capacity. Consequently, they found plenty of applications in a wide range of research fields. [131]. In addition, BNNTs are considered as good candidates for a wide range of biomedical and related applications such as orthopedic implants [132], biosensing [133], and drug and gene delivery [134].

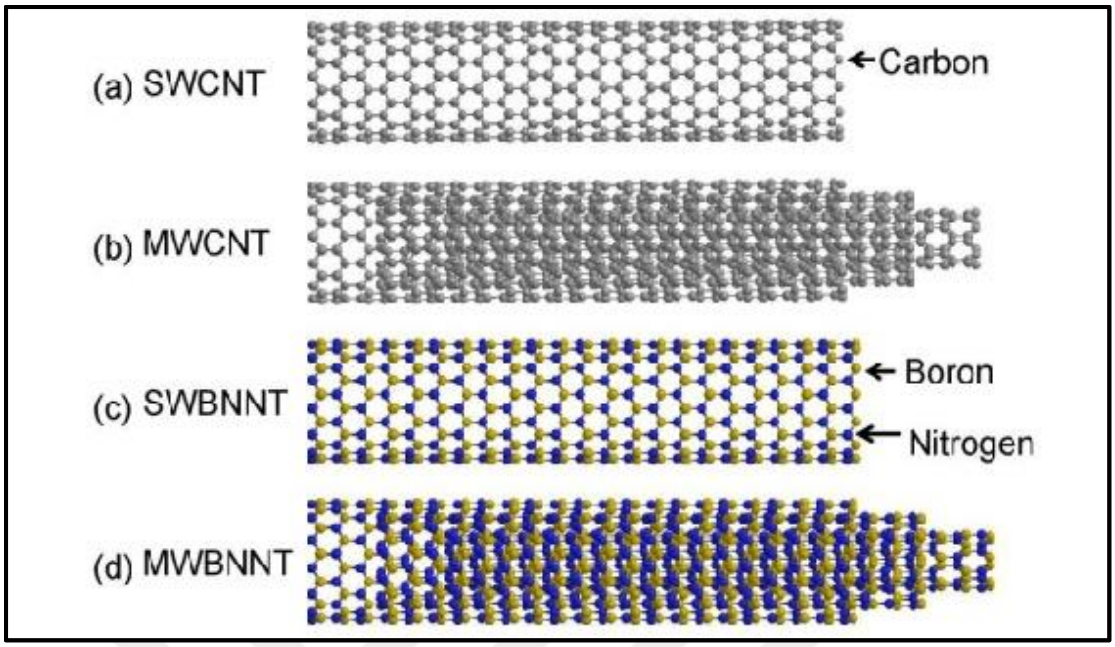

Figure 1.7. Molecular model of a SWCNT (a), MWCNT (b), SWBNNT (c) and MWBNNT (d) [135].

BNNTs were also investigated in a variety of applications as carrier or active agent to use in cancer treatments [136]. As carriers, BNNTs were functionalized with transferrin as a targeting ligand interacting with the overexpressed transferrin receptors on glioblastoma cancer cells. This study presents a fundamental step towards BNNT exploitation as smart and selective nanocarriers in several nanomedicine applications [137]. Then, BNNTs were functionalized as contrast agents to use in BNCT application. BNNTs were functionalized with DSPE-PEG_{2000} to increase their dispersibility in aqueous media. In this study, BNNTs-DSPE-PEG_{2000} accumulated in B16 melanoma cancer cells three times more than BSH, indicating that BNNTs-DSPE-PEG2000 would be a possible candidate as a boron delivery vehicle for BNCT [138]. In another study, BNNTs were also functionalized with poly-L-lysine (PLL) and folic acid for BNCT (Figure 1.8). PLL was wrapped around the BNNTs to induce more hydrophilic properties. In addition, BNNTs were coated with folic acid for selective interaction with the tumor cells. It was observed that PLL–F–BNNTs were effectively taken up by malignant glioblastoma cells, suggesting that the use of BNNTs should be further investigated for neutron capture therapy [139].

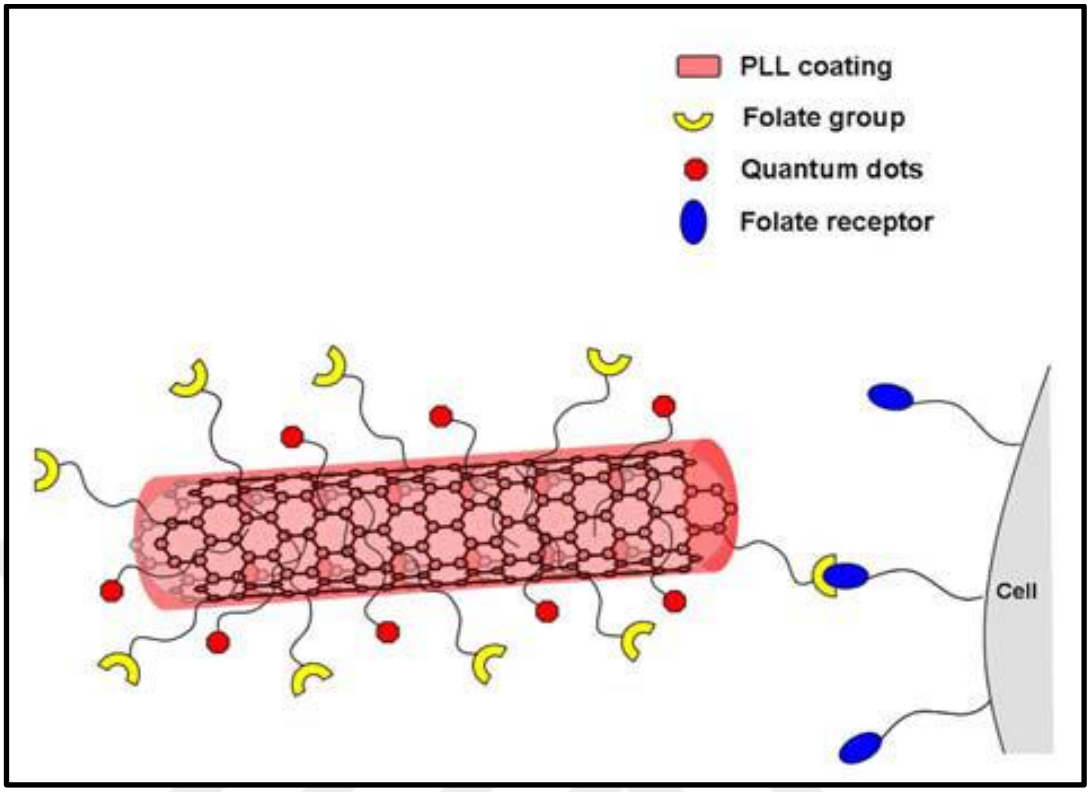

Figure 1.8. Schematic representation of the PLL–F–BNNTs nanovector [139].

1.3.1.1. BNNT Synthesis

There are several BNNT synthesis methods that vary depending on the boron precursors, catalysts, mode of heat, temperature, and duration of the process [140]. The differences in the process change the production yield, length, and size of the BNNTs. The BNNTs were first synthesized by arc discharge method, by which dark gray BNNTs were collected in approximately 3 nm inner diameter and 200 nm length [126]. An arc discharge is generated between a hexagonal BN (h-BN)-filled tungsten rod as an anode and a cooled copper electrode as cathode. In another method, due to the structural similarity between the CNTs and BNNTs, the latter were synthesized from CNTs by substitution reaction [141]. CNTs, B_2O_3 molecules as boron precursor, and MoO_3 as catalyst were used in this reaction. The only way to obtain single walled-BNNTs is laser ablation method [142]. Further, chemical vapor deposition (CVD) method is a well-known and economical method widely used for CNT and BNNT synthesis [143]. In this method, high production yield can be obtained and

requires simple experimental procedure. In recent studies, high production yield has been achieved by the CVD method using metal oxides such as ZnO, Al_2O_3, Fe_3O_4 and Fe_2O_3 as catalysts [144]. Besides, the ball milling is used to increase production yield by transferring high mechanical energy to boron and nitrogen precursors and to increase their surface area to increment their contact possibility [145]. In another study, the CVD technique was used in combination with the ball milling process: high yield of BNNTs of approximately 30 nm in diameter and 500-1000 nm in length were obtained [146].

1.3.1.2. Functionalization of BNNTs

The high chemical stability and hydrophobicity of BNNTs result into their poor dispersibility in aqueous media [147,148], which hinders their cellular uptake studies and reliable assessment of their adverse effects on living systems. The poor dispersibility limits their use in medical and biomedical applications. Therefore, significant efforts have been dedicated to increase their dispersions in physiological solutions and their interactions with other biomaterials. The water dispersibility of BNNTs can be increased basically by the insertion of –OH or $–NH_2$ groups at the edges and/or at defects of the structures [149]. This makes them suitable for further functionalization or more amenable for interactions with other biomaterials. Of course, the chemical and/or physical functionalization processes can affect the properties of the BNNTs, and appropriate biocompatibility investigations should be carried out after each functionalization step. Moreover, BNNTs have been physically kept in interaction with several biomolecules such as gum Arabic, glycine, mesoporous silica, and europium doped sodium gadolinium fluoride ($NaGdF_4$:Eu) for cellular uptake studies for biomedical applications including drug delivery and tissue engineering [150–153]. The functionalization provides high dispersibility in aqueous media and functional groups to visualize them by binding fluorescent dyes or quantum dots in fluorescence imaging studies [154,155].

1.3.1.3. Biocompatibility of BNNTs

The cytocompatibility of synthesized BNNTs and their interactions with living systems were first evaluated by Ciofani *et al.* In that study, polyethyleneimine (PEI) and quantum dots

were complexed with BNNTs, the latter being investigated on neuroblastoma SH-SY5Y cells for 72 h. The cellular uptake and cytotoxicity experiment results confirmed that PEI-BNNTs were completely cytocompatible structure. Moreover, the results indicated that the cellular uptake of the PEI-BNNTs was accomplished using energy-dependent classical endocytosis pathway, probably due to the chemical reactivity of PEI with cells [154]. Next, glycol–chitosan (GC) non-covalently coated BNNTs were used for the treatment of human neuroblastoma cells, that resulted viable up to 100 μg/mL of GC-BNNTs [156]. In another study, the BNNTs were functionalized with organic hydrophilic agents including glucosamine (GA), poly(ethylene glycol) 1000 (PEG1000), and chitosan (CH), and their toxicity was investigated [157]. It was found that the PEG1000-BNNT and CH-BNNT were cytotoxic at high concentrations (100 μg/mL), while GA-BNNTs were not cytotoxic. Moreover, compatibility investigation of unmodified BNNTs showed that they were safe on the malignant U87 (wild type p53) and T98 (mutant p53) glioblastoma, MCF-7 adenocarcinoma mammary gland cells and normal MRC-5 fibroblast lung cells [158]. In another study, the cytotoxicity of Tween 80 coated BNNTs was investigated with several cell lines including lung adenocarcinoma cells (A549), murine alveolar macrophage cells (RAW 264.7), murine embryonic fibroblast cells (3T3-L1), and human embryonic kidney cells (HEK293) [159]. The results of that study demonstrated that BNNTs were cytotoxic at variable BNNT concentrations (0.2–20 g/mL) in a cell-type-dependent manner. They were enormously cytotoxic especially on macrophage cells due to the high endocytosis capacity of these cells. Furthermore, the biocompatibility of the glycol-chitosan modified BNNTs was investigated with *in vivo* studies. BNNTs were intravenously injected in rabbits at 1 mg/mL dose in a first experiment [160]; then, 5 and 10 mg/kg doses were adopted in a second experiment [161]. All the collected results indicated that the BNNTs have no significant adverse effect on white blood cells, red blood cells, and many other blood parameters of the rabbits upon their injection in the blood. In a recent study, gum Arabic functionalized BNNTs were injected into planarians to investigate the influence of the modified BNNTs on the regeneration of these worms. The animals amputated below their heads showed no important morphological and progressive differences when treated with BNNTs, with respect to the controls [162].

1.3.2. Hexagonal Boron Nitrides (hBNs)

Although hBNs were discovered in 1842, their first stable form was obtained about a century later. The hexagonal boron nitrides (hBNs), as structural analogs of graphene, have strong intralayer covalent bonding between B and N atoms and weak interlayer van der Waals bonding (Figure 1.9) [163]. hBNs can be potentially used in many fields including pharmacy, cosmetics, chemistry and high-temperature technologies, due to their biocompatibility, high chemical and thermal stability, excellent mechanical strength and electrical insulation properties [164, 165].

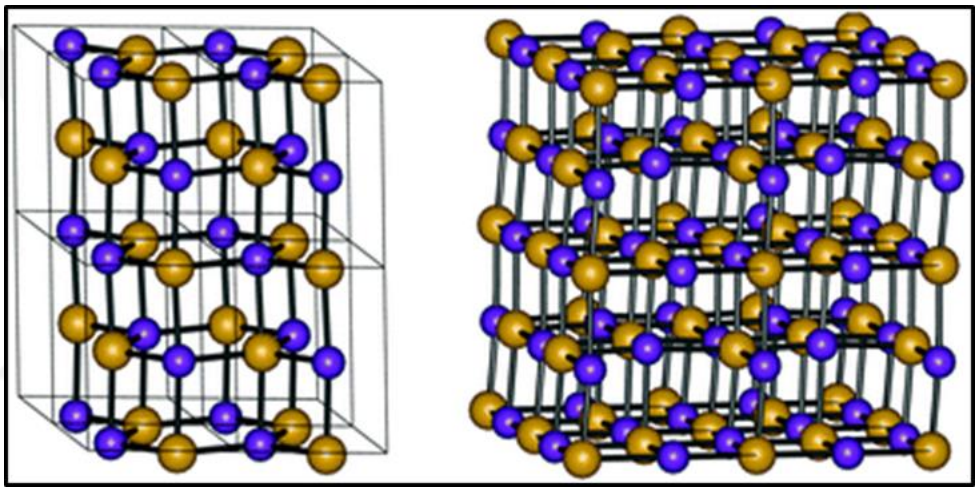

Figure 1.9. Schematic representation of hBNs [166].

1.3.2.1. hBN Synthesis

As one-dimensional boron nitride-based structures hBN are widely investigated in the literature, concerning both synthesis and characterization in several publications. In a study, BN nanocages were produced in a typical synthesis environment of boron nitride nanotubes using Arc discharge method in 1999 [167]. In that study, electrodes were covered with 99 per cent elemental boron and with 1 per cent nickel and cobalt as catalyst. Apart from the BN nanotubes, BN covered nanocrystals were formed in the synthesis environment. Following the removal of nanocrystals, hollow BN cocoons were obtained [167].

In another study, BN synthesis was performed two steps *via* CVD method. In the first step, B-N-O sphere particles were synthesized from ($B(OMe)_3$) and ammonia precursors. Then, oxygen atoms were removed from spheres by heating under ammonia atmosphere at high temperature [168]. However, Golberg and coworkers claimed that the $(OMe)3BNH_3$ complex were produced in place of removing oxygen atoms from structure at the second step. Therefore, there another intermediate phase was required to produce BN spheres. Then, the BN ceramics were formed using dehydrogenative hydrolysis from BH_3NH_3 for hydrogen elimination. At the end, B-O impurities generates the nuclear center of BN spheres that are in the size range of 50-400 nm [169].

In another study of Golberg and his team, they used argon (Ar) gas rather than NH_3 that evaporates B-O at the inner part of nanospheres at the second phase of the synthesis, in order to obtain hollow BN nanomaterials [90].

Next, hBN nanoparticles were synthesized under low temperature using ammonium borofluoride (NH_4BF_4), sodium azide (NaN_3) and sulfur (S) as precursors that had mixed each other with milling method. The mixture was heated up to 250^oC for 20 h. Finally, the product was washed with hydrochloric acid (HCl), benzene, and deionized water to remove iron, sulfur and water-soluble salt impurities, respectively. Then, BN nanoparticles were obtained around 35-45 nm sizes [170].

Lastly, spherical BN and BCNs were synthesized *via* elemental substitution reaction, where carbon nanocages were used as template and boron trioxide as boron source. They were mixed and heated under NH_3 gas flow for substitution reaction. Following the reaction, 1-3 μm sized microspheres were obtained with interconnected holes as shown in Figure 1.10, interpreted as the elemental substitution of B and N atoms in place of C atom [171].

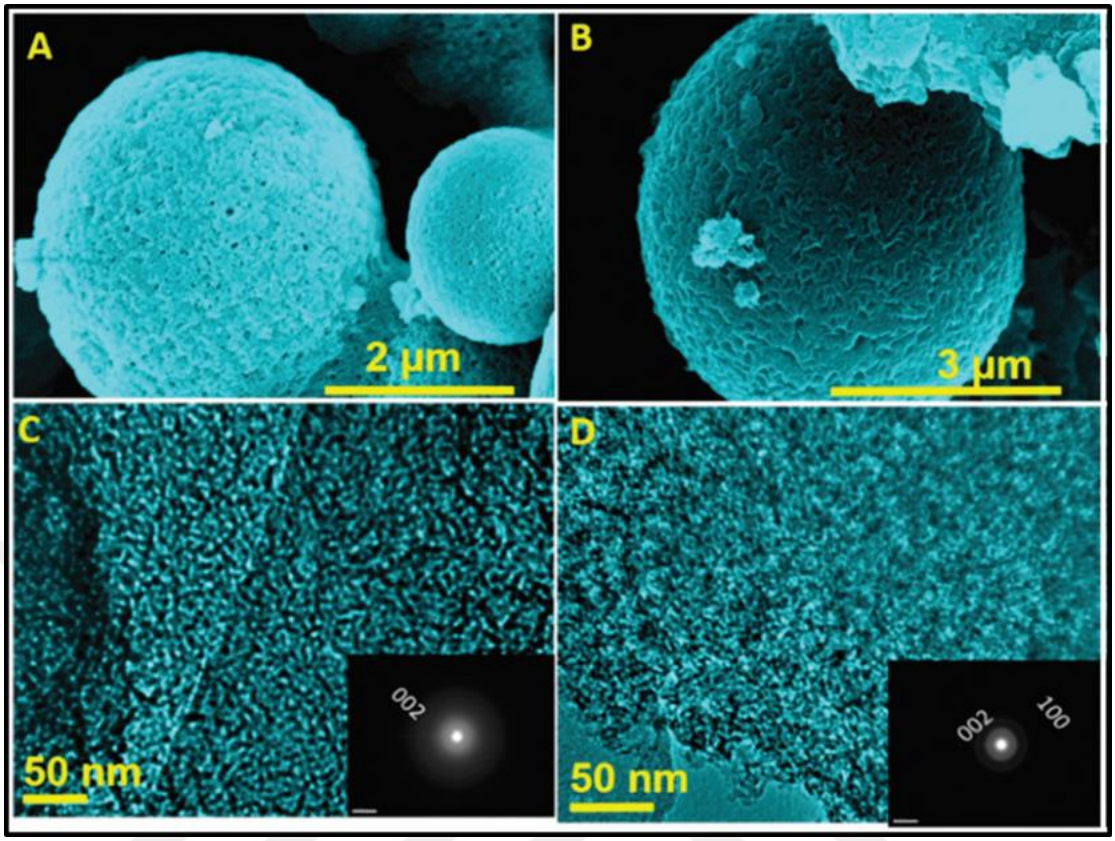

Figure 1.10. HRSEM and HRTEM images of MBN and MBCN nanocages (A and C: MBN; B and D: MBCN) [171].

The biocompatibility investigations of the BNNT and hBNs have been performed to clarify their acceptability in biomedical applications. Many of these investigations indicate that the BNNTs and hBNs are non-toxic, however their biocompatibility related to animal model, cell type, dose, their dispersion surfactant, BNNT aspect ratio and lateral size dimensions of hBNs. All together, we can conclude that BNNTs and hBNs have no significant adverse effects on the cell proliferation, metabolism and viability. However, the BNNTs and hBNs were found non-toxic in *in vitro* studies, more *in vivo* investigations should be performed in the future studies to reach more clear conclusions.

2. AIM OF THE STUDY

The investigation of the use of BNNTs and hBNs as drug carriers and as potential boron source in applications such as BNCT is the main objective of the thesis. The other objective was to investigate their cancer suppression property by emphasizing effect mechanisms.

First, the biocompatibility of BNNTs and hBNs was carefully investigated to avoid potential damage to healthy tissues. Then, their cellular uptake performance was investigated as one of the most important points to reveal their effectiveness.

Next, BNNTs and hBNs based drug delivery systems are optimized by considering the following points;

- Drug loading capacity and releasing conditions
- Cellular uptake performance of drug and targeting agent-loaded BNNTs and hBNs
- Intracellular accumulation of targeting agent-functionalized hBNs
- Therapeutic effect of hBNs on prostate cancer

3. MATERIALS AND METHODS

3.1. MATERIALS

3.1.1. Cell Lines

Human Dermal Fibroblast (HDF) cells, Adenocarcinomic Human Alveolar Basal Epithelial (A549) cells, human umbilical vein endothelial cells (HUVEC), cancerous HeLa cells, glioblastoma multiforme (U87MG) cells, androgen independent prostate (DU145 and PC3) cancer cells and healthy prostate (PNT1A) cells were purchased from American Tissue Culture Collection (ATCC).

3.1.2. Cell Culture Reagents

Dulbecco's Modified Eagle Medium (DMEM), Opti-MEM medium, fetal bovine serum (FBS), trypsin-EDTA, colchicine, bovine serum albumin (BSA), ribonuclease (RNase), Rhodamine 123 and propidium iodide (PI) were purchased from Sigma-Aldrich. Phosphate buffered saline (PBS) and penicillin streptomycin (Pen-Strep) were obtained from Gibco. WST-1 reagent was purchased from Roche. Calcein, AM, cell-permeant dye and dimethyl sulfoxide (DMSO) were purchases from Invitrogen. Cellular ROS detection assay kit and Annexin V-FITC Apoptosis Staining / Detection Kit were obtained from Abcam. Morpholino antisense oligonucleotides were prepared by Gene Tools. BD Matrigel matrix was purchased from BD Biosciences.

3.1.3. Chemicals

Colemanite ($Ca_2B_6O_{11}\cdot 5H_2O$) was a gift from Eti Mine Works General Management (Turkey). Iron (III) oxide (Fe_2O_3), hydrogen peroxide (H_2O_2), ethanol, boric acid, boron trioxide, nitric acid, calcium chloride dihydrate, sodium chloride, potassium hydrogen phthalate, glycine, sodium phosphate dibasic anhydrous and sodium sulfate (anhydrous) were purchased from Sigma-Aldrich. Glutaraldehyde and alkylbenzyldimethylammonium

chloride were obtained from Merck Millipore. Highly pure ammonia gas (99.98 per cent) was provided from Schick GmbH & Co. KG. Ethidium bromide was obtained from Bio-Rad and DNA Ladder was provided from Invitrogen.

3.2. METHODS

3.2.1. Synthesis, Functionalization and Biocompatibility of BNNTs

3.2.1.1. Synthesis of BNNTs

Boron nitride nanotubes were synthesized from colemanite using Fe_2O_3 as catalyst. Briefly, 2.0 g colemanite and 160 mg Fe_2O_3 were mixed into 2.0 mL ammonia solution (13.38 M) and this mixture was spread onto an alumina boat. After water evaporation from the mixture, it was placed into a tubular furnace (Protherm, Furnaces PTF 14/50/450). BNNTs were synthesized under NH_3 atmosphere for 3 h at 1280°C. For purification, the BNNTs were first stirred in 4 M HCl solution at 90°C for 4 h, and then the solution was centrifuged at 14000 rpm for 30 min. Then, 1 M HNO_3 solution was used for further purification. The BNNTs were stirred in 1 M HNO_3 solution at 30°C for 6 h. After centrifugation (14000 rpm, 30 min), they were washed with double distilled water (ddH_2O) to remove all the acid residues. Then, they were dried under vacuum for 24 h and stored at room temperature.

3.2.1.2. Characterization of BNNTs

The size and morphology of the synthesized BNNTs were monitored using scanning electron microscopy (SEM, Helios Nano-Lab 600i FIB/SEM, FEI). Before SEM imaging samples were prepared as gold-sputtered for 25 s at 60 nA to obtain a 3-nm thick conductive layer over the BNNTs. TEM images of the BNNTs were acquired with a JEOL-2100 HRTEM microscopy system at 200 kV (equipped with LaB6 filament and an Oxford Instruments 6498 EDS system).

Then, the BNNTs were dispersed in ddH_2O by sonication for 2 min before the analysis (Bandelin Sonopuls HD 3100). A Perkin Elmer Lambda 25 UV-Vis spectrometer was used

to obtain absorption spectra. The measurements were performed at least three times and their mean values were shown in the figures.

BNNTs were analyzed in dried form using IR spectroscopy; the spectra were acquired with a Thermo NICOLET IS50 Spectrometer. The measurements were performed at least three times and mean values of the spectra were shown in the figures. Moreover, the BNNTs were dispersed in ddH_2O and samples prepared as drops on CaF_2 slides. Raman spectra of the BNNTs were recorded using a Renishaw In Via Reflex Raman Microscopy system (Renishaw Plc., New Mills, Wotton-under-Edge, UK) equipped with a 514 nm Argon ion laser. A minimum of 16 spectra was acquired from a 16-μm^2 BNNT sample area. The mean values of the spectra were shown in the figures.

3.2.1.3. Functionalization of the BNNTs

3.2.1.3.1. Hydroxylation of BNNTs

In the hydroxylation process, 100 mg of pure BNNTs were added into 10 mL of 30 per cent H_2O_2 solution and the mixture was sonicated for 1 h at 25°C. Then, the mixture was refluxed for 48 h at 110°C while stirring. The obtained hydroxylated BNNTs (h-BNNTs) were precipitated by centrifugation (15 min, 10000 rpm) and washed with ddH_2O five times and dried at 60°C. The h-BNNTs were stored at room temperature.

3.2.1.3.2. Carbohydrate (Glucose, Lactose and Starch) Modification of h-BNNTs

As carbohydrates, glucose, lactose and starch were used for further modification (m-BNNTs) of h-BNNTs. Briefly, a suspension was prepared by dispersing 100 mg of h-BNNTs in 10 mL of deoxygenated H_2O and sonicated for 30 min. 10 mL of 5 per cent w/v glucose, 5 per cent w/v lactose or 2 per cent w/v starch solution were added to the suspensions. These suspensions were then incubated for 48 h on a magnetic stirrer at 37°C after adding 500 µL of 10 per cent v/v glutaraldehyde. The obtained m-BNNTs were precipitated by centrifugation (30 min, 14000 rpm) and washed with ddH_2O five times and dried in a vacuum oven at 30°C. The m-BNNTs were thereafter stored at room temperature.

3.2.1.3.3. Characterization of Functionalized BNNTs

The synthesized h-BNNTs and m-BNNTs were analyzed in dried form using IR spectroscopy; the spectra were acquired with a Thermo NICOLET IS50 Spectrometer. The measurements were performed at least three times and their mean values were shown in the figures.

Thermogravimetric analysis (TGA) was performed on synthesized BNNTs, h-BNNTs and m-BNNTs by using a Perkin Elmer Pyris 1 TGA. The weight of samples was measured between the temperatures 30-700°C and the results shown in relevant figures.

3.2.1.4. Biocompatibility of BNNTs

3.2.1.4.1. Biocompatibility of BNNTs on Mammalian Cells

Cell Culture

The biocompatibility of BNNTs, h-BNNTs and m-BNNTs was tested on human dermal fibroblast (HDF) and on adenocarcinomic human alveolar basal epithelial (A549) cell lines. The cells were used to assess the cytotoxicity and the genotoxicity of modified and unmodified BNNTs. HDFs were cultured in Dulbecco's Modified Eagle's Medium (DMEM), supplemented with 10 per cent fetal bovine serum (FBS) and 1 per cent penicillin streptomycin ampicillin (PSA) as antibiotics. A549 cells were cultured in (DMEM F-12) supplemented with 1 per cent L-glutamine in addition to 10 per cent FBS and 1 per cent PSA. The cells were incubated in water-jacketed incubator in a 5 per cent CO_2, 95 per cent air atmosphere at 37°C.

Cell Viability Assay

The cytotoxic effects of the modified and unmodified BNNTs on cells were quantified with 2-(2-methoxy-4-nitrophenyl)-3-(4-nitrophenyl)-5-(2,4-disulfophenyl)-2H-tetrazolium (WST-1) colorimetric assay. First, HDFs were seeded at 5×10^3cells/well and A549 cells

were seeded at 1×10^4 cells/well in 96-well plates. The cells were incubated for 24 h, then treated with BNNTs, h-BNNTs and m-BNNTs at increasing concentrations (5 μg/mL,10 μg/mL, 20 μg/mL, 50 μg/mL, 100 μg/mL and 200 μg/mL). The concentration of the modified BNNTs was adjusted basing on the TGA data (Figure 4.6). After 1-3 days of incubation, the culture medium in 96-well plates was replaced with fresh culture medium containing WST-1 reagent with 1:10 ratio and incubated for a further 1 h. The percentage of living cells is calculated by measuring absorbance of formed formazan salts at 450 nm with an microplate reader.

Reactive Oxygen Species (ROS) Detection Assay

The ROS detection test was applied to BNNTs, h-BNNTs, and m-BNNTs exposed A549 cells. The cells were seeded in 24-well plates (the number of the cells was 1×10^5 for each well) and incubated for 24 h at 37°C. In the following day, the cells were treated with ROS detection reagent (2,7 dichlorofluorescindiacetate, DCFDA) and incubated for 30 min at 37°C. After diffusion into the cells, the DCFDA is transformed to a non-fluorescent compound by deacetilation. Then, the ROS detection reagent containing medium was removed and the cells were incubated for 24 h at 37°C with the increasing concentrations (5 μg/mL, 10 μg/mL, 20 μg/mL, 50 μg/mL, 100 μg/mL and 200 μμg/mL) of BNNTs, h-BNNTs and m-BNNTs. The non-fluorescent compound in the cells is oxidized into the fluorescent 2,7-dichlorofluorescein (DCF) by the presence of ROS in the cells. Finally, the cells were analyzed with a flow cytometer.

Genotoxicity Assay

The genotoxicity of BNNTs, h-BNNTs, and m-BNNTs on A549 cells was analyzed with the comet assay. The cells were treated with all the samples at 100 μg/mL and incubated for 24 h. Following the exposure to modified and unmodified BNNTs, the cells were collected into 1 mL PBS and embedded in 1 per cent low melting agarose onto high melting agarose coated slides, which were kept into refrigerator at 4°C for 30 min. Then, the slides were put into lysis solution (1 per cent Triton X, 10 mL DMSO, 2.5 M NaCl, 0.1 EDTA, 10 mM Tris base, pH 10) for 1 h at 4°C. The cells were denaturated with alkaline buffer for 40 min; then,

electrophoresis was performed at 25 V and 300 mA for 20 min with alkaline buffer. The slides were immersed in neutralization buffer (0.5 M Tris–HCl, pH 7.5) for 15 min at 4°C. Finally, the samples were fixed with 70 per cent ethanol for 10 min. The DNA was stained with SYBR green dye at the 4°C for 30 min. After all these procedures, the comet images were taken by florescence microscopy and the tail length of the DNA was measured by comet image analysis software (Comet IV). Fifty comets were analyzed for BNNTs, h-BNNTs and m-BNNTs sample.

3.2.1.4.2. Biocompatibility of BNNTs on Microorganisms

Yeast Culture

Yeast (*Saccharomyces cerevisiae*) cells were utilized for biocompatibility tests. They were cultured in Yeast Extract–Peptone–Dextrose (YPD) medium. To remove the yeasts from media, they were washed three times with PBS followed by centrifugation (5 min, 1500 rpm). The yeast concentration in the PBS was determined using UV/Vis spectroscopy at 600 nm.

LbL-coating of Yeasts with PEs (PLL-PSS-PLL) and BNNT-OHs

The yeasts were coated with poly-L-lysine (PLL) and polystyrene sulfonate (PSS) as positive and negative charged polyelectrolytes, respectively. The negatively charged *S. cerevisiae* cell wall was first coated with PLL. The yeasts were suspended in 1 mL of PLL solution (1 mg/mL in 0.5 M NaCl). They were incubated while shaking for 15 min and then washed three times with NaCl (0.5 M) to remove free PLL molecules.

PLL-coated yeasts were exposed to PSS to provide the second monolayer around the cell wall. This step was performed by resuspending the yeasts in 1 mL of PSS solution (1 mg/mL in 0.5 M NaCl) and incubating the mixture while shaking for 15 min. After coating with PLL/PSS, the yeasts were washed three times with NaCl (0.5 M) solution to remove free PSS molecules.

The PSS-PLL-coated yeasts were exposed to PLL again to obtain third monolayer around

the yeasts. After washing step, PLL/PSS/PLL coated yeasts were obtained. The yeasts were suspended in 1 mL of PLL solution (1 mg/mL in 0.5 M NaCl). The cells were incubated while shaking for 15 min and then washed three times with NaCl (0.5 M) to remove free PLL molecules.

Finally, the PLL/PSS/PLL-coated yeasts were treated with h-BNNTs in NaCl solution (1 mg/mL in 0.5 M NaCl), thus promoting the h-BNNT absorption by electrostatic interaction due to the negatively charged hydroxyl groups linked to the BNNTs. The cells were incubated with h-BNNTs while shaking for 30 min.

Characterization of PEs and h-BNNTs Coated Yeasts

The surface potential of the yeast cells was measured using a Malvern Nano ZS instrument in 0.5 M NaCl solution after the absorption of each layer of the oppositely charged PEs. The PEs and h-BNNTs coated yeasts were analyzed with FTIR (Thermo NICOLET IS50) following each coating step of PEs and h-BNNTs. PEs- and h-BNNTs-coated cells were visualized with SEM before and after PE and h-BNNT coating processes. SEM (Helios Nano-Lab 600i FIB/SEM, FEI) imaging was carried out on samples previously gold-sputtered for 25 s at 60 nA, obtaining a 3-nm thick conductive layer over the samples.

Biocompatibility Assay

The cytotoxicity of the PEs and h-BNNTs coating around the yeasts was assessed with the 2-(2-methoxy-4-nitrophenyl)-3-(4-nitrophenyl)-5-(2,4-disulfophenyl)-2H-tetrazolium (WST-1) colorimetric assay. Yeasts were prepared as bare, PLL, PLL/PSS, PLL/PSS/PLL and PLL/PSS/PLL/h-BNNT coated samples. The yeast viability was analyzed following one day of incubation. Yeast medium mixed to the WST-1 reagent (10:1) was provided to the samples, and the formazan products absorbance was measured at 450 nm with a microplate reader.

3.2.2. Synthesis, Functionalization and Biocompatibility of hBNs

3.2.2.1. Synthesis of hBNs

In the synthesis of hexagonal boron nitride (hBNs), boric acid and ammonia as boron and nitrogen sources, respectively, were used. First, boric acid solution was prepared by suspending 2 g of boric acid in 3 mL of 13.38 M ammonia solution. Then, the mixture was layered on a silicon carbide boat and dried on a hot plate adjusted to 100°C for approximately 20 min. Then, the mixture on silicon carbide boat was heated in a Protherm Furnace PTF 14/50/450 until 1300°C with a heating rate of 10°C/min under ammonia gas flow for 2 h. After the heating process, the silicon carbide boat was removed from furnace at around 550°C and hBNs were collected in a tube from the surface of the silicon carbide boat and stored under room conditions.

3.2.2.2. Characterization of hBNs

3.2.2.2.1. Imaging Techniques

Size and morphology of the synthesized hBNs were characterized using SEM (Helios Nano-Lab 600i FIB/SEM, FEI). Before the SEM imaging samples were coated with gold-sputtered for 25 s at 60 nA previously to obtain a 3-nm thick conductive layer over the hBNs. Next, TEM images of hBNs were performed using a JEOL-2100 HRTEM microscopy system at 200 kV (equipped with LaB_6 filament and an Oxford Instruments 6498 EDS system).

3.2.2.2.2. Spectroscopic Techniques

As a spectroscopic technique UV/Vis spectroscopy (Perkin Elmer Lambda) were utilized to analyze absorption of hBNs, following the hBNs were dispersed in ddH_2O by sonication for 2 min before the analysis. The measurements were repeated at least three times and their mean values are shown in the figures. The hBNs were also analyzed with IR spectroscopy (Thermo NICOLET IS50 Spectrometer) in their dried form. Lastly, Raman spectra of the hBNs were recorded using a Renishaw In Via Reflex Raman Microscopy system (Renishaw

Plc., New Mills, Wotton-under-Edge, UK) equipped with a 514 nm Argon ion laser. From a 16-μm^2 of each hBNs sample area a minimum of 16 spectra was acquired. Each sample was measured at least three times and their mean values are shown in the figures.

3.2.2.3. Biocompatibility of hBNs

Biocompatibility of hBNs, was quantified with WST-1 colorimetric assay. First, 7×10^3 HDF cells/well were seeded in 96-well plates and incubated for 24 h. Then, the medium of cells was replaced with the hBNs at several concentrations (25, 50, 100, 150, 200, 300 and 400 μg/mL). Following 24 h of incubation, the culture media was replaced with fresh culture media containing WST-1 reagent at 1:10 ratio and further incubated for 1 h. The percentage of living cells is calculated by measuring absorbance of formed formazan salts at 450 nm with a microplate reader.

3.2.3. BNNTs and hBNs as Nanocarriers for Anticancer Drugs

3.2.3.1. Noncovalent Interaction of Doxorubicin (Dox) with BNNTs and hBNs

3.2.3.1.1. Concentration Dependent Evaluation

BNNTs and hBNs were complexed with Dox at a fixed pH in PBS (pH 7). 2.0 mL of Dox solutions at 0.5, 1.0, 2.0, 4.0 and 5.0 mM in PBS were prepared, and 3.0 mg of BNNTs or hBNs were added into these solutions. These suspensions were stirred at room temperature for 24 h. Then, the free Dox was removed by centrifugation of the samples at 10,000 r.p.m. for 15 min by removing the supernatant. The pellet settled at the bottom of the tube was re-dispersed and washed with PBS three times. The characterization of the Dox loading onto the BNNTs and hBNs was performed with a Perkin Elmer Lambda 25 UV/Vis Spectrometer and a Cary Eclipse Fluorometer. The fluorescence spectroscopy measurement was performed at maximum excision and emmision wavelengths of Dox (480 and 555 nm). The absorption wavelength was 480 nm for all measurement involving Dox.

3.2.3.1.2. pH Dependent Evaluation

The Dox interaction with BNNTs or hBNs was tested at several pH values to find out the optimal loading. Thus, 5.0 mM of Dox and 3.0 mg of BNNTs or hBNs were stirred at room temperature for 24 h in PBS, where pH was fixed at pH 4, pH 7 and pH 11. Following their incubation, their washing was performed with centrifugation at 10000 rpm for 15 min at the same pH values in PBS that were also used for their loading process. The characterization of the Dox–BNNTs and of the Dox–hBNs interaction was performed with UV/Vis and fluorescence spectroscopy.

3.2.3.2. Dox Release from BNNTs and hBNs

The Dox released from the BNNTs or hBNs was monitored at fixed concentration ratios of the samples at different pH values to reveal the pH effect. The Dox–BNNTs and Dox–hBNs were prepared at different pH values (pH 4, 7 and 11) and shaked at room temperature for several h (1, 2, 4, 8, 24 and 72 h). Following their incubation, they were centrifuged at 10000 rpm for 15 min and their supernatants were collected to measure the released Dox in PBS with UV/Vis spectroscopy.

3.2.3.3. Folate Loading on Dox-BNNT Structures

Folate was loaded onto the Dox–BNNTs to target cancer cells, which overexpress folate receptors on their surfaces. A 2.0 mM solution of folate was stirred with 1.043 mg of Dox–BNNTs (10 wt per cent of 5.0 mM Dox interacted with BNNTs), 1.0 mg of BNNTs alone in 3.0 ml of PBS at room temperature for 24 h. After three washing steps, their interaction was characterized with Malvern Zeta sizer and UV/Vis spectrometer.

3.2.3.4. Cellular Uptake of F-Dox-BNNTs

HeLa cells and HUVECs were seeded on coverslips and incubated for 24 h. Due to 10 per cent loading efficiency of Dox onto the BNNTs, 0.5 mM of free Dox, which is the 1/10 of the initial Dox concentration used to treat BNNTs, was applied to the control cells. A 20-

μg/ml concentration of Dox–BNNTs (5.0 mM) or F–Dox–BNNTs (5.0 mM) was administered to the cells and incubated for 4 h. In a control experiment, 1.0 ml of 3.5 mM folate solution was added into the media to compete with F–Dox–BNNTs by saturating the folate receptors on HeLa cells. After the addition of folate solution into the cell culture media, a 30 min incubation was performed for allowing competitive inhibition. After the 30 min incubation, folate was discarded and the F–Dox–BNNTs were added into the cell culture and incubated for 4 h. After this incubation period, the media were removed from the cultures and the cells were washed with PBS three-times. A 4 per cent (v/v) paraformaldehyde solution was used for fixation of the cells. The paraformaldehyde solution was added into the cells and incubated for 30 min at 4°C. Then, the cells were washed with PBS for 5 min for three-times. The samples were examined with a Zeiss LSM 700 confocal laser-scanning microscope. Then the images were analyzed with ImageJ program for fluorescence intensity quantification of Dox-including structures up-taken by the cells.

3.2.3.5. Cell Viability Studies of F-Dox-BNNTs

The effect of F–Dox–BNNTs, Dox–BNNTs, BNNTs and free Dox on cell viability was comparatively quantified with 2-(2-methoxy-4-nitrophenyl)-3-(4-nitrophenyl)-5-(2,4-disulfophenyl)-2H-tetrazolium (WST-1) colorimetric assay on cancerous HeLa cells and healthy human umbilical vein endothelial cells (HUVECs). First, the cells were seeded at a density of 8×10^3 cells/well in 96-well plate, and incubated for 24 h. The cells were then treated with BNNTs, free Dox, Dox–BNNTs and F–Dox–BNNTs at increasing concentrations (5, 10, 20, 50 and 100 μg/mL). After fixed incubation times (1, 2, 4, 8, 24 and 72 h), the media was replaced with fresh culture media containing WST-1 reagent with 1:10 ratio and incubated for one more h. The percentage of living cells was calculated by measuring absorbance of formed formazan salts at 450 nm with a microplate reader.

3.2.4. Transferrin-mediated Glioblastoma Cancer Targeting of hBNs

3.2.4.1. hBN Functionalization with DSPE-PEG-NH_2 and Characterization

hBNs and DSPE-PEG-NH_2 interaction was optimized using several concentration ratios of

the components, and by changing sonication durations. In the optimized protocol, hBNs were ultrasonicated for 2 min for an efficient dispersion. Then, hBNs and DSPE-PEG-NH_2 were ultrasonicated for 1 min to allow their interaction. Following this process, intensive washing procedure was applied to remove weakly bound DSPE-PEG-NH_2 molecules from the hBNs. The characterization of the DSPE-PEG-hBNs was performed with UV/Vis spectroscopy (Perkin Elmer Lambda 25 UV-Vis spectrometer); the measurements were performed three times. Furthermore, the DSPE-PEG-hBNs interaction yield was analyzed using TGA (Mettler Toledo TGA/SDTA 851 instrument) following a drying process in vacuum oven at 60°C for 24 h to remove water molecules in the samples. The samples were analyzed with TGA under 20 mL/min N_2 gas flow. The temperature was increased up to 700°C at a rate of 10°C/min.

3.2.4.2. Colloidal Stability of DSPE-PEG-hBNs

The colloidal stability analysis of hBNs and DSPE-PEG-hBNs was performed comparatively by monitoring the size distribution of the samples in ddH_2O. According to the DSPE-PEG-hBN interaction ratio, the concentration of hBNs and DSPE-PEG-hBNs were fixed as 1000 μg/mL and 1120 μg/mL, respectively. Following the interaction process, samples were assessed with dynamic light scattering (DLS) at several times (0, 1 and 24 h) to evaluate their time-dependent colloidal stability.

3.2.4.3. DSPE-PEG-hBN Functionalization with Transferrin and Characterization

NHS groups are generally used as activating agent of carboxylic acid [173]. In this study, they were used as active end for the modification of the DSPE-PEG-hBNs with the carboxylic acid groups of the amino acids belonging to the transferrin protein. 1120 μg DSPE-PEG-hBN and 1 mg transferrin were incubated by shaking overnight in borate buffer (pH 9) at 4°C. Then, the samples were washed three times with centrifugation, and free transferrin molecules were removed from the reaction environment. The characterization of TfR-DSPE-PEG-hBN was performed with FT-IR (Thermo NICOLET IS50 Spectrometer) and interaction yield was investigated with BCA assay. In the BCA measurements, several concentrations of transferrin (between 0-250 mg/mL) were prepared as standard solutions to

reveal the interacted transferrin concentration. 25 µL of hBN, DSPE-PEG-hBN, TfR-DSPE-PEG-hBN samples and standard solutions were added to 2 mL of BCA working reagents in 96 well-plates and incubated for 30 min at 37°C. Since the method relies on reduction of Cu^{2+} to Cu^{+} by protein in an alkaline medium, the reduction of the Cu^{2+} was measured using a unique reagent containing bicinchoninic acid that can be detected with sensitive and selective absorption of light at 562 nm.

3.2.4.4. Biocompatibility and Cellular Uptake of TfR-DSPE-PEG-hBNs

3.2.4.4.1. Cell Culture

U87MG glioblastoma multiforme cell line was utilized to assess the cytotoxicity and the cellular uptake of hBNs, DSPE-PEG-hBNs and TfR-DSPE-PEG-hBNs. The cells were cultured in Dulbecco's Modified Eagle's Medium (DMEM), supplemented with 10 per cent fetal bovine serum (FBS), 1 per cent penicillin/streptomycin/ampicillin (PSA) antibiotics and supplemented with 1 per cent L-glutamine. The cells were incubated in water-jacketed incubator in a 5 per cent CO_2, 95 per cent air atmosphere at 37°C.

3.2.4.4.2. Biocompatibility of TfR-DSPE-PEG-hBNs

Biocompatibility of hBNs, DSPE-PEG-hBNs and TfR-DSPE-PEG-hBNs was quantified with 2-(2-methoxy-4-nitrophenyl)-3-(4-nitrophenyl)-5-(2,4-disulfophenyl)-2H-tetrazolium (WST-1) colorimetric assay. First, 6×10^3 U87MG cells/well were seeded in 96-well plates and incubated for 24 h. Then, the medium of cells was replaced with the hBNs at several concentrations (5, 10, 50 and 100 µg/mL) and with equal concentrations of DSPE-PEG-hBNs and TfR-DSPE-PEG-hBNs. Following 24 h of incubation, the culture medium was replaced with fresh culture medium containing WST-1 reagent at 1:10 ratio and further incubated for 1 h. The percentage of living cells is calculated by measuring absorbance of formed formazan salts at 450 nm with a microplate reader.

3.2.4.4.3. Cellular Uptake of TfR-DSPE-PEG-hBNs

The cellular uptake of hBNs, DSPE-PEG-hBNs and TfR-DSPE-PEG-hBNs by U87MG cells was investigated using flow cytometer. 6×10^4 U87MG cells were seeded in 24-well plates and incubated for 24 h. Then the medium of cells was replaced with the medium that includes a single concentration (50 μg/mL) of hBNs, DSPE-PEG-hBNs, or TfR-DSPE-PEG-hBNs. They were incubated at several incubation times (1, 4, 8, 24 and 48 h). Thereafter, cells were removed from plate following a trypsin treatment and dispersed in phosphate buffer saline (PBS) solution for flow cytometry measurements. The increased side scattering of the cells due to the uptake of hBNs, DSPE-PEG-hBNs or TfR-DSPE-PEG-hBNs were analyzed by flow cytometer.

3.2.4.4.4. Confocal Microscopy Images of TfR-DSPE-PEG-hBNs Treated Cells.

The cellular uptake of TfR-DSPE-PEG-hBNs was observed by using FITC-labeled DSPE-PEG-NH_2 by confocal microscopy. In this study, DSPE-PEG-NH_2 molecules were covalently modified with FITC by shaking overnight in borate buffer (pH 9) at 4°C. The free FITC molecules were removed from the interaction solution by washing three times using filter-based centrifugation process. Then, 1 mg of hBNs was incubated with 249 μg of DSPE-PEG-FITC and DSPE-PEG-NH_2 at a ratio of 1:4. Finally, DSPE-PEG-FITC-hBNs were modified with transferrin by shaking overnight in borate buffer (pH 9) at 4°C. Then, the samples were washed three times with centrifugation and free transferrin molecules were removed from reaction environment.

2×10^5 U87MG cells/well were seeded on cover slips at 6-well plate and incubated overnight. Then, the media of the cells were replaced with 10 μg/mL TfR-FITC-DSPE-PEG-hBN, and 100 μg/mL TfR-FITC-DSPE-PEG-hBN including fresh media, and incubated for 24 h. Following the incubation, cells were fixed with 4 per cent paraformaldehyde at 4°C for 30 min and washed with PBS for 5 min three times. The samples were examined with a Zeiss LSM 700 confocal laser-scanning microscope.

3.2.5. hBNs, as Boron Source, in Prostate Cancer Treatment

3.2.5.1. Cell Culture

The inhibitory effects of hBNs and boric acid (BA) on prostate cancer cells were tested on androgen independent (DU145, PC3) cancer cells, comparatively. As a control, healthy prostate (PNT1A) cells were used. The cells were cultured in Dulbecco's Modified Eagle's Medium (DMEM), supplemented with 10 per cent Fetal Bovine Serum (FBS) and 1 per cent penicillin streptomycin ampicillin (PSA) antibiotics. The cells were incubated in water-jacketed incubator in a 5 per cent CO_2, 95 per cent air atmosphere at 37°C.

3.2.5.2. Determination of the Concentration and Cellular Sensitivity for hBNs

The sensitivity of the prostate cancerous cells toward hBNs was analyzed by varying applied hBN concentrations and incubation times. In this study, viability of hBNs treated cells was quantified with 2-(2-methoxy-4-nitrophenyl)-3-(4-nitrophenyl)-5-(2,4-disulfophenyl)-2H-tetrazolium (WST-1) colorimetric assay. Cells were seeded at a density of 7×10^3 cells/well in 96-well plates and incubated for different time points (1 and 3 days). Following the incubation process, the cells were treated with increasing concentrations of hBNs and BA were quantified as 2.2, 4.4, 11, 22, 44, 88, 176, 220 and 440 µg/mL boron including amounts. Then, the medium of cells was replaced with fresh culture medium containing WST-1 reagent at 1:10 ratio, and cells were incubated for a further 1 h. The percentage of living cells is calculated by measuring absorbance of formed formazan salts at 450 nm with an microplate reader.

3.2.5.3. Cellular Uptake of hBNs

The cellular uptake and intracellular degradation of hBNs were tested on DU145 and PNT1A cells by measuring intensity of the scattering of cells using flow cytometer and by analyzing the boron content with ICP-MS. The cells were seeded in 24-well plates (the density of the cells was 2.5×10^4 for each well) and incubated for 24 h at 37°C. Following day, the cells were treated with increasing amount of (22, 44, 88 and 176 µg/mL) boron including hBNs

and incubated for 1 and 3 days. Following the incubation, the cells were detached with trypsin and collected in PBS. The intensity of cell side scattering signal was analyzed by flow cytometers.

The intracellular degradation of hBNs in DU145 cells was measured with ICP-MS. Cells were seeded in 24-well plates (the density of the cells was 2.5×10^4 for each well) and incubated for 24 h at 37°C. In the following day, the cells were treated with increasing amount of (22, 44, 88 and 176 µg/mL) boron including hBNs and incubated for 1 and 3 days. After the incubation, the cells were detached from plates using trypsin and exposed to lysis solution to remove cellular components as pellet. Then cells were centrifuged at 10000 rpm for 10 min at 4°C. Then, 0.5 mL of the degradation products including supernatant was mixed with 4.5 mL of 1 per cent nitric acid solution. The measurements were performed using an ICP-MS (X Series 2, Thermo Scientific) instrument equipped with a CETAC asx-520 autosampler.

3.2.5.4. Analysis of hBN Treated Cells

3.2.5.4.1. Cell Cycle Analysis of hBN Treated Cells

Cell cycle of the hBN and BA exposed DU145 and PNT1A cells was analyzed using flow cytometer. The cells were seeded in 24-well plates (the density of the cells was 2.5×10^4 for each well) and incubated for 24 h at 37°C. Then, the cells were incubated with increasing concentrations (22, 44, 88 and 176 µg/mL) of boron including hBN and BA for 1 and 3 days at 37°C. Then, hBN and BA including media were replaced with 0.5 µg/mL of propidium iodide (PI) and 2.5 µg/mL of RNase including buffer and incubated for 30 min at room temperature. Cells were finally analyzed with flow cytometer.

3.2.5.4.2. Mitochondrial Function Analysis of hBN Treated Cells

Mitochondrial function of the hBN and BA exposed DU145 and PNT1A cells was analyzed using flow cytometer. The cells were seeded in 24-well plates (the density of the cells was 2.5×10^4 for each well) and incubated for 24 h at 37°C. Then, the cells were incubated with increasing concentrations (22, 44, 88 and 176 µg/mL) of boron including hBN and BA for

1 and 3 days at 37°C. Then, hBN and BA including media were replaced with 1 μg/mL of Rhodamine123 (Rho123) including PBS and incubated for 45 min at room temperature. Cells were finally analyzed with flow cytometer.

3.2.5.4.3. Reactive Oxygen Species (ROS) Detection of hBN Treated Cells

ROS production in hBN and BA-exposed DU145 and PNT1A cells was measured using flow cytometer. The cells were seeded in 24-well plates (the density of the cells was 2.5×10^4 for each well) and incubated for 24 h at 37°C. In the following day, the cells were treated with ROS detection reagent (2,7 dichlorofluorescindiacetate, DCFDA) and incubated for 30 min at 37°C. After the DCFDA reagent diffused into the cells, the DCFDA is transformed to a nonfluorescent compound by deacetilation. Then, the ROS detection reagent containing media was replaced with the 22, 44, 88 and 176 μg/mL boron containing amount of hBN and BA including media. Then, the cells were incubated for 1 and 3 days. The non-fluorescent compound in the cells was oxidized into the fluorescent 2,7-dichlorofluorescein (DCF) by the presence of ROS in the cells that were analyzed with flow cytometer.

3.2.5.4.4. Death Mechanism of hBN Treated Cells

The death mechanisms of hBN- and BA-exposed DU145 and PNT1A cells were studied using flow cytometer. The cells were seeded in 24-well plates (the density of the cells was 2.5×10^4 for each well) and incubated for 24 h at 37°C. Next day, the cells were incubated with increasing concentrations (22, 44, 88 and 176 μg/mL) of boron including hBN and BA for 1 and 3 days at 37°C. Then, the hBN and BA-including media were replaced with anexin V-FITC and PI including binding buffer (Alexa Fluor® 488 Annexin V/Dead Cell Apoptosis Kit, ThermoFisher) and incubated for 30 min. Then, the cells were analyzed with flow cytometer.

3.2.5.4.5. DNA Fragmentation Analysis of hBN Treated Cells

The DNA fragmentation of hBN and BA-exposed DU145 cells was analyzed by gel electrophoresis of the whole cell DNA. In this study, the cells were seeded in 24-well plates

(the density of the cells was 2.5×10^4 for each well) and incubated for 24 h at 37°C. Next day, the cells were incubated with increasing concentrations (22, 44, 88 and 176 µg/mL) of boron-including hBN and BA for 1 and 3 days at 37°C. Then, the cells were lysed overnight at 37ºC. Next day, the whole DNA of cells was isolated by incubating samples in equal volume of phenol and chloroform and centrifuging at 14000 rpm for 15 min. Then, the supernatant was mixed with equal volume of ammonium acetate (7.5 M) and ethanol (100 per cent). The mixture was centrifuged at 14000 rpm for 15 min. The pellet was diluted in TBE buffer and loaded on the agarose gel (2 per cent). Then, the gel run at 80-150 V until the dye line is approximately 75-80 per cent of the way down the gel.

3.2.5.4.6. Imaging the Cytoskeleton of Cells

The cytoskeleton of cells is mainly constituted by actin fibers, and it plays an important role in the migration of cancer cells in metastasis process. Thus, the effect of the hBN on actin fibers was monitored by exploiting confocal microscopy. In this study, DU145 and PNT1A cells were seeded in 24-well plates (the density of the cells was 2.5×10^4 for each well) and incubated for 24 h at 37°C. Then, the cells were treated with 88 µg/mL boron including hBN and BA. Following 1 and 3 day of incubation, the cells were fixed using 4 per cent of paraformaldehyde and then washed with PBS three times. The actin fibers of the cells were stained with Alexa Fluor 488® phalloidin (Excitation/Emission: 495/518 nm) and washed with PBS for three times. The confocal microscopy images of the cells were acquired by using 63X objective.

4. RESULTS AND DISCUSSION

4.1. SYNTHESIS, FUNCTIONALIZATION AND BIOCOMPATIBILITY OF BNNTs

4.1.1. Characterization of BNNTs

The precise characteristics of nanomaterials, including size, shape, surface charge, chemical structures and dispersibility require high quality characterization techniques such as imaging and spectroscopic [174]. As new generation imaging techniques including scanning and transmission electron microscopy (SEM and TEM), and they present high resolution. These imaging techniques are widely used not only in materials characterization, but also in biological sciences. Basically, SEM scans the surface of the structures with high energy beams of electron. With these imaging techniques, high-resolution (less than 1 nm) and three-dimensional images of a sample can be obtained [175]. However, the main disadvantage of SEM imaging is that it requires conductive specimens may require coating with a thin layer of conductive materials such as gold [176]. This is required to prevent accumulation of static electricity on samples. The working approach of the TEM does not rely on absorption, but instead on diffraction of the electrons. Therefore, inner part of the samples can be seen in this imaging technique since an electron beam is transmitted through the samples [177]. A drawback of TEM is that it requires very thin layers (1 μm) of sample slices [178]. As a complementary imaging technique, atomic force microscope (AFM) has a probe including a sharp tip located near a cantilever beam and scans above the sample using a piezoelectric scanner. It is another imaging instrument that obtains very high-resolution images of samples topology [179]. In this study, BNNT morphology was analyzed using SEM and AFM imaging techniques (Figure 4.1a and b). They were synthesized high yieldingly and in well purified form. The results indicated that the average diameter of the BNNTs is around 70 nm and they have uniform structures.

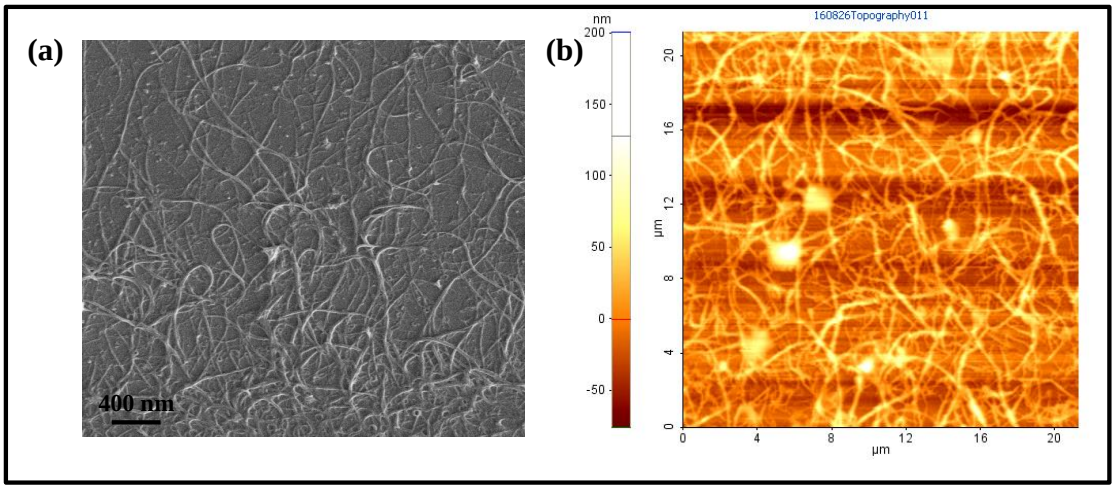

Figure 4.1. SEM (a) and AFM (b) imaging of BNNTs.

Concerning spectroscopic characterization, ultraviolet (UV/Vis), infrared (IR) and Raman spectroscopy play very important roles. UV/Vis spectroscopy is based on absorption of light [180]. Therefore, the samples have absorption at ultraviolet and visible region of light could be analyzed qualitative and quantitatively. IR spectroscopy has the same principle but uses IR region of light in place of ultraviolet/visible [181]. Raman spectroscopy is a technique based on vibrations and rotations of the bonds in chemical structures of samples, and more specifically on the inelastic scattering of monocromatic laser beams that excites molecules from ground state originating Raman scattering [182]. As stated before, IR and Raman spectroscopies provides fingerprints of chemical bonds of the samples. Additionally, size and surface charge features of nanomaterials are very important characteristics to estimate their colloidal stability in aqueous conditions [183].

The characterization of BNNTs was also performed with UV/Vis spectroscopy and FT-IR as spectroscopic techniques. In UV/Vis spectroscopy, the BNNTs showed high absorption around 190 nm, which is the B-N bond specific wavelength, as shown in Figure 4.2. Moreover, they were assessed in a wide range of wavelength (190-590 nm) and the lack of extra peaks in the spectrum is attributed to the purity of the sample in the extent of these wavelengths.

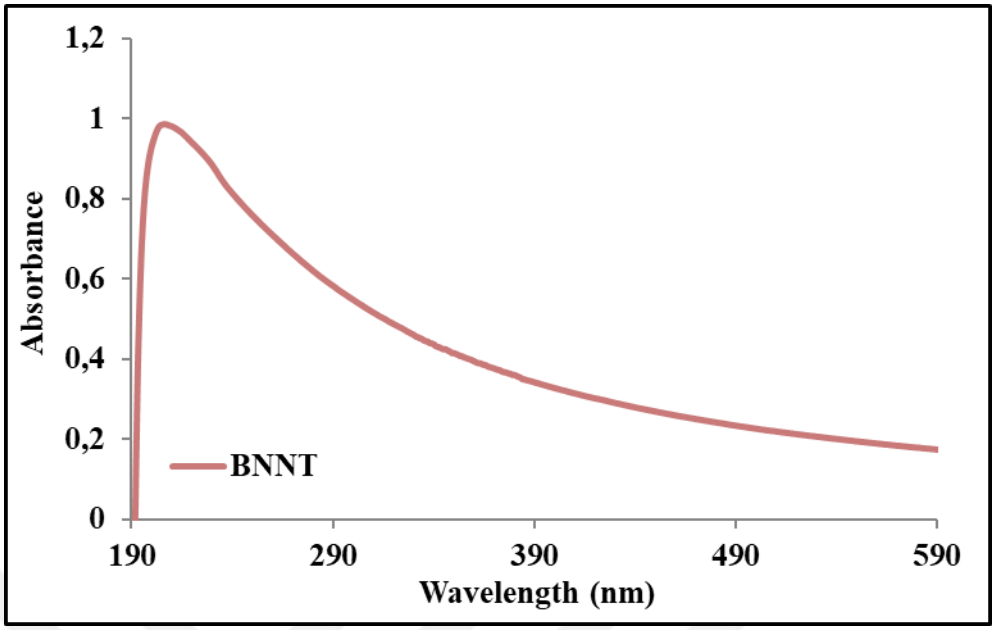

Figure 4.2. UV/Vis spectroscopy of BNNTs.

The FT-IR spectra shows the specific BNNT peaks around 1364 and 820 cm^{-1} that are attributed to the B-N and B-N-B vibrations, respectively (Figure 4.3.). Furthermore, lack of other significant peaks claims the high purity of the sample.

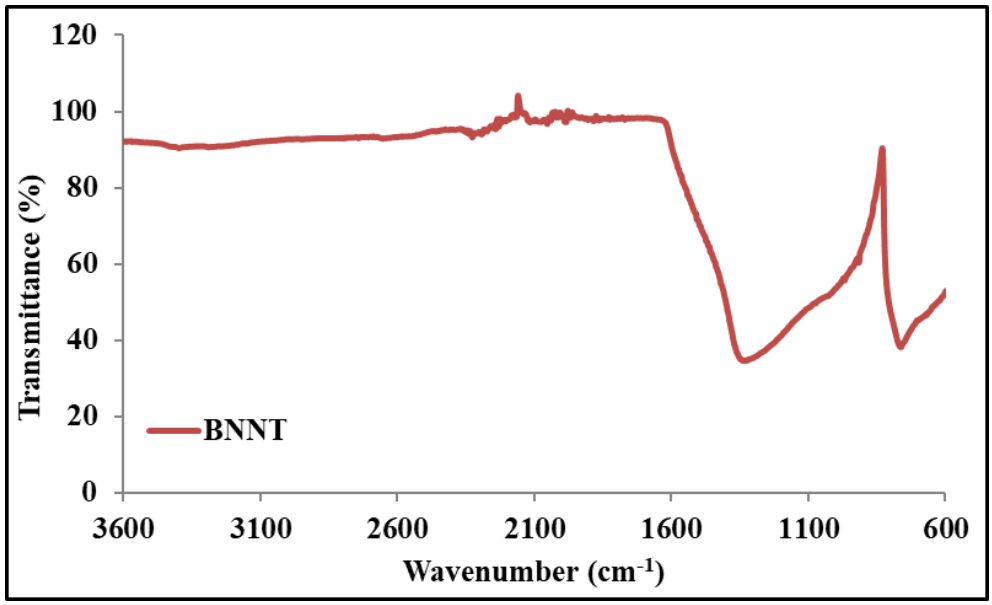

Figure 4.3. FT-IR spectroscopy of BNNTs.

4.1.2. Characterization of Functionalized BNNTs

High hydrophobicity of BNNTs hinders their use in medical and biomedical applications [184]. A strategy to make BNNTs dispersible in aqueous media is their covalent modification. In this study, BNNTs were first hydroxylated with a hydrogen peroxide treatment procedure. This procedure generates -OH groups at defects and edges of the BNNTs, which can be used for further modification. Glutaraldehyde was used as a cross-linker between the -OH groups of hydroxylated BNNTs with other carbohydrate species including glucose, lactose and starch. The TEM images of the BNNTs, before and after hydroxylation procedure are given in Figure 4.4. In the TEM images, some damages to BNNTs, shown with a black arrow on the image, are most probably ascribable to the –OH functionalization (Figure 4.4b).

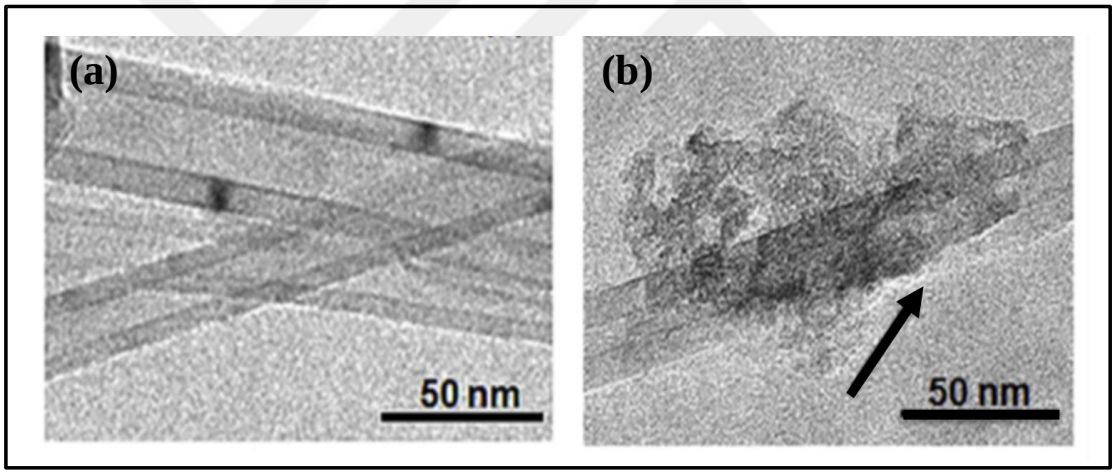

Figure 4.4. TEM images of the BNNTs (a) and h-BNNTs (b).

The covalent modification was evaluated with FT-IR. As seen on Figure 4.5, the FT-IR spectra demonstrate a broad peak in the range of 3000–3600 cm^{-1}, which is attributed to -OH group vibrations of the carbohydrates. While this band is absent on the pristine BNNT spectrum, the band becomes clear after the hydroxylation and the carbohydrate modifications. This band is more evident in starch-modified BNNTs, because of the large size of the starch molecule with respect to glucose and lactose. A band attributed to the asymmetric C-H stretching vibrations originating from carbohydrates was also observed at around 2930 cm^{-1}.

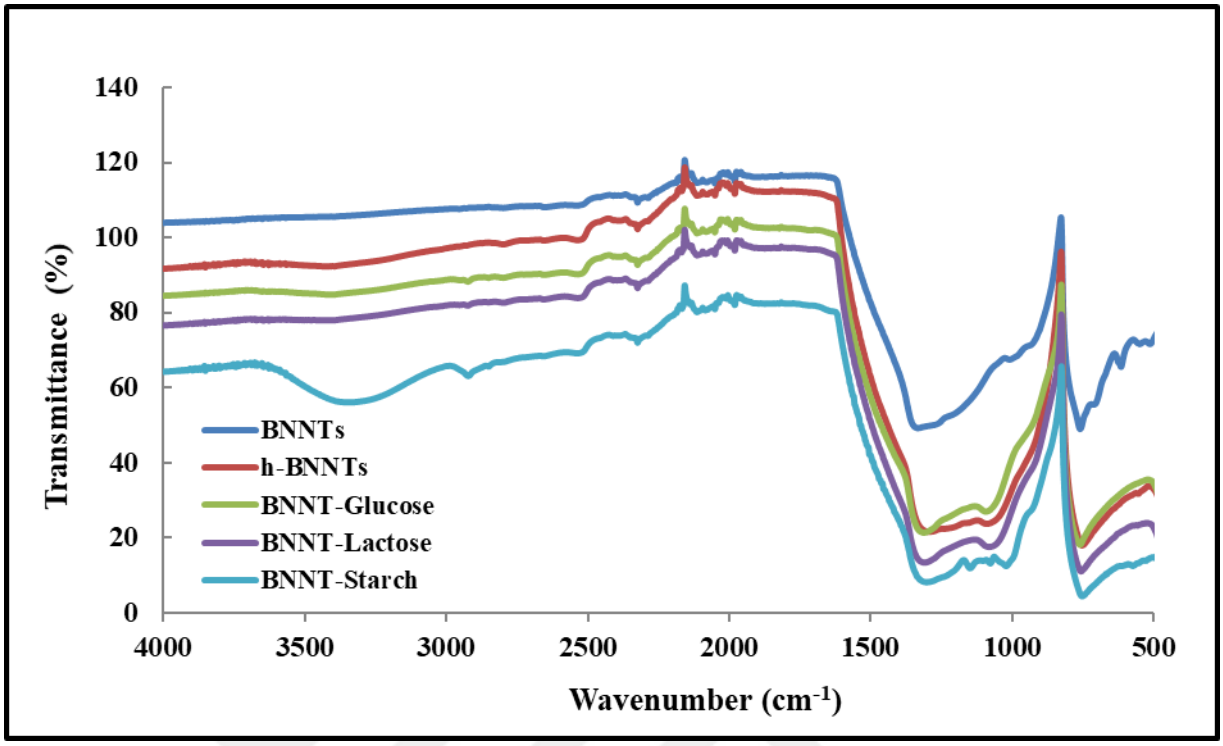

Figure 4.5. FT-IR spectroscopy of BNNTs, h-BNNT, BNNT-Glucose, BNNT-Lactose and BNNT- Starch

The amount of carbohydrates bound to the BNNTs was determined with TGA. The BNNTs are, by nature, highly resistant against heat degradation. Therefore, as seen in Figure 4.6, a decrease in the weight of pristine BNNTs was not appreciable when the temperature increases, because the structure of BNNTs does not degrade up to 800°C. On the contrary, the weight loss in glucose-modified BNNTs was about 9 per cent, about 4 per cent weight for lactose, and 5 per cent for starch-modified BNNTs. This observation suggests that a higher amount of glucose is bound to the BNNT surfaces with respect to the other investigated carbohydrates. This finding can be explained with a more efficient binding of glucose molecules to the -OH groups on the BNNT surfaces, most probably because of its small size.

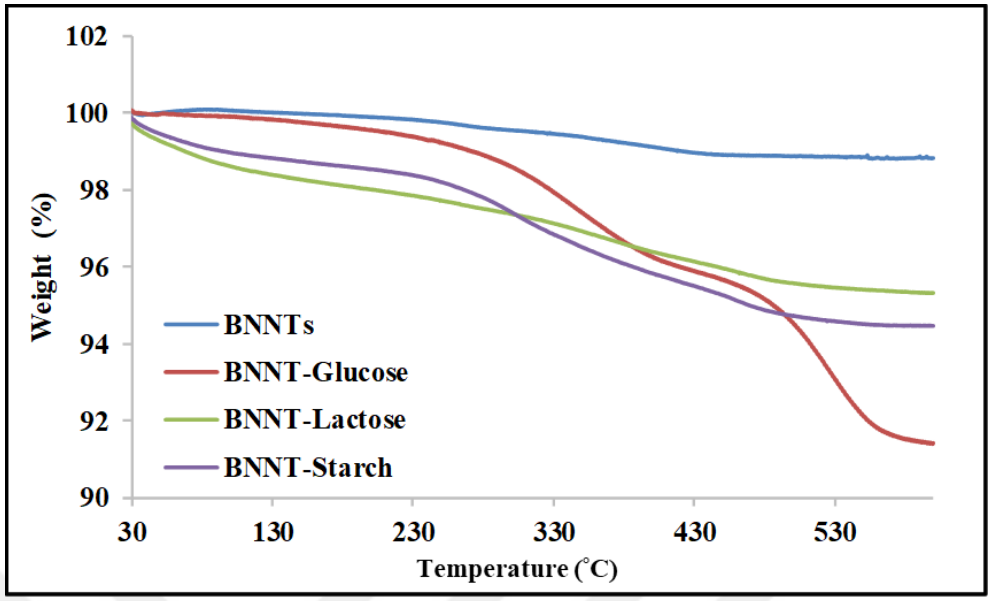

Figure 4.6. TGA measurements of BNNTs, BNNT-Glucose, BNNT-Lactose and BNNT-Starch

4.1.3. Cellular Uptake and Biocompatibility of BNNTs, h-BNNTs and m-BNNTs on Mammalian Cells

4.1.3.1. Cellular Uptake of BNNTs, h-BNNTs and m-BNNTs

Confocal microscopy images were acquired to analyze the internalization of BNNTs in the cells. Since BNNTs show no fluorescent properties, a fluorescent dye, DAPI, was selected to track the cellular uptake of BNNTs. It was found that DAPI non-covalently interacts with BNNTs, h-BNNTs and m-BNNTs, this allowing their tracking under confocal microscopy. As the chemical structure of DAPI presents several amino groups and aromatic rings, it is not surprising to see some DAPI molecules binding the BNNT surfaces. While only DAPI-stained cell nuclei were detectable in control cells, the cells incubated with DAPI-labeled BNNTs clearly showed fluorescence not only in cell nuclei, but also in the cytosols (Figure 4.7). The two reasons can be the origin of the fluorescence in the treated cell nuclei. Since the BNNTs–DAPI complexes are formed through non-covalent interactions, DAPI molecules might have separated upon their up-take into the cells. On the other hand,

BNNTs–DAPI complexes might have moved into the cell nuclei directly after being internalized by the cells. A549, lung cancer cells, have higher uptake capacity compared to healthy cells, because of their higher nutrition requirement for proliferation and growth. Thus, they are likely to internalize more material with respect to healthy cells. Additionally, it is known that the cellular uptake of hydrophobic materials shows lower efficiency with respect to hydrophilic materials [185]. Therefore, it is assumed that the interaction between BNNTs and medium proteins in cell culture media, and their covalent modification with hydroxyl groups and carbohydrates, enhances its cellular uptake by increasing its hydrophilicity.

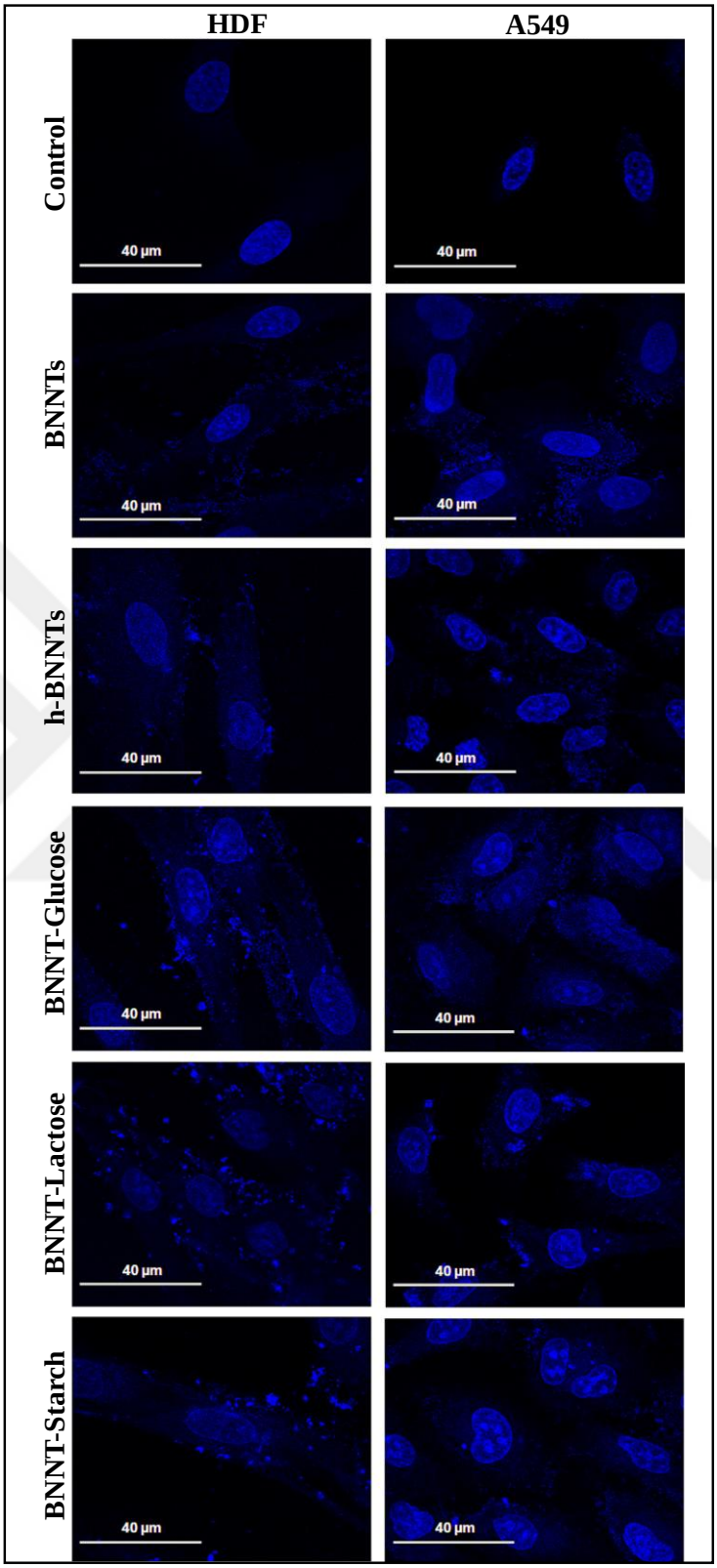

Figure 4.7. Confocal images of HDF and A549 cells treated with DAPI-stained BNNTs, h-BNNTs and m-BNNTs (BNNT-Glucose, BNNT-Lactose and BNNT-Starch)

4.1.3.2. Cell Viability of BNNTs, h-BNNTs and m-BNNTs Treated Cells

The comparative cytotoxicity assessment of BNNTs, h-BNNTs, and m-BNNTs on HDFs and A549 cells are given in Figures 4.8-4.10. The HDFs and A549 cells were treated with the BNNTs, h-BNNTs and m-BNNTs at increasing concentrations (5-200 μg/mL) for different incubation times (1-3 days). Figure 4.8a shows results for the BNNT-treated HDFs, while Figure 4.8b shows BNNT-treated A549 cells. As it can be seen, whereas BNNTs non-significantly affect the viability and the proliferation of the HDFs, they considerably decrease the viability of A549 cells at higher concentrations (100 and 200 μg/mL). The A549 cell viability decreased to 40 and 60 per cent, while the HDF cell viability decreased to 90 per cent at 2 and 3 days of the incubation with BNNTs.

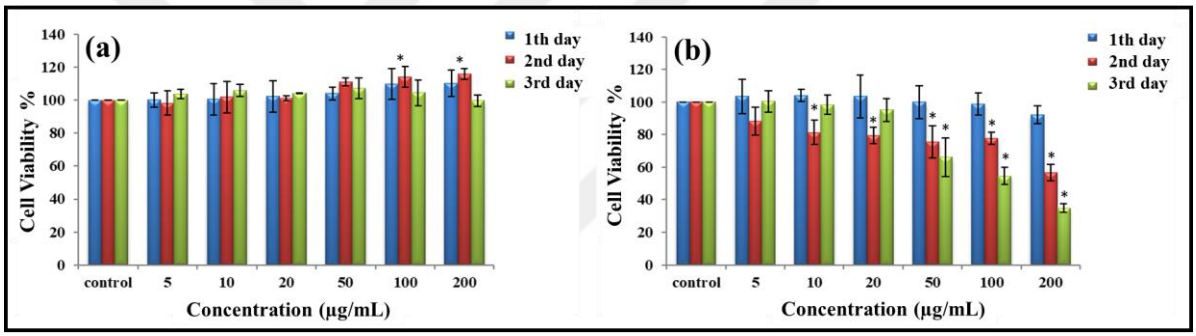

Figure 4.8. Cell viability measurement of BNNT exposed HDF and A549 cells. (analyzed with student *t*-test $^{*}p < 0.05$)

In Figure 4.9a, images show results for the h-BNNT-treated HDFs, while Figure 4.9b shows h-BNNT-treated A549 cells. As it can be seen, whereas BNNTs non-significantly affect the viability and proliferation of the HDFs, they considerably decrease the viability of A549 cells at higher concentrations (100 and 200 μg/mL). The A549 cell viability decreased to 35 and 66 per cent, while the HDF cell viability decreased to 92 per cent at 2 and 3 days of the incubation with h-BNNTs.

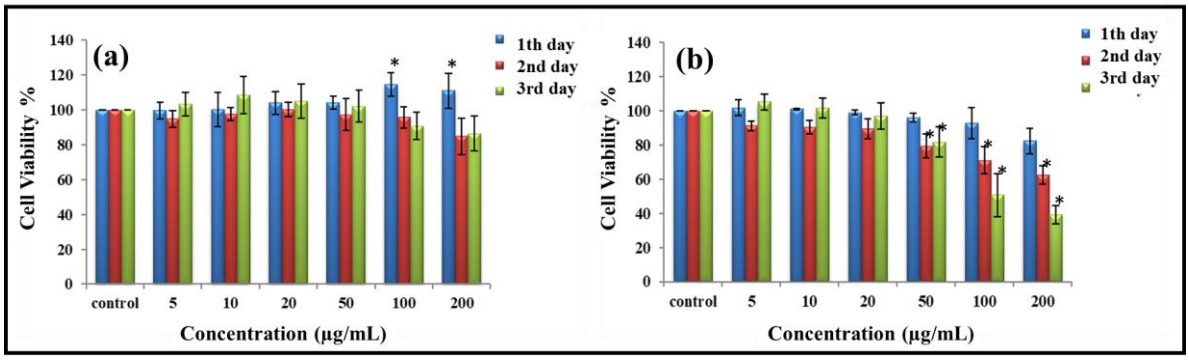

Figure 4.9. Cell viability measurement of h-BNNT-treated HDFs and A549 cells. (analyzed with student *t*-test $^{*}p < 0.05$)

Figure 4.10a, c and e show results about m-BNNTs (glucose, lactose and starch-BNNT)-treated HDFs, while Figure 4.10b, d and f show m-BNNTs-treated A549 cells. As it can be seen, each type of m-BNNTs non-significantly affected viability of HDFs and A549 cells apart from the high concentration (200 µg/mL) of BNNT-Lactose and BNNT-Starch. Although it is already known the carbohydrate modification stimulates the selective uptake of nanoparticles by cancer cells, the high cell viability could be attributed to the positive effects of the carbohydrates on viability of cells [186].

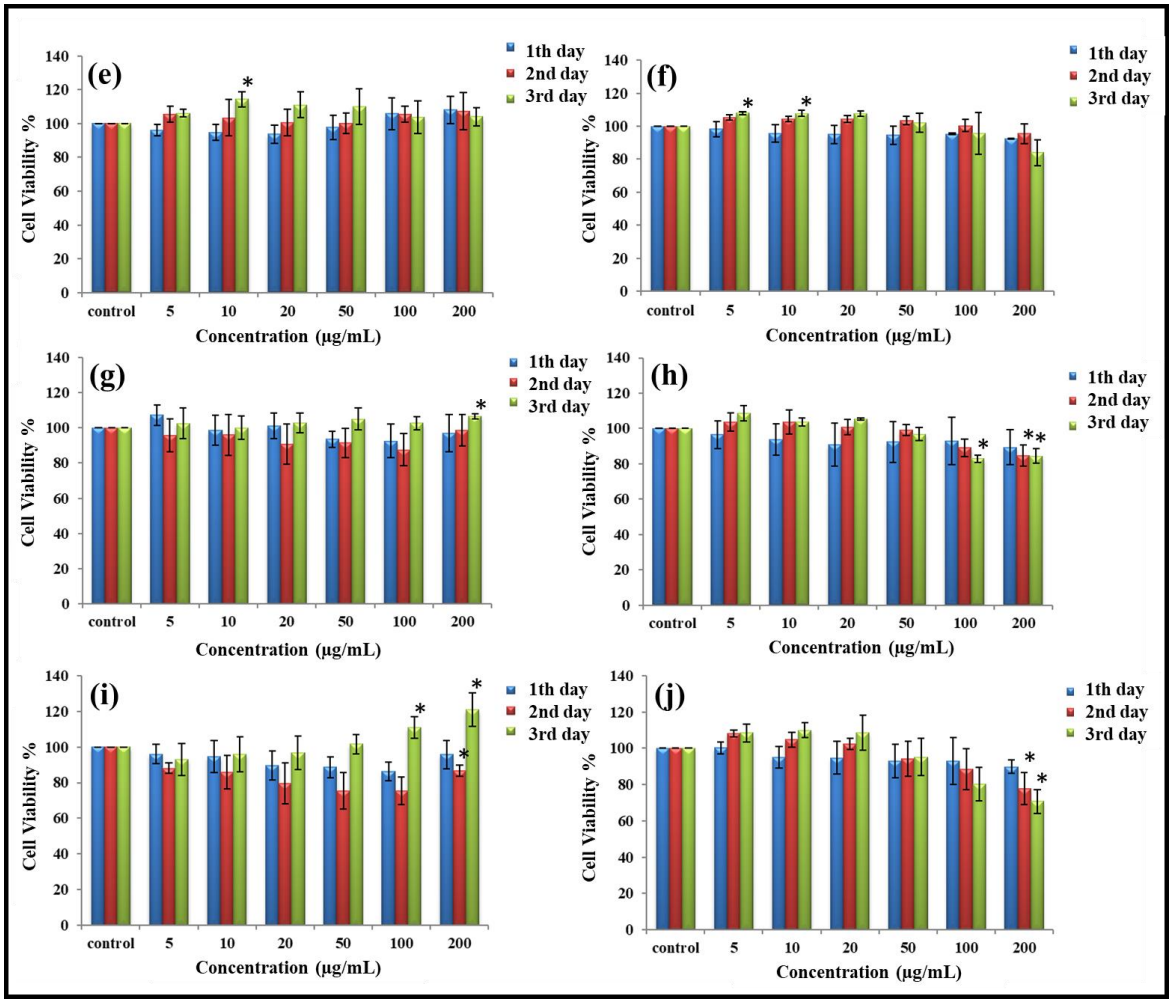

Figure 4.10. Cell viability measurement of m-BNNT (BNNT-Glucose, BNNT-Lactose and BNNT-Starch) treated HDFs and A549 cells. (analyzed with student *t*-test $^{*}p < 0.05$)

According to the cellular uptake outcomes depicted in Figures 4.8-4.10, the lower viability of A549 cells exposed to BNNTs and h-BNNTs can be explained with the fact that the two cell lines do not have the same uptake capacity. The A549, lung cancer cells, take up more BNNTs and h-BNNTs because of their higher nutrition requirement for their fast proliferation. Therefore, BNNTs and h-BNNTs show toxic effects on A549 cells because of a final higher content inside the cells. In addition, the decreased viability of the h-BNNT-treated HDFs and A549 cells at increased incubation times also could be attributed to increased uptake of the h-BNNTs because of their higher interactions with the cells owing to the presence of -OH groups [187]. Moreover, the high viability of A549 cells at high m-BNNT concentrations could be explained with the proliferative effects of carbohydrates on cancer cells despite the increased cellular uptake of m-BNNTs [186].

4.1.3.3. ROS Production of BNNTs, h-BNNTs and m-BNNTs Treated Cells

When cells are exposed to foreign substances, they tend to increase ROS production as a defense mechanism [188]. The increased ROS levels cause cellular stress that stimulates further ROS production. High ROS levels in the cells causes damages in the structure of many components such as proteins, membrane lipids, and DNA. These alterations might result into many important degenerative diseases [189]. The ROS detection was performed to analyze whether BNNTs, h-BNNTs, or m-BNNTs cause any cellular stress that could trigger death mechanism of A549 cells. The cells were treated with DCFDA, ROS detection reagent, and they were exposed to BNNTs, h-BNNTs and m-BNNTs at increasing concentrations (5-200 μg/mL) for 4 h. As seen in Figure 4.11, the ROS production significantly increased in BNNT and h-BNNT treated cells up to 60 and 70 per cent, while the ROS production was increased around 25 and 36 per cent in m-BNNT treated cells, with respect to the control cultures. As already provided by the cell viability assays, the ROS detection assay results indicate that the cellular uptake of BNNTs and h-BNNTs at high doses decrease cell viability, and this decrement is correlated to an increased oxidative stress in A549 cells. Despite the m-BNNT treated cells viability decrease was respectively lower that correlated with the respectively low ROS production indicates the stress in m-BNNT exposed cells.

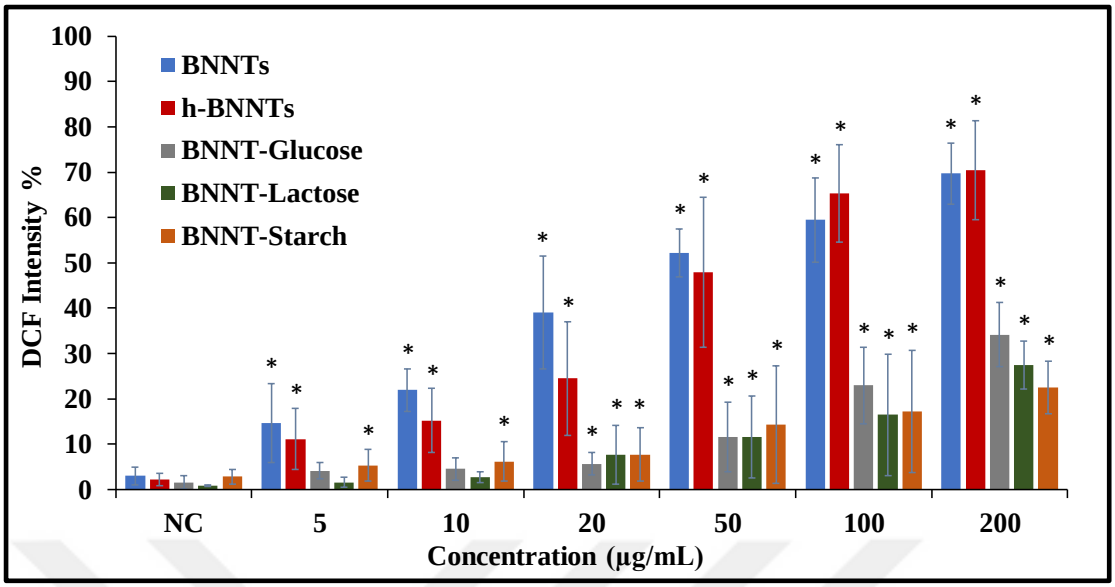

Figure 4.11. ROS detection assay on BNNT, h-BNNT and m-BNNT (BNNT-Glucose, BNNT-Lactose and BNNT-Starch) treated A549 cells. (analyzed with student *t*-test $^{*}p < 0.05$)

4.1.3.4. Genotoxicity of BNNTs, h-BNNTs and m-BNNTs

The comet assay, a single cell gel electrophoresis method used for the genotoxicity assessment, provides detection of DNA damage in single cells [190]. The DNA damage in the cells can be detected from the length of the smear structure of the whole cell DNA. that means the tail length occurring after single cell gel electrophoresis. The different size of DNA fragments occurring following DNA damages leads to a stretch of the smear structure. The smear structure of the cells was analyzed with the Comet IV software. In Figure 4.12, we can see as BNNT and h-BNNT treated cells tail lengths were approximately 38 per cent, while the m-BNNT exposed cell tail lengths were 20 per cent and 30 per cent if compared to the positive control cells, which were exposed to hydrogen peroxide: these results indicate that the increased ROS levels in the cells are responsible of the DNA damage.

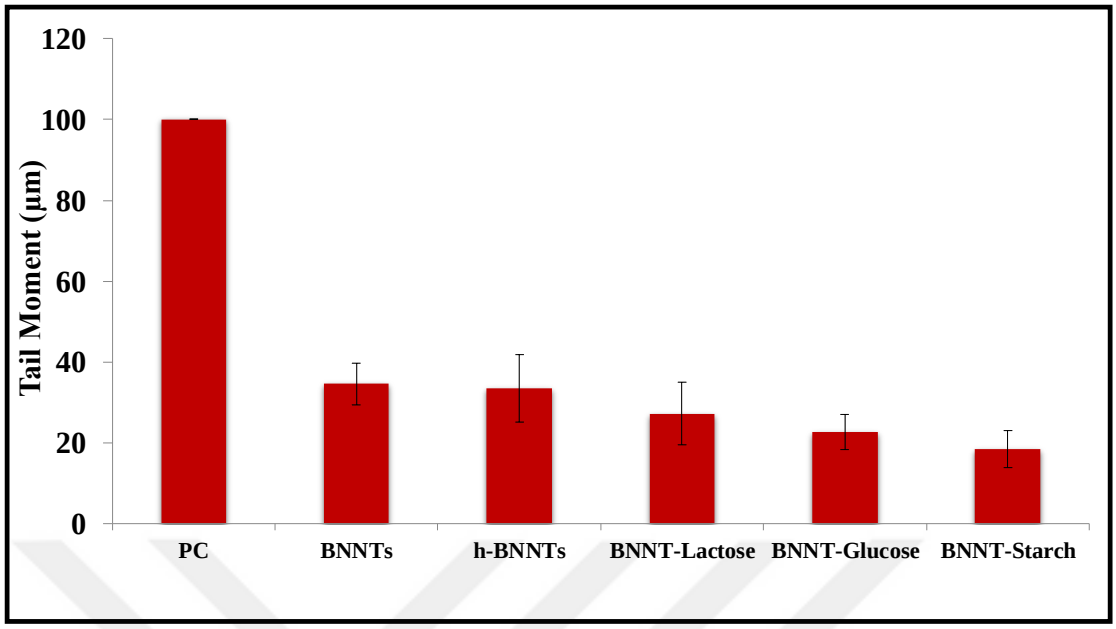

Figure 4.12. Comet assay on BNNTs, h-BNNTs and m-BNNTs (BNNT-Glucose, BNNT-Lactose and BNNT-Starch) treated A549 cells.

4.1.4. Biocompatibility of h-BNNTs on Microorganisms

The application of living microbial cells as molecular engines for a variety of biotechnological applications, including cell-based biosensing, is an ongoing research effort. However, there are significant difficulties to be overcome, such as the non-biocompatible structures in contact with the microbial cells, and the weak efficiency of developed systems. In this study, we demonstrate the biocompatibility of interfacing hydroxylated boron nitride nanotubes (h-BNNTs) with live yeast cell surfaces. H-BNNTs were incorporated with polyelectrolytes (PEs) using a layer-by-layer deposition onto live *Saccharomyces cerevisiae* cells, as schematized on Figure 4.13. PEs and h-BNNTs coated yeasts were characterized using DLS and FTIR as spectroscopic and SEM as imaging techniques.

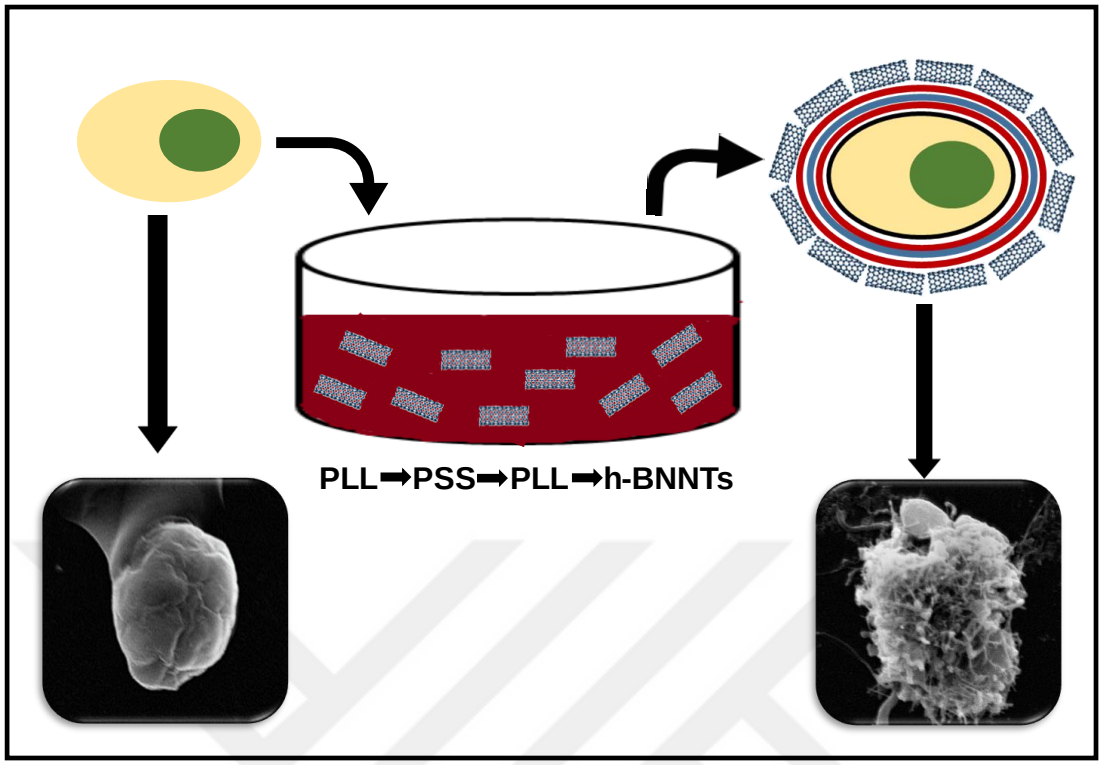

Figure 4.13. Schematic representation of PEs (PLL-PSS-PLL) and h-BNNTs coated yeasts.

4.1.4.1. Characterization of LbL-PEs and h-BNNTs Coated Yeasts

Phosphate residues of the mannoproteins in the cell wall of yeasts play an important role in determining their anionic surface charge [191]; the yeast cell surface charge, moreover, consequently shows differences in terms of positive or negative potential depending on the charge of the PEs coated around the yeasts as shown in Table 4.1. By comparing the bare yeast surface zeta potential to that one of the PE-coated cells, it is therefore possible to confirm successful encapsulation. LbL deposition of the PEs shell around yeasts was analyzed by measuring the zeta potential of bare and PEs-coated cell surface. The zeta potential of bare yeast is approximately -23.0 ± 0.8 mV due to the carbohydrate residues providing the highly negative charge of the yeast cell surface. After the PLL was coated on the surface of the yeast cells, it is supposed that the amino groups in the structure of the PLL interacted with the phosphate groups of the cell wall structure, and changes surface charge of the cells toward higher values (-1.0 ± 0.2 mV). Next, the deposition of the PSS on the PLL-encapsulated yeast cells provided more negative features (-7.0 ± 1.1 mV) because of

the sulfonate groups in their structures. Lastly, the deposition of the PLL on the PLL/PSS encapsulated cells reverses the zeta potential of the cell surface again to positive values (+3.0 ± 0.7 mV). According to the zeta potential results, we can therefore state that the LbL PEs coating on the surface of the yeast cells has been successfully performed.

Table 4.1. Surface charge of bare yeast and PE-coated yeasts.

	Bare yeasts	**PLL**	**PLL/PSS**	**PLL/PSS/PLL**
Zeta Potential (mV)	-23.0 ± 0.8	-1.0 ± 0.2	-7.0 ± 1.1	+3.0 ± 0.7

The LbL deposition of PEs and the adsorption of h-BNNTs on the yeast surface were evaluated by FTIR following each layer absorption, and eventually after that h-BNNTs were deposited on the yeast surface (Figure 4.14). The FTIR spectra show strong peaks at around 1156 cm^{-1} and 1550 cm^{-1}, which are attributed to the C-O-C, C-C, and C-OH bond vibrations, which are characteristic in the structure of pyranose rings of glucan proteins in the yeast cell wall structure [192]. However, these peaks are suppressed by BNNT-specific peaks in the range of 700–1600 cm^{-1} in the PLL/PSS/PLL/BNNT-OH coated yeasts. The broad peak in the range of 3000–3600 cm^{-1} is attributed to the -NH and -OH groups of PLL and BNNT-OHs, respectively.

Our results confirm the successful encapsulation of yeast in the h-BNNT-based PEs shells. Furthermore, the hindering of the -NH peak in PLL/PSS-coated samples demonstrates the yielding of PSS layer on the PLL coated cells, by repressing the -NH peaks belonging to PLLs.

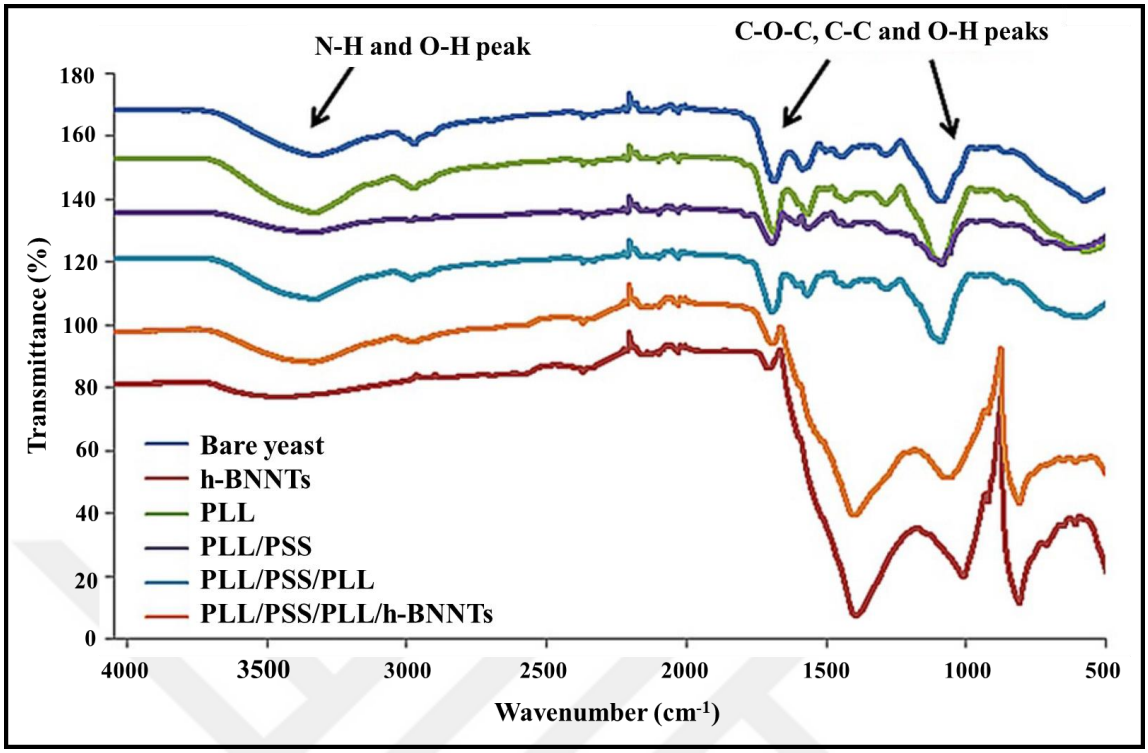

Figure 4.14. FT-IR spectra of bare yeast, h-BNNT, PLL, PLL-PSS, PLL-PSS-PLL and PLL-PSS-PLL-h-BNNT-coated yeasts.

Bare yeasts, PEs and h-BNNTs modified yeasts were then observed with SEM (Figure 4.15). The surface of the bare yeasts is smooth (Figure 4.15a), whereas we can clearly see the layers around the cells are getting thicker following each PE coating process (Figure 4.15b, c and d). Then, well-structured yeast surface coated with a dense layer of PEs surrounded by h-BNNTs is shown in Figure 4.15e. The average diameter of the PEs and h-BNNTs encapsulated yeast cells increased to approximately up to 5.8 μm, as compared to their bare form that is approximately 4 μm.

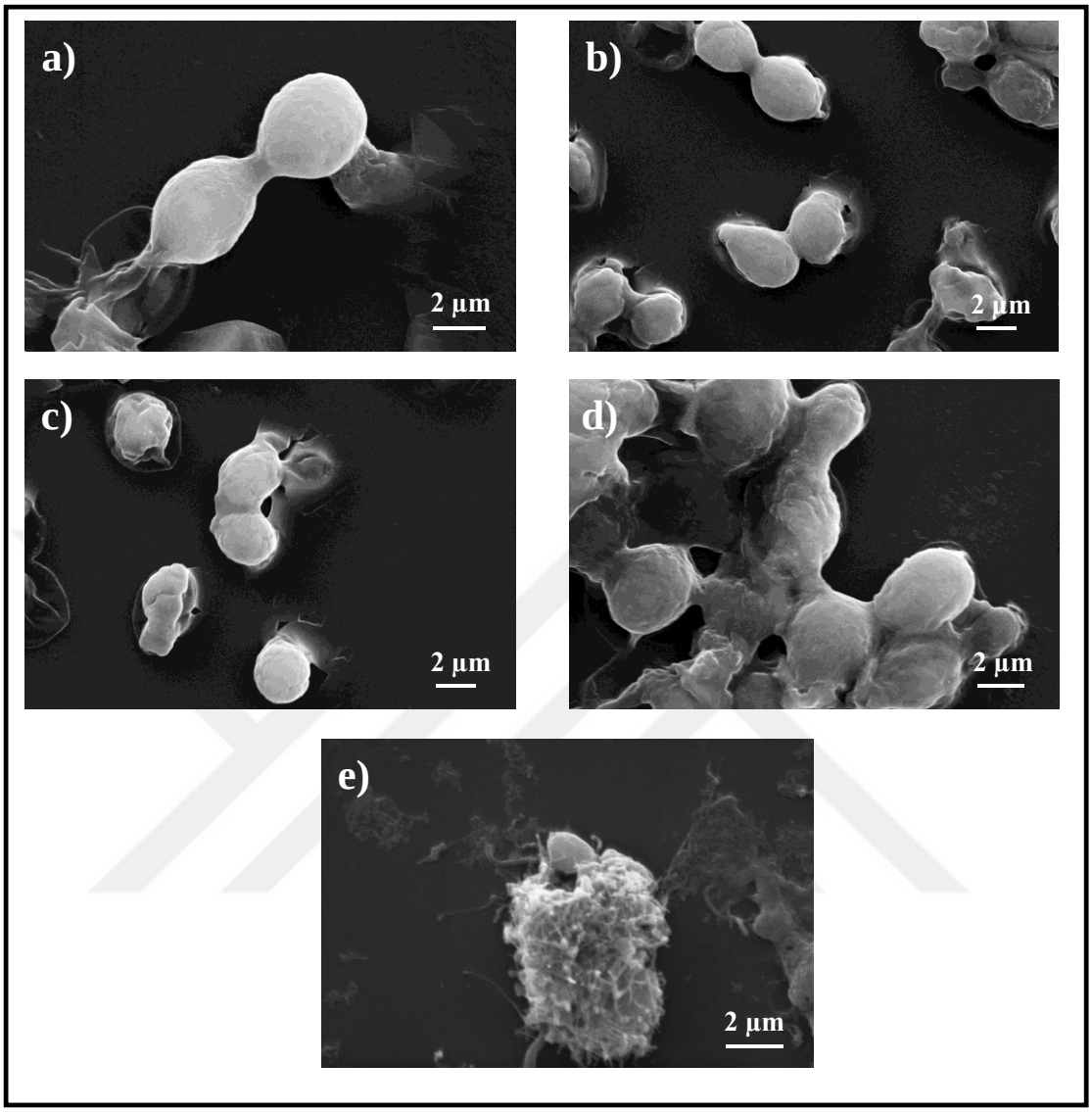

Figure 4.15. SEM images of bare (a), PLL (b), PLL-PSS (c), PLL-PSS-PLL (d) and PLL-PSS-PLL-h-BNNTs (e) coated yeasts.

4.1.4.2. Biocompatibility of LbL-PEs and h-BNNTs Coated Yeasts

The biocompatibility of h-BNNTs coating approach was assessed to show the possible exploitation in biotechnological applications. The yeast viability was tested with a WST-1 colorimetric assay after one day of incubation in their bare and adsorbed form with each layer of PEs and h-BNNTs (PLL, PLL/PSS, PLL/PSS/PLL and PLL/PSS/PLL/h-BNNTs) (Figure 4.16). As observed in previous experiments, the PEs and h-BNNTs coating

significantly affect cell viability [193]. Although the PLL coated cell viability decreased, PSS and h-BNNT coating of cells increased the viability significantly. Finally, the h-BNNTs adsorption on the yeast surface resulted biocompatible with cells, thus making this approach convenient for biotechnological applications.

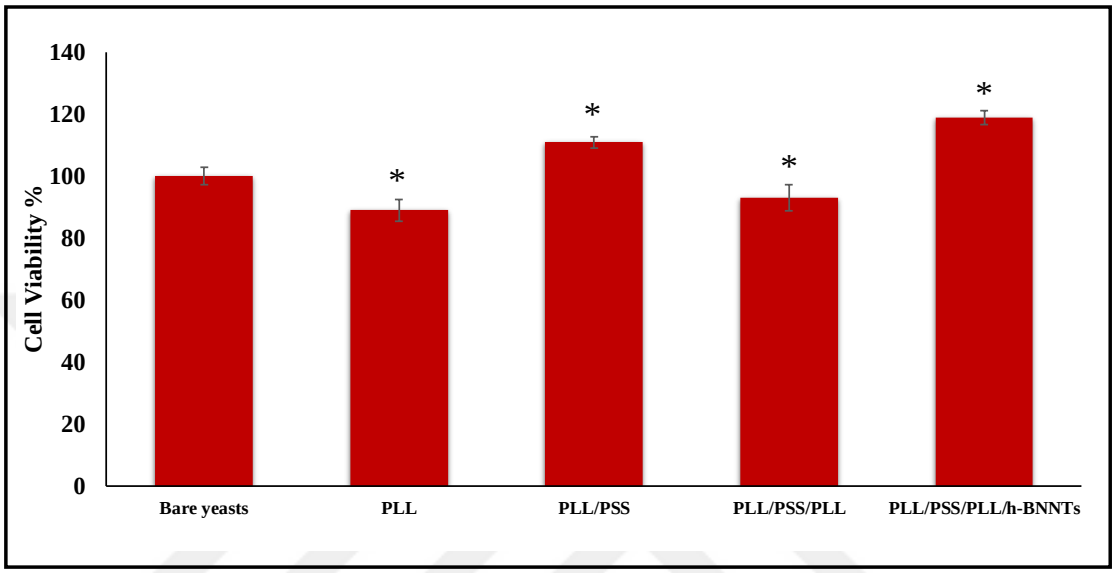

Figure 4.16. Cell viability results of bare, PLL, PLL-PSS, PLL-PSS-PLL and PLL-PSS-PLL-h-BNNT coated yeasts. (analyzed with student *t*-test $^{*}p < 0.05$)

4.2. SYNTHESIS AND BIOCOMPATIBILITY OF hBNs

4.2.1. Characterization of hBNs

Synthesized hBNs were observed by using SEM and TEM as imaging techniques, as shown in Figure 4.17. The SEM and TEM images showed a platelet-like structures of the hBNs. The size and morphology of the synthesized hBNs are uniform, being the lateral size dimension is around 50 nm. Lack of the impurities around the hBNs shows the production of hBNs without contamination.

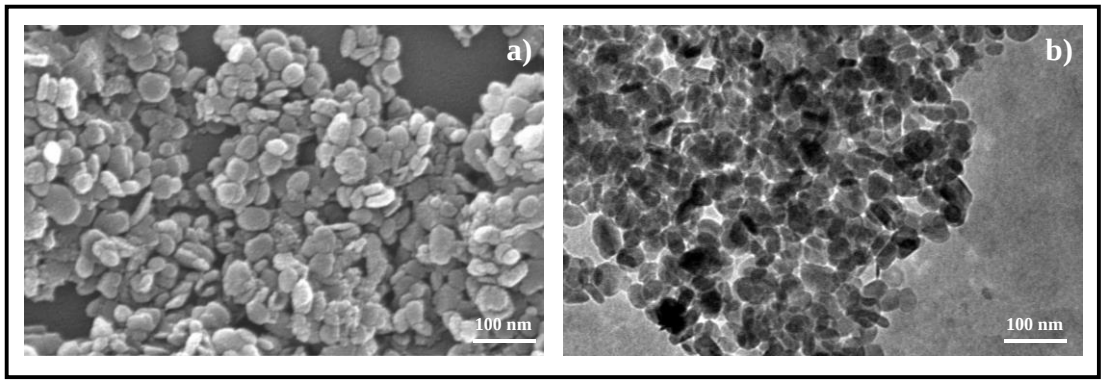

Figure 4.17. SEM (a) and TEM (b) images of the hBNs.

The spectroscopic characterization of the hBNs was performed using UV-Vis, FT-IR and Raman spectroscopy. As shown in Figure 4.18, the UV-Vis spectrum of the hBNs indicates a maximum absorbance at around 200-220 nm, that is attributed to the specific B-N bonds in hBNs. Furthermore, the lack of extra peaks in the spectrum is attributed to the purity of the sample in the extent of these wavelengths.

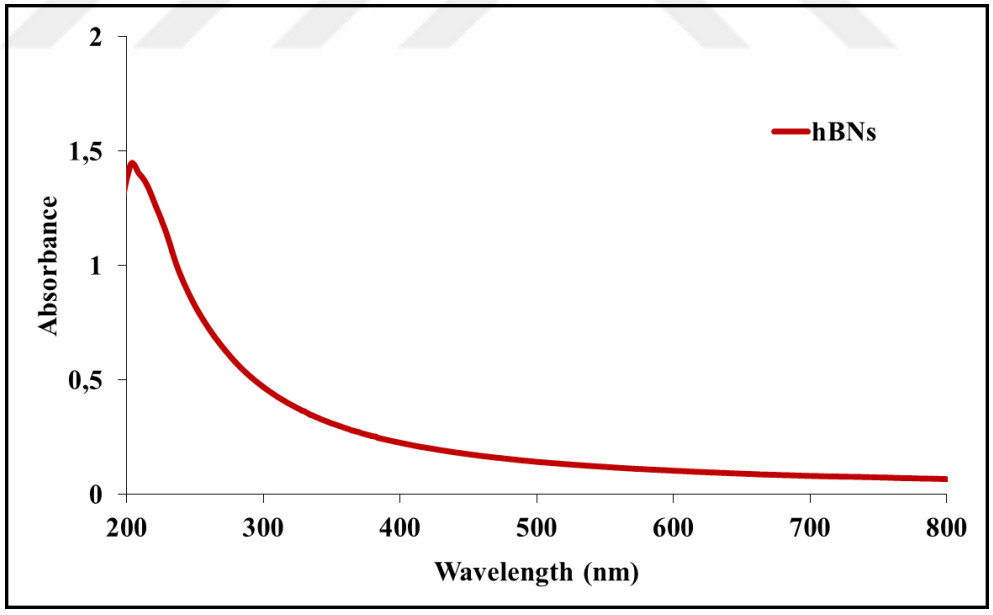

Figure 4.18. UV/Vis spectroscopy of the hBNs.

The FT-IR spectra of the hBNs show broad peaks at around 1364 and 820 cm^{-1} that is attributed to the B-N and B-N-B vibrations, respectively (Figure 4.19). Furthermore, a lack

of other peaks in the spectrum, especially at around 3400 cm^{-1} attributed to -OH stretching, claims the low degradation capacity of the hBNs as a degradation tendency indicator [90].

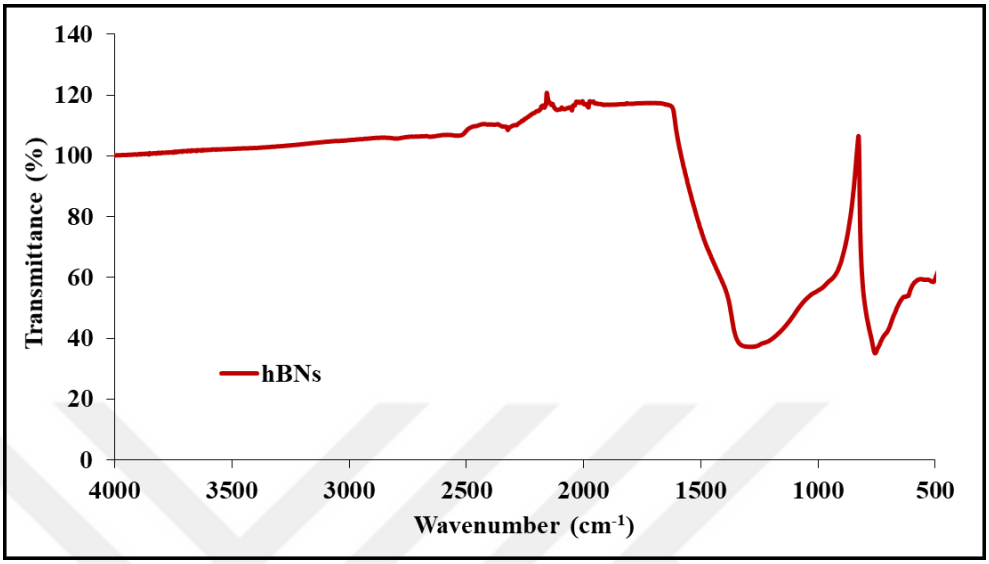

Figure 4.19. FT-IR spectrum of hBNs.

Raman spectroscopy results of the hBNs indicates a sharp peak at around 803 and 1364 cm^{-1} originating from B-N vibrations as characteristic spectral features unique for boron nitrides such as hBN, as shown in Figure 4.20.

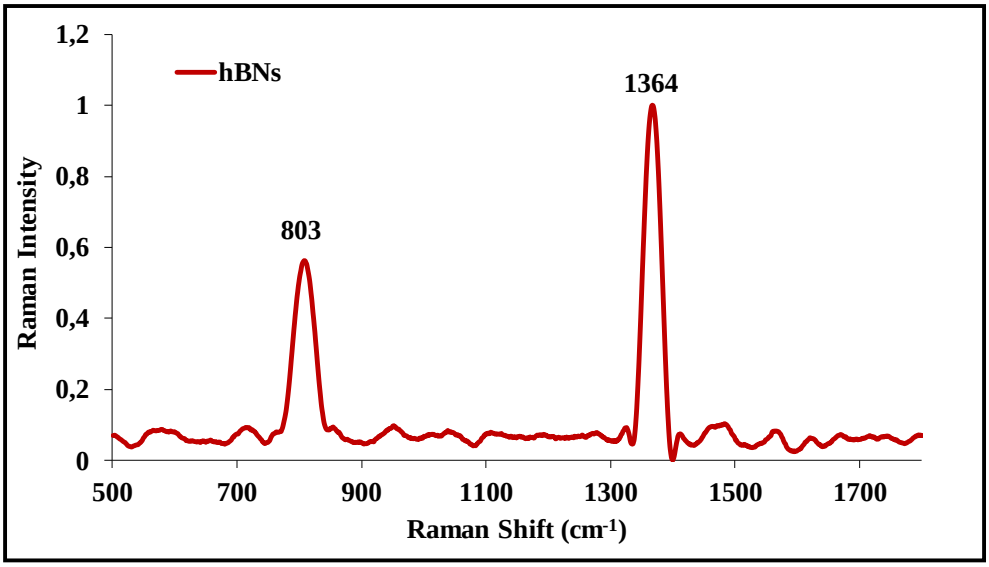

Figure 4.20. Raman spectroscopy results of hBNs.

4.2.2. Colloidal Stability of hBNs

Time-dependent changes in the hydrodynamic size of the hBNs indicate their colloidal stability. The hydrodynamic size of the hBNs was measured using DLS at the 0, 1 and 3 days of incubation in aqueous environment. As shown in Figure 4.21, hydrodynamic size of the hBNs increased up to 120 nm from 101 nm following 3 days of incubation. Moreover, we can see the peaks are broadening and maximum hBN size increased to 210 nm at the 3 day of incubation from 130 and 155 nm at the 0 and 1 day of incubation, respectively. The results indicate that the hBNs are efficiently dispersed in the water, and present narrow size distribution even after 3 days of incubation, confirming their high colloidal stability.

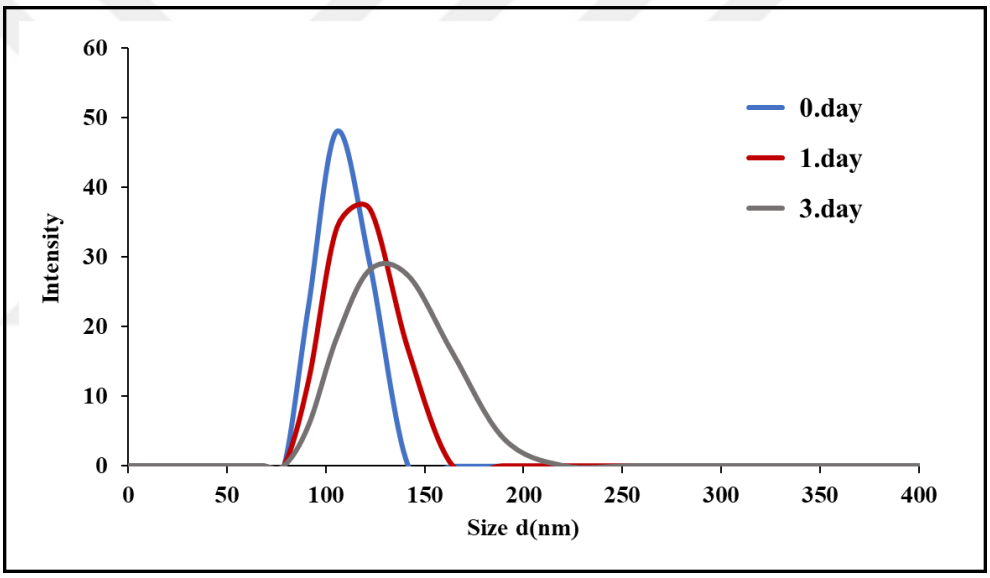

Figure 4.21. DLS measurement results concerning hBNs at 0, 1 and 3 days of incubation.

Furthermore, zeta potential of the hBNs was measured as an indicator of their colloidal stability in aqueous environment. It is known that highly charged particles repel each other and show better stability while neutral structures with a low density of charges cannot resist to attractive forces and form aggregates [194]. The zeta potentials of the synthesized hBNs in this study were measured as -10.72 ± 0.11 mV for the hBNs. This value indicates their high colloidal stability.

4.2.3. Biocompatibility of hBNs

The biocompatibility of hBNs were studied on HDF cells at increasing concentrations (25-400 µg/mL) using WST-1 colorimetric assay as shown in Figure 4.22. According to these results, the viability of the hBN-treated cells did not show significant decrease up to 300 µg/mL concentration of hBNs. The results indicate the biocompatible nature of hBNs at low concentrations for many kinds of biomedical applications.

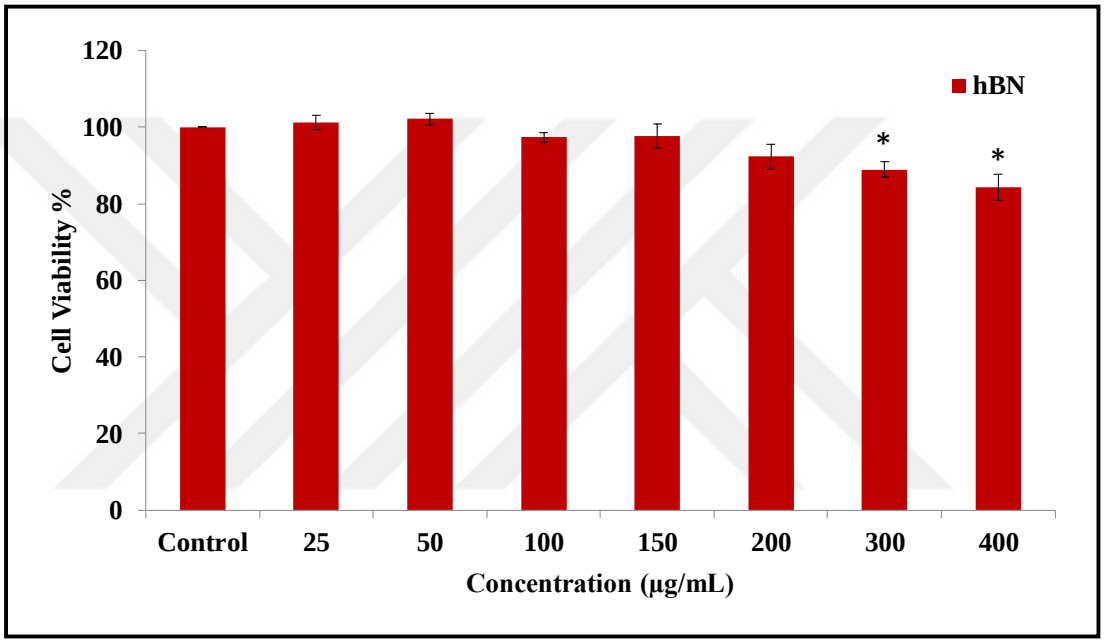

Figure 4.22. Biocompatibility of hBNs. (analyzed with student *t*-test $^{*}p < 0.05$)

4.3. BNNTs AND hBNs AS NANOCARRIERS FOR ANTICANCER DRUGS

In this study, the potential of BNNTs and hBNs as novel nanocarriers has been comparatively investigated. BNNTs have in fact become, in recent years, promising and biocompatible carriers for drug delivery [161, 195] and this study represents the latest *in vitro* validation of their potentialities. First, the interaction of both nanostructures with Dox (Dox–BNNTs and Dox–hBNs) was studied for achieving an efficient loading and following release at different pH values; thereafter, Dox–BNNTs were decorated with folate molecules

(F–Dox–BNNTs) in order to target cancer cells as schematically represented in Figure 4.23. Finally, their toxicity and cellular uptake / localization was investigated.

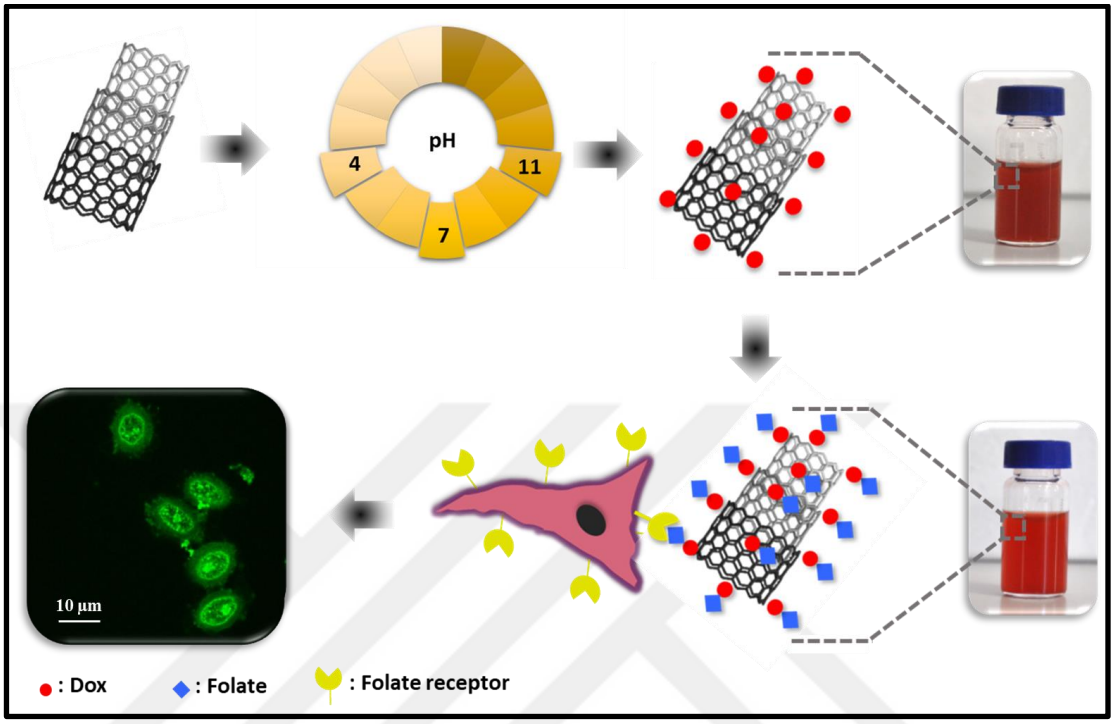

Figure 4.23. Schematical representation of Dox interaction with BNNTs and hBNs, and their cellular uptake.

4.3.1. Noncovalent Interaction of Dox with BNNTs and hBNs

Dox is a high-performance genotoxic drug used in cancer therapy; however, its high toxicity is one of its limiting properties. The use of a carrier to help in delivering drug molecules towards target cells is an ideal approach in nanomedicine to reduce toxic side effects. Among many nanostructures investigated for this purpose, there are only a few reports regarding the application of BN nanostructures for drug delivery so far. The reason behind this can be found in their limited availability and not well understood toxicity. Therefore, it was explored their possible carrier potential using Dox as a model drug. The chemical structure of Dox and a depiction of its possible interactions with B–N sidewalls are shown in Figure 4.24. As it can be seen, Dox has two phenyl rings, one amino group, three carbonyl groups, two ether groups and several hydroxyl groups in its structure (Figure 4.24a). It is possible

that the presence of aromatic rings in the structure enhances its interaction with hydrophobic BNNTs and hBNs through π-π stacking (Figure 4.24b), while amino, carbonyl, ether and hydroxyl groups may help Dox to remain in the aqueous phase. This interaction may also help to increase the dispersion of BNNTs and hBNs in an aqueous environment. While the hydrophobic part of the molecule may prefer to stay in contact with the BNNT surface, the hydrophilic functional groups may prefer the aqueous phase.

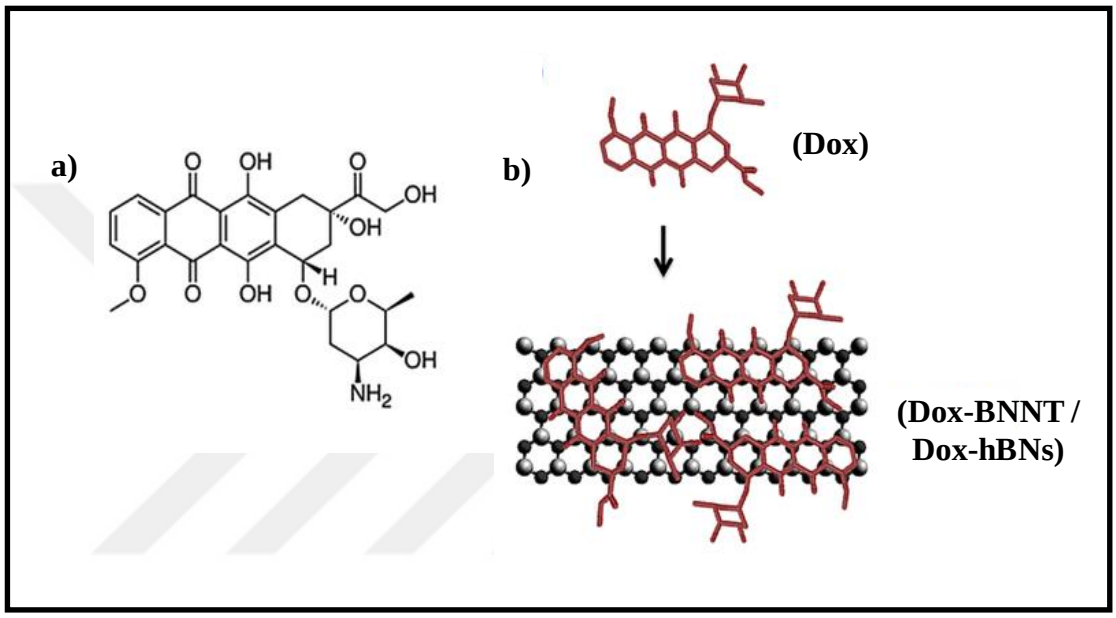

Figure 4.24. Chemical structure of Dox (a) and its possible interaction with B–N sidewalls (b).

4.3.1.1. Concentration-dependent Dox Loading Investigation on BNNTs and hBNs

The interactions of Dox with BNNTs and hBNs were studied at varying Dox concentrations to investigate the optimal concentrations showing the saturation point of BNNTs or hBNs for Dox loading. Absorption and fluorescence spectroscopies were used to estimate Dox concentration adsorbed onto the nanostructures. Dox has a maximum absorption at 480 nm and has two maximum emission at around 560 and 590 nm, which can be used to estimate its concentration onto the nanostructures and in solution [196]. In Figure 4.25, the fluorescence spectra show the comparison of the loading capacity of BNNTs and hBNs at increasing Dox concentration, while keeping the BNNTs or hBNs concentrations constant.

Note that an intensive washing procedure was applied to remove the weakly bound Dox molecules from BNNTs and hBNs. The higher is the amount of Dox complexing the nanostructures, the higher is the fluorescence intensity originating from the Dox–BNNTs, while the fluorescence intensity of Dox–hBN constructs is almost constant. Although a quenching effect of Dox fluorescence is expected upon interaction with BNNTs and hBNs, a small increase in fluorescence intensity is observed for Dox–BNNT and Dox–hBN complexes [197]. This is probably due to the release of weakly bound Dox molecules into aqueous phase, or to an incomplete quenching of weakly bound Dox molecules, since the interaction of Dox with the nanostructures is through noncovalent interactions. As we can appreciate from Figure 4.25a, if we consider the highest Dox concentrations (2.0, 4.0 and 5.0 mM), fluorescence spectra of Dox–BNNT complexes, suggest a drug loading saturation point, achieved for a concentration of about 5.0 mM. Conversely, all Dox concentrations (except 0.5 mM) interacting with hBNs show similar fluorescence intensity spectra (Figure 4.25b), and the saturation point is estimated to be 1.0 mM.

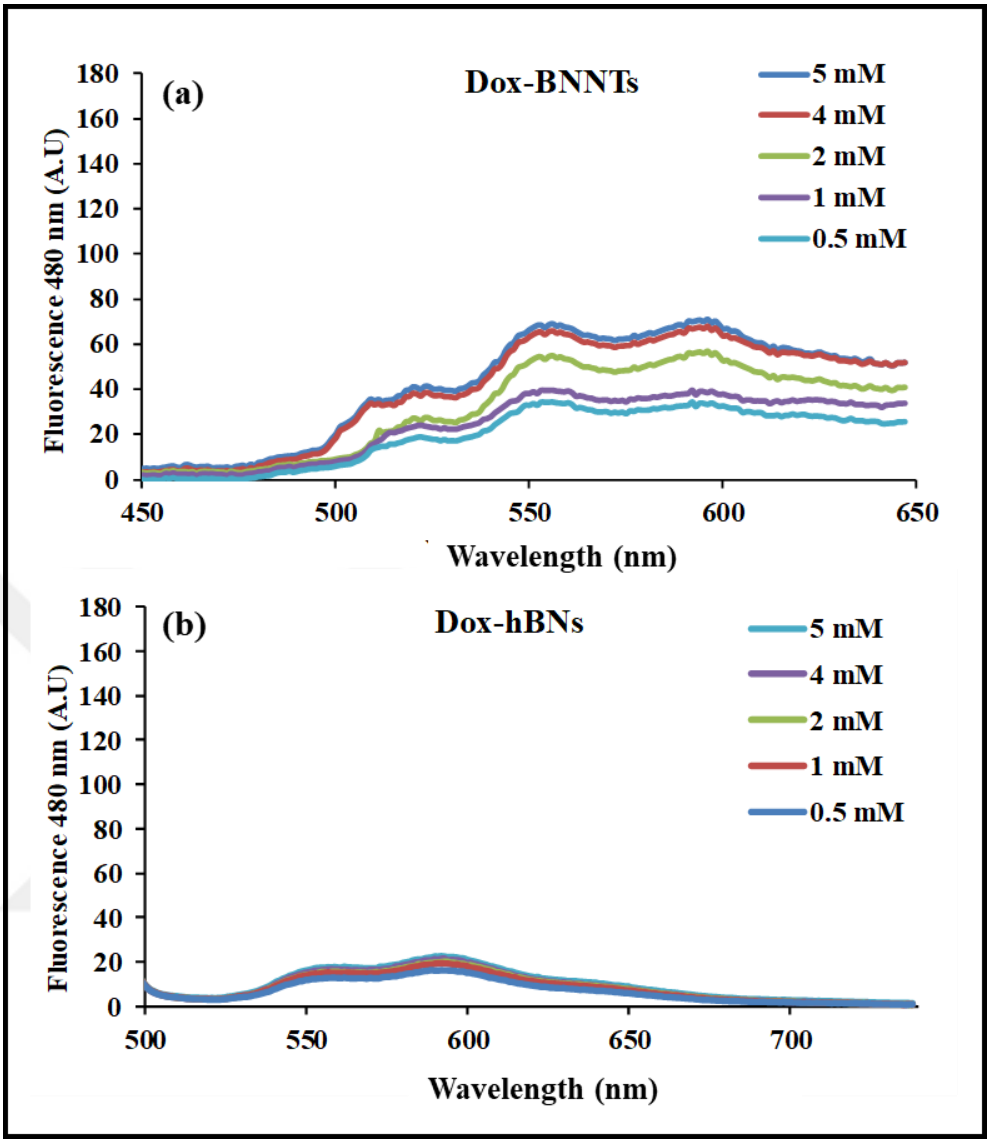

Figure 4.25. Fluorescence spectra of Dox-BNNTs and Dox-hBNs for increasing concentrations.

Furthermore, the absorption of Dox–BNNTs and Dox–hBNs was measured to confirm the data obtained from the fluorescence spectroscopy data. Note that again that an intensive washing step was applied to remove weakly bound Dox molecules from the BNNTs and hBNs. As seen from Figure 4.26, the absorption of Dox increases as the Dox concentration increases, indicating that more Dox molecules are bound to the nanostructures at increasing Dox concentration. The data from both experiments clearly indicate that the BNNTs have a superior loading capacity for Dox.

As the absorption of Dox molecules is lower upon their binding to the BNNTs, we have decided to determine the Dox loading capacity of BNNTs and hBNs from the supernatants after the incubation of BNNTs and hBNs with Dox. By combining all collected data, it was found that the Dox loading capacity was 10 wt per cent of BNNTs while 3.75 wt per cent of hBNs. This indicates that the BNNTs have about threefold higher loading capacity than hBNs.

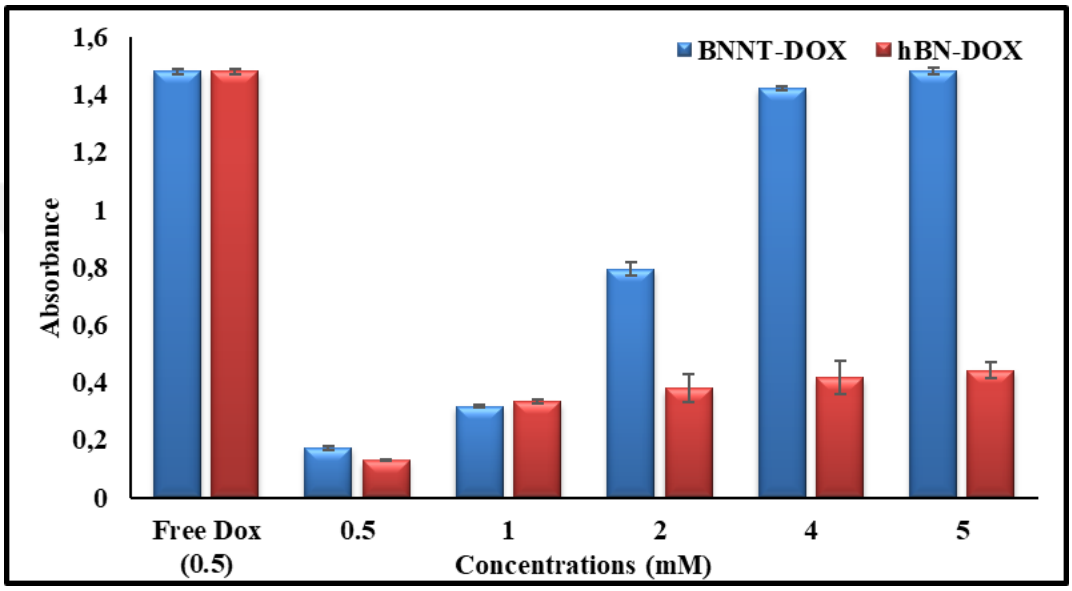

Figure 4.26. UV/Vis spectroscopy data of Dox-BNNTs and Dox-hBNs for increasing concentrations.

4.3.1.2. pH-dependent Dox Loading Investigation on BNNTs and hBNs

Next, the influence of pH on Dox loading efficiency on the nanostructures was studied. As mentioned earlier, Dox has one -NH_2 group and several ionizable -OH groups in its structure. The ionization status of these groups can have an influence on the binding efficiency of Dox. Thus, BNNTs and hBNs were conjugated with Dox in PBS at pH 4, 7 and 11. At lower pH, it is expected that the Dox is protonated owing to the -NH_2 group, which may diminish the interaction of Dox with nanostructures. As the pH increases, the number of the protonated -NH_2 groups decreases and its hydrophobicity increases, which may allow better interaction of Dox with the hydrophobic BNNTs and hBNs. On the other hand, the increased pH values

of the solution cause degradation of doxorubicin, which decreases its absorption at basic pH values [198, 199]. Note that when Dox interacts with BNNTs or hBNs, its fluorescence is quenched as indicated earlier. Again, fluorescence spectroscopy is chosen to monitor the Dox–nanostructure interactions. Figure 4.27 show the fluorescence spectra of Dox–BNNTs and Dox–hBNs at increasing pH values from 4 to 11. A 5.0 mM concentration of Dox was used to be conjugated with BNNTs and hBNs. As the pH increases, a dramatic decrease in the fluorescence intensity from Dox–BNNTs and Dox–hBNs is observed due to the improved interactions between the nanostructures and Dox molecules through π-π stacking onto BNNT sidewalls and hBNs [200]. As seen, the BNNTs show strong affinity for Dox at pH 11, while the interaction is weak at pH 4. As the solubility of Dox increases at low pH due to the protonation of free amino groups, the interaction with BNNTs becomes weaker. The inset images on the figure show the color of Dox–BNNTs suspension at increasing pH. As the pH is increased, the interaction between Dox and BNNTs becomes stronger, which means the increased Dox concentration remains in the suspension leading to a more intense red color (Figure 4.27a). However, there is almost no color change observed in the hBNs case (Figure 4.27b). The interactions with BNNTs are stronger at pH 7 with respect to hBNs. The increased loading of Dox could be explained with the adsorption of Dox onto BNNT surfaces, but encapsulation into the inner cavity of the nanotubes can be also taken into consideration, as suggested by other studies exploiting drug delivery inside the nanotubes [201].

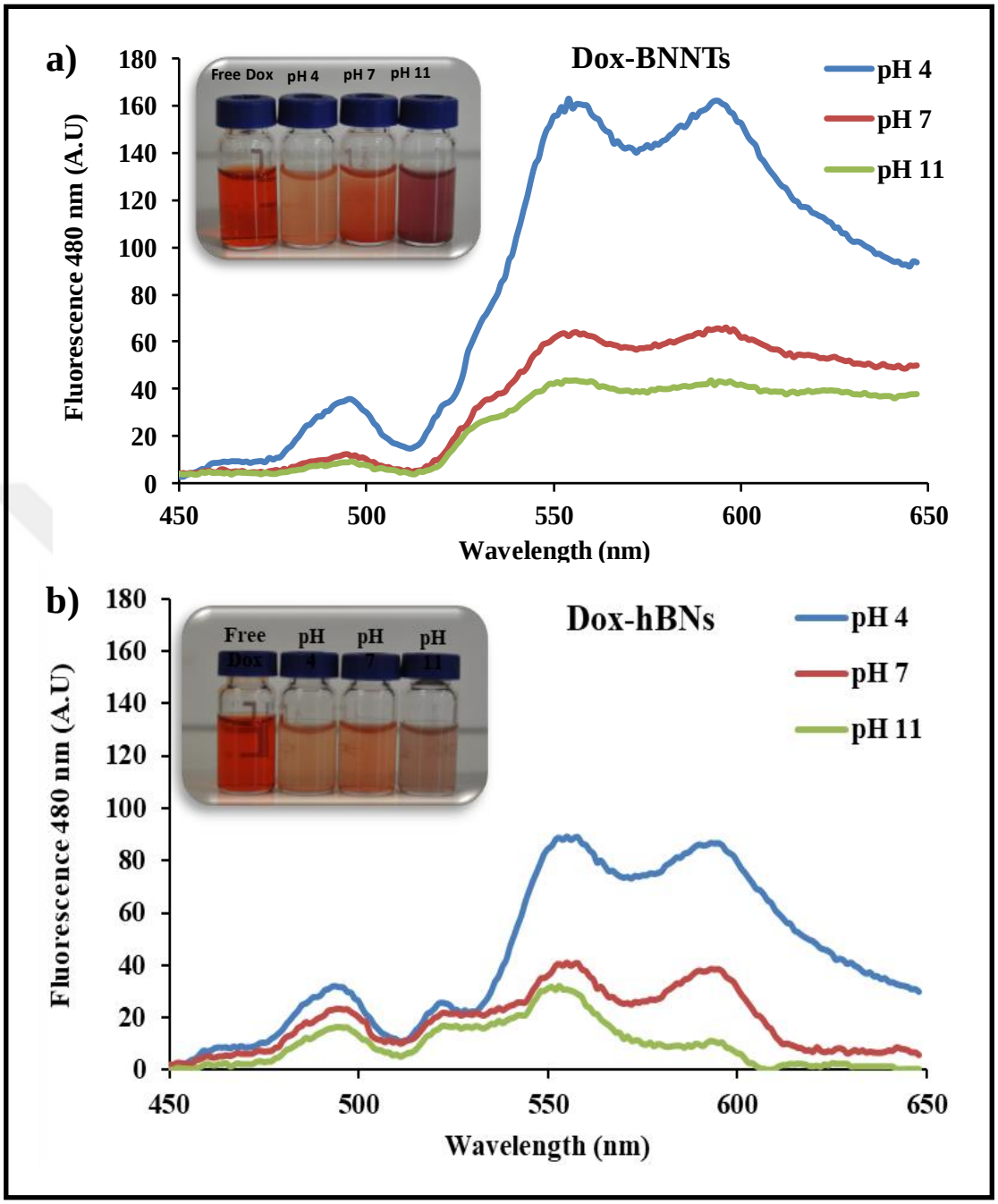

Figure 4.27. Fluorescent spectra of Dox-BNNTs and Dox-hBNs at different pH values.

The interactions between Dox and BNNTs or hBNs at different pH values were also characterized using UV/Vis spectroscopy. Dox has higher absorbance in its free form in solution compared with its conjugated form with BNNTs or hBNs through its aromatic rings [202]. This information can be used to understand the degree of interaction of Dox with BNNTs and hBNs. The data on Figure 4.28 show that the strongest interaction between

BNNTs and Dox is at pH 7 and pH 11 with respect to pH 4 (absorbed Dox is calculated as 10 wt per cent). The absorbance data from the Dox–hBNs complex are higher at pH 4 (3.75 wt per cent) with respect to the other pH values. Based on these results, Dox–BNNTs and Dox–hBNs are prepared at higher pH values (pH 7 or pH 11) for the following studies.

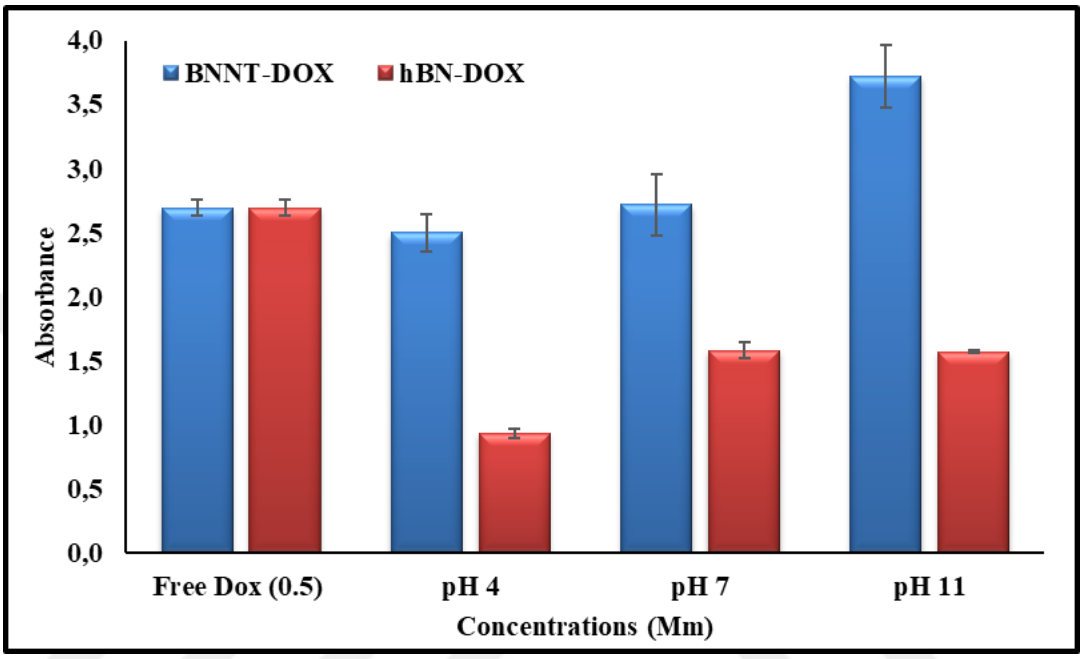

Figure 4.28. UV/Vis spectroscopy results of Dox-BNNTs and Dox-hBNs at different pH values.

4.3.2. Dox Release from BNNTs and hBNs

Dox–BNNTs and Dox–hBNs were prepared at pH 7 and 11 to describe Dox release behavior. The release studies were performed in PBS solution at increasing pH values of 4, 7 and 11 at increasing incubation times (1, 2, 4, 8, 24 and 72 h). As expected, the Dox release from BNNTs or hBNs showed different patterns. For instance, its release was almost stable at ph 7 and 11. While its release increased at lower pH values (at 4) due to weaker interactions, as shown in Figure 4.29. However, Dox release from hBNs was lower (Figure 4.29c and d), as compared with Dox released from BNNTs (Figure 4.29a and b). It is clear that the low release of Dox from hBNs is due to the low amount of Dox loaded onto hBNs. Therefore, the experiments were continued with Dox–BNNTs. The data suggest that the release of Dox

from the Dox–BNNTs can be triggered upon uptake by cells since lysosomes present an acidic environment, exploited to digest molecular species internalized through endocytosis [203, 204].

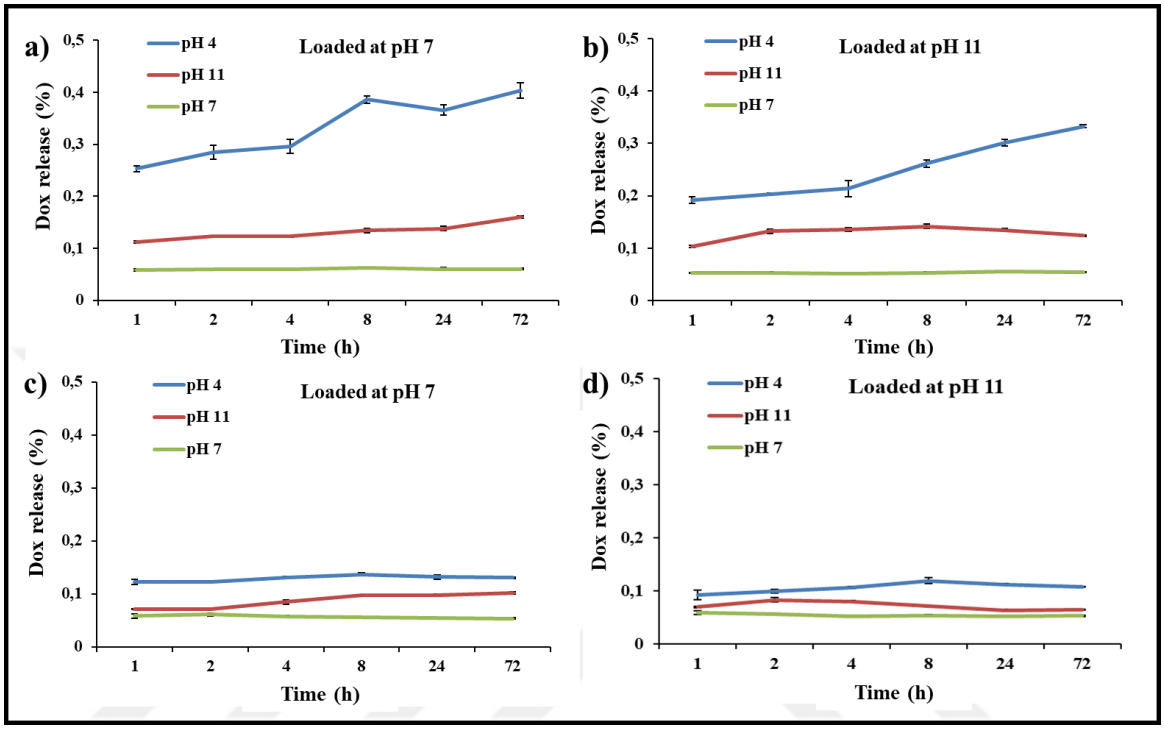

Figure 4.29. Dox release from Dox-BNNTs (a and b) and Dox-hBNs (c and d) at increasing pH values.

4.3.3. Folate Loading on Dox-BNNT Structures

The targeting studies of Dox–BNNTs to cancer cells were performed by decorating the structures with folate molecules. BNNTs were first complexed with Dox, and then with folate to decorate the surface of Dox–BNNTs in order to increase the possible binding with folate receptors on the surface of the cancer cells. The chemical structure of folate is shown in Figure 4.30. As seen, folate molecule has several ionizable groups and it can be negatively or positively charged depending on the pH of the medium. Two possible ways of binding to Dox–BNNTs for folate molecules can be envisaged. Since folate has phenyl moieties, it may bind to the surface of BNNTs (F–BNNTs) through π-π stacking if there are any uncoated areas left from Dox. In the second and most probable way, folate molecules graft onto Dox

molecules because of electrostatic interaction. The nature of interaction between Dox and folate should be mostly charge–charge in nature, since Dox tends to be positively charged and folate tends to be negatively charged depending. Since the majority of Dox molecules carries a positive charge at around neutral pH due to the presence of an amino group in their structure, it will be easier for folate molecules, which will be mostly negatively charged due to the presence of two carboxyl groups at around neutral pH, to adhere to the Dox–BNNTs conjugates.

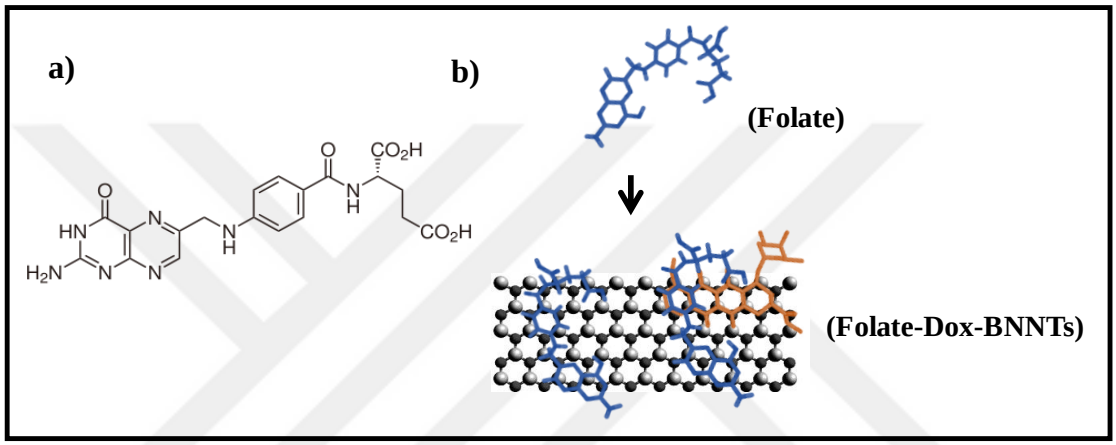

Figure 4.30. Schematic representation of folate interaction with Dox-BNNTs.

UV/Vis spectroscopy was used to investigate the conjugation of folate onto Dox–BNNTs. The comparison of free Dox and Dox–BNNTs in Figure 4.31a and folate and F–Dox–BNNTs in Figure 4.31b was analyzed. A strong absorption band at 230 nm, weak absorption at 250 nm and a wide peak at around 480 nm appear for free Dox. After the binding of Dox onto BNNTs, a decrease at the intensity of Dox absorption peaks is observed. This is possibly due to the lower concentration of Dox molecules adsorbed onto BNNTs. As mentioned earlier, the loading efficiency of Dox onto the BNNTs was about 10 wt per cent. Free folate molecules show a strong absorption peak at 275 nm and a less intense peak at 360 nm. On the absorption spectrum of F–Dox–BNNT the characteristic peaks (at around 230, 250, 275 and 480 nm) originating from both Dox and folate are observed. However, the folate binding onto the Dox–BNNTs was decreased to 19 per cent. The UV/Vis spectroscopy results show almost the same absorbance intensity at around 480 nm (specific for Dox molecule) for the F–Dox–BNNT samples. Thus, no appreciable Dox release was detected even after the folate conjugation.

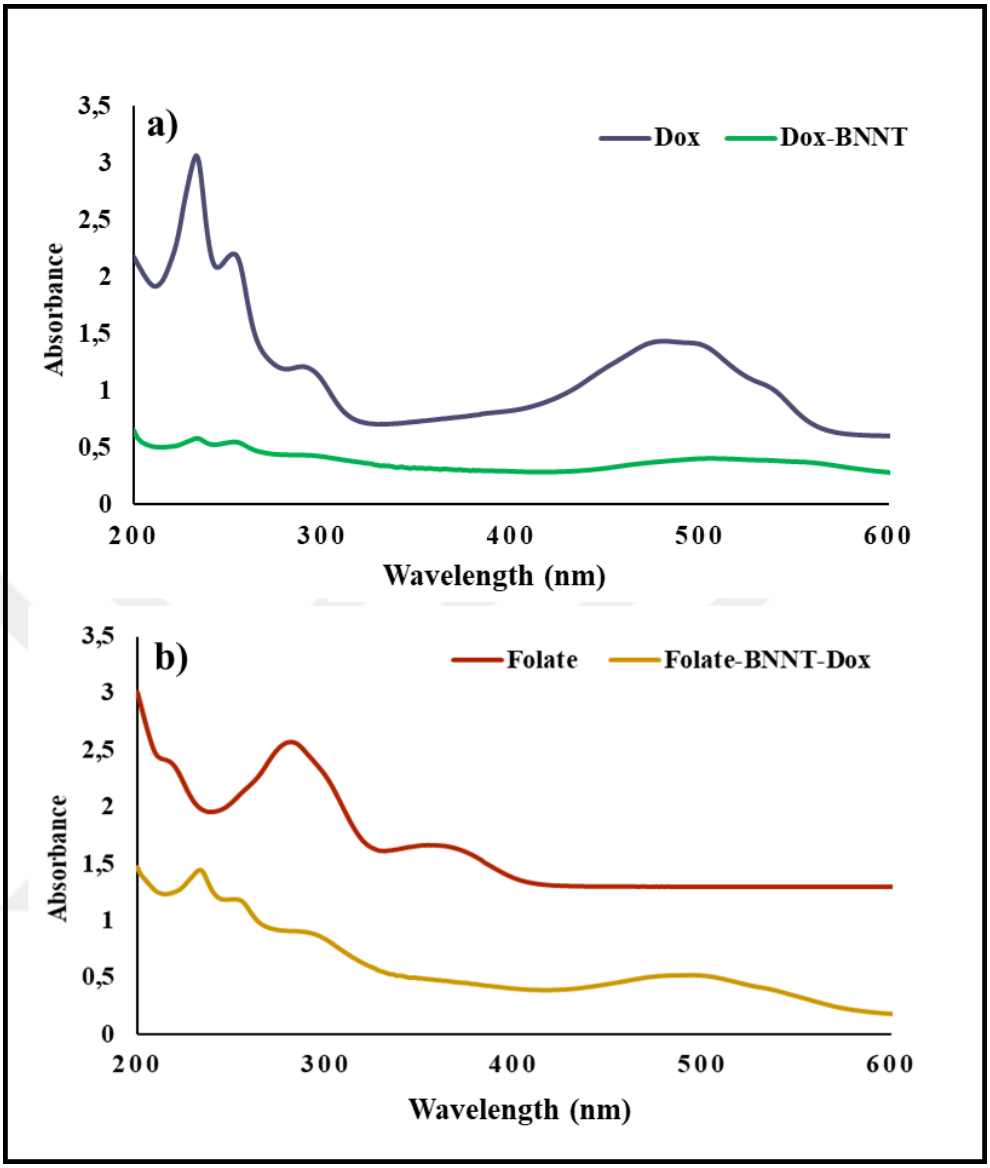

Figure 4.31. UV/Vis spectroscopy analysis of Dox, Folate, Dox-BNNTs and F-Dox-BNNTs.

The binding of folate and Dox molecules to BNNTs was also confirmed by measuring their zeta potentials as shown in Table 4.3. Owing to the negatively charged folate and positively charged Dox molecules, their electrostatic interaction occurred because of their opposite charges as mentioned above. As seen in the table, after the attachment of the positively charged Dox onto the negatively charged BNNTs (-9.94 mV), their charge becomes less negative (-5.98 mV). Their charge becomes also more negative (-12.70 mV) when Dox–BNNTs interacted with folate. The charge was not as negative as F–BNNTs (-14.50 mV)

due to the positive charge of Dox. As seen, zeta potential measurements support the absorption spectroscopy data.

Table 4.2. Zeta potential of BNNTs, Dox-BNNTs and F-Dox-BNNTs.

	Folate-Dox	**Folate**	**Dox**	**free**
BNNT	-12.7±1.2mV	-14.5±0.7mV	-5.97±0.1mV	-9.94±1.8mV
free		-32.3±4.3mV	3.69±0.5mV	

4.3.4. Cellular Uptake of Folate-Dox-BNNT Structures

In this study, HeLa cells were chosen as model cancer cells due to the overexpression of folate receptors on their cell surface. Since folate receptors are not overexpressed in HUVECs, it was chosen to observe folate-mediated cellular uptake of F–Dox–BNNTs. Moreover, HUVECs were treated with F–Dox–BNNTs to estimate their behavior envisioning future *in vivo* studies through intravenous administration. Confocal microscopy images were obtained to observe the internalization of the free Dox, Dox–BNNTs and F–Dox–BNNTs by the cells after 4 h of incubation. The fluorescence originating from Dox allowed the tracking of the uptake of the Dox–BNNTs and F–Dox– BNNTs in the HeLa cells (Figure 4.32) and in HUVECs (Figure 4.33). The confocal images show HeLa cells and HUVECs incubated with a 20 μg/mL concentration of Dox–BNNTs. Since it was found that Dox loading efficiency onto BNNTs is 10 wt per cent and the initial concentration of Dox used for loading is 5.0 mM, 1/10 of this concentration (0.5 mM) as free Dox is applied to control cells to compare the fluorescence intensity in the images. Figure 4.32 show the results of the confocal microscopy imaging study with HeLa cells. The fluorescence intensity from HeLa cells was weak when the free Dox and Dox–BNNTs were added into the cell cultures, as depicted by Figure 4.32a and b, respectively. However, the fluorescence intensity was significantly increased when folate conjugation was performed, indicating a remarkably increased cellular uptake of the F–Dox–BNNTs (Figure 4.32c). In order to understand whether the cellular uptake is folate-mediated in HeLa cells, a competitive inhibition experiment was performed. 3.5 mM free folate was added into the medium to

saturate the folate receptors before the addition of the conjugate complex, and then the F–Dox–BNNTs were incubated with the cells. As shown in Figure 4.32d, a weak fluorescence was observed indicating that the uptake was folate-mediated for F–Dox–BNNTs.

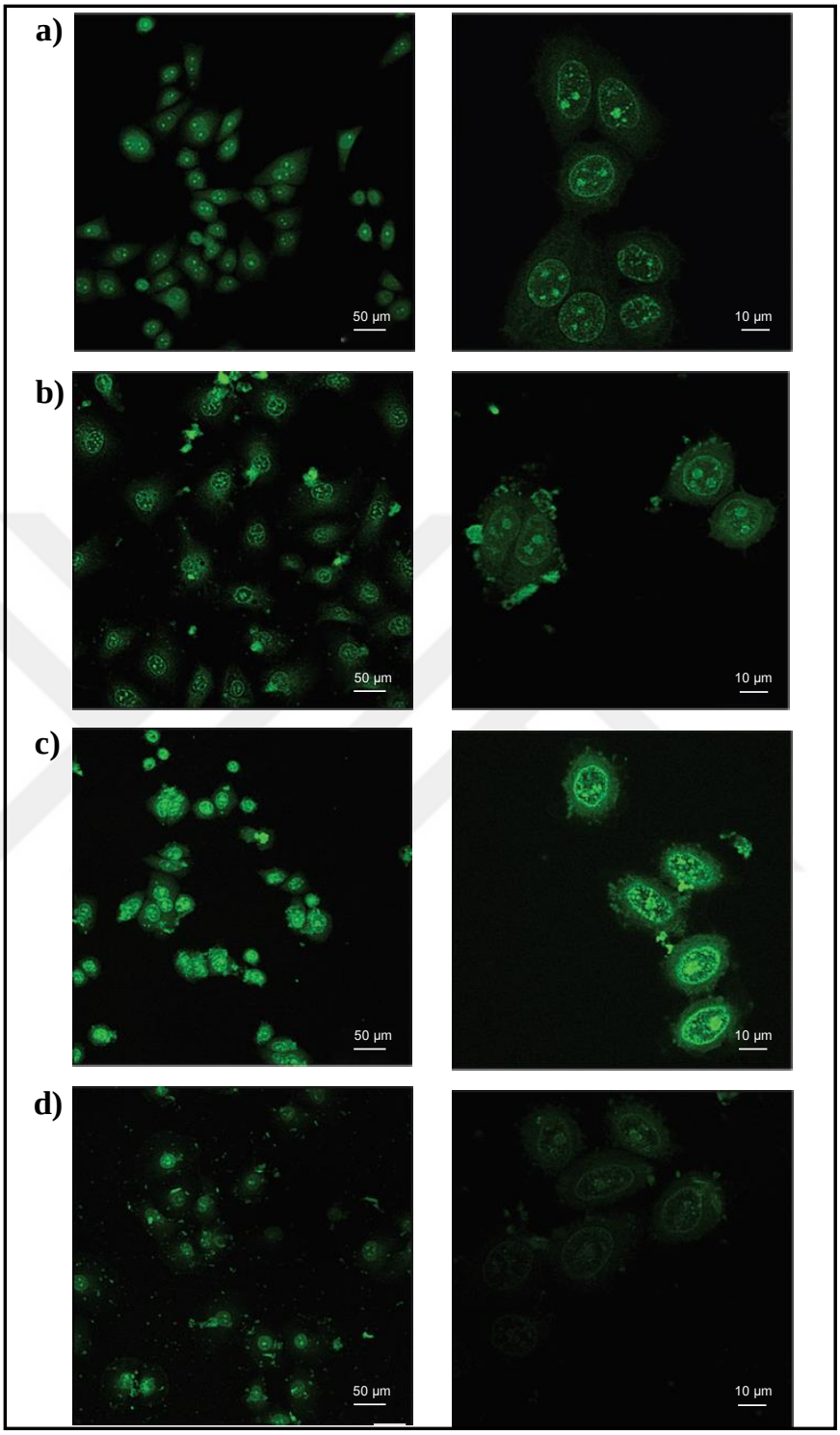

Figure 4.32. Confocal microscopy images of HeLa cells incubated with free Dox (a), Dox–BNNTs (b), F–Dox–BNNTs (c) and F–Dox–BNNTs after pre-incubation with a 3.5 mM folate solution (d).

Figure 4.32 show the confocal images of HUVECs incubated with 0.5 mM of Dox, 20 μg/mL of Dox–BNNTs and F–Dox–BNNTs, respectively. As proven by the results of fluorescence intensity analysis in Figure 4.34, the fluorescence intensity pattern for HUVECs resembles the case of HeLa cells (Figure 4.33a, b and d), exception done for Figure 4.33c. Since folate receptors are not overexpressed in HUVECs [205], the cellular uptake of F–Dox–BNNTs is similar to Dox–BNNTs. The fluorescence intensity was thus weaker for F–Dox–BNNTs in HUVECs as compared with the HeLa cells. Furthermore, folate saturation of the receptors did not significantly affect the cellular uptake of F–Dox–BNNTs (Figure 4.33d) as compared with the unsaturated cells, due to the absence of overexpressed folate receptors in HUVECs. Moreover, the high-magnification images of HeLa cells and HUVECs show that Dox accumulates in the nuclei regardless of whether it is free or conjugated to BNNTs. The fluorescent observed in the cytosol are most probable Dox–BNNTs and just-released Dox molecules. These observations strongly suggest that the Dox is released from the conjugate heading to the nuclei from the cytosol. The data suggest that folate conjugation was significant for Dox targeting into the folate receptor overexpressing cancer cells.

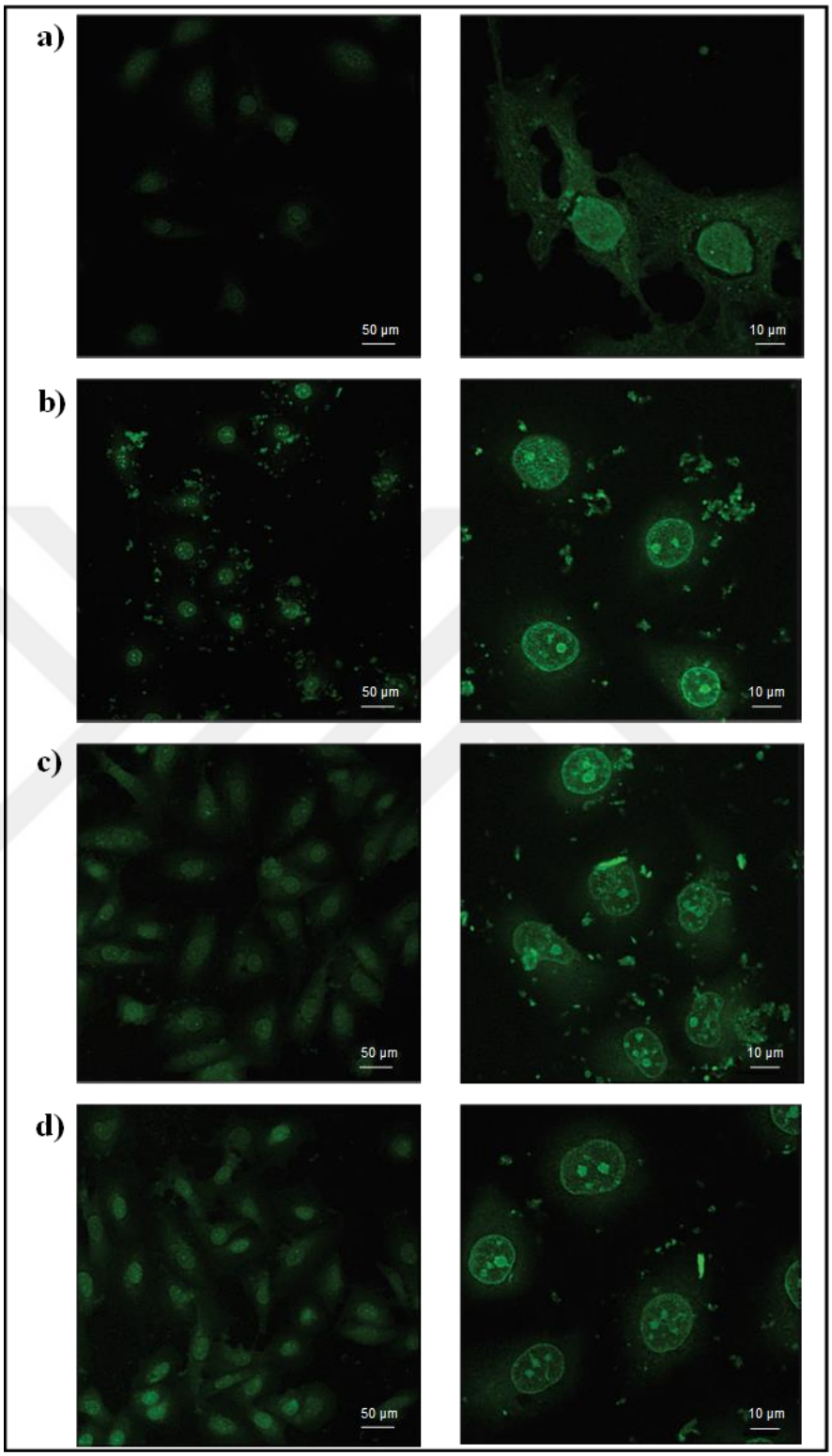

Figure 4.33. Confocal microscopy images of HUVECs incubated with Free Dox (a), Dox–BNNTs (b), F–Dox–BNNTs (c) and F–Dox–BNNTs after pre-incubation with a 3.5 mM folate solution (d).

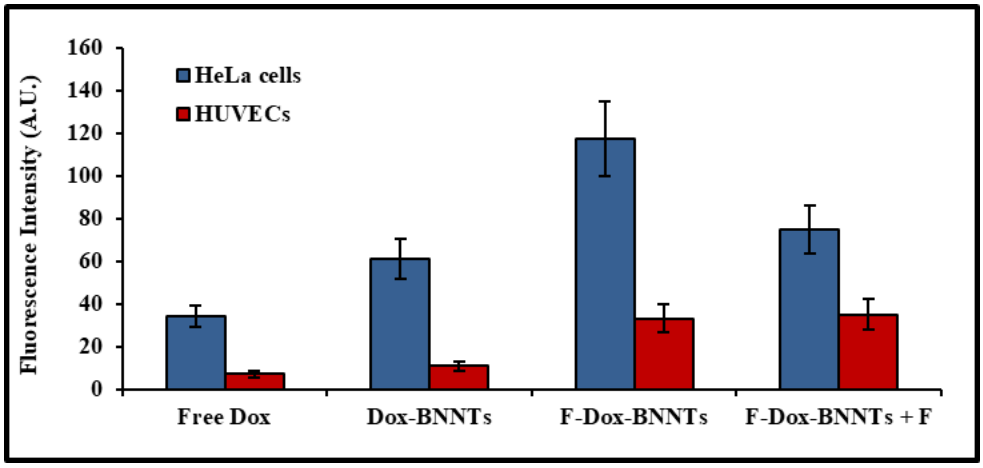

Figure 4.34. Quantitative analyses of confocal images of HeLa cells and HUVECs.

4.3.5. Cell Viability Studies

Cellular toxicity of F–Dox–BNNTs was investigated. The cells were incubated with only BNNTs, free Dox, Dox–BNNTs and F–Dox–BNNTs with increasing concentrations (5-100 μg/mL) for increasing incubation times (1, 2, 4, 8, 24 and 72 h). Figure 4.35 and 4.36 show the viability of HeLa cells and HUVECs, respectively. Figure 4.35a and 4.36a demonstrate that only BNNTs do not show toxicity to both cell types and only a slight toxicity is observed with increased incubation times. The viability for both cell lines was between 85 and 110 per cent. The free Dox-exposed cells showed significant decrease in viability at 8, 24 and 72 h incubation times, as seen in Figure 4.35b and 4.36b. The Dox–BNNT conjugates show the same effect as free Dox, by significantly decreasing the cell viability in the range of 20 - 60 per cent at 8, 24 and 72 h incubation times (Figure 4.35c and 4.36c). The F–Dox–BNNTs show significant toxic effect even at earlier incubation times (4, 8, 24 and 72 h) on HeLa cells, and the viability is in the range of 5 - 40 per cent; moreover, they were significantly toxic at 8, 24 and 72 h incubation times on HUVECs (in the range of 20 and 60 per cent) (Figure 4.35d and 4.36d). The viability decrease of HeLa cells at earlier incubation times with respect to HUVECs is attributed to a quicker accumulation of F–Dox–BNNTs into HeLa cells due to selective targeting. These results demonstrate that the F–Dox–BNNT conjugates can be promising structures for cancer therapy.

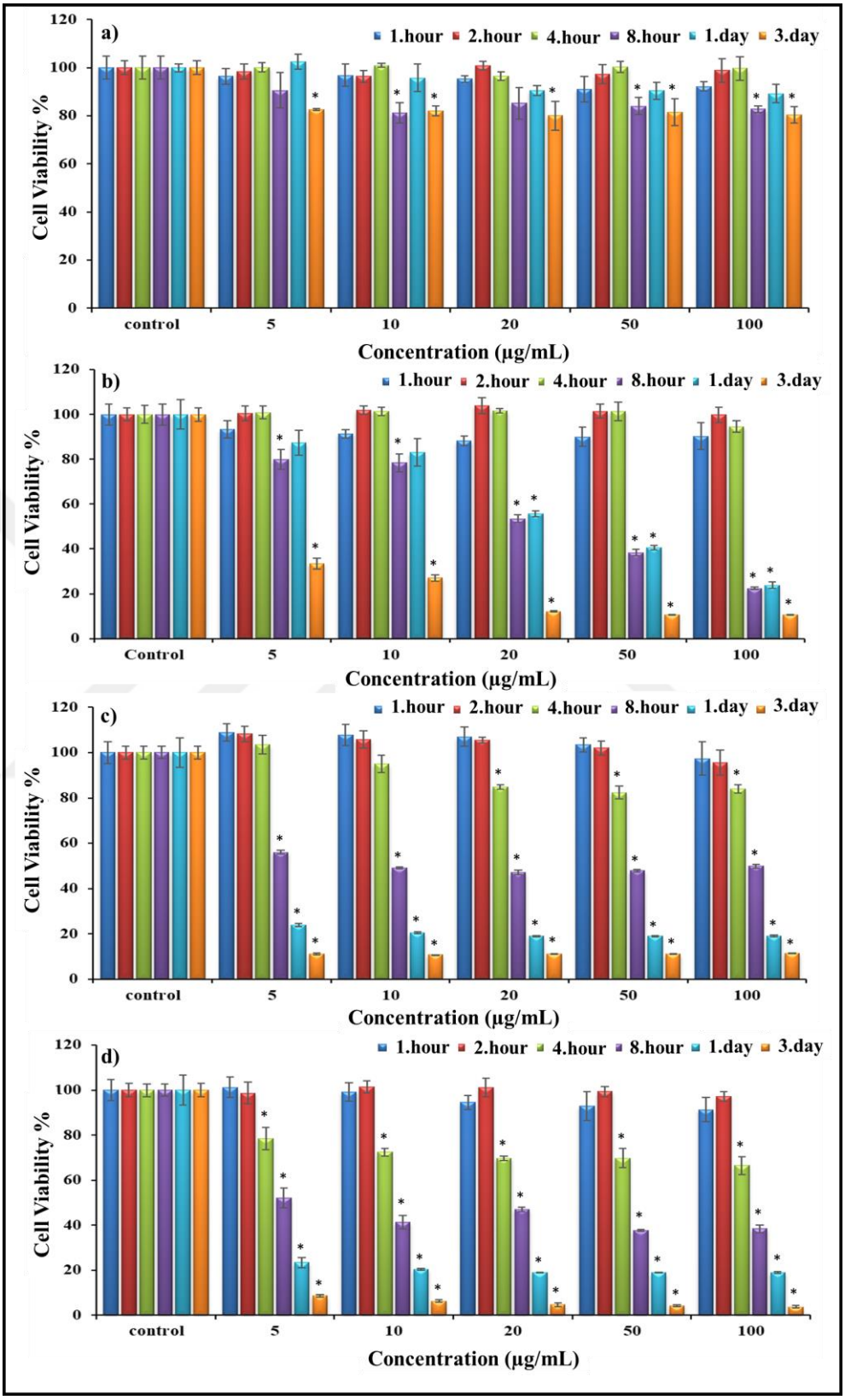

Figure 4.35. Cell viability assessment of HeLa cells incubated with BNNTs (a), free Dox (b), Dox–BNNTs (c) and F–Dox–BNNTs (d). (*$p < 0.05$)

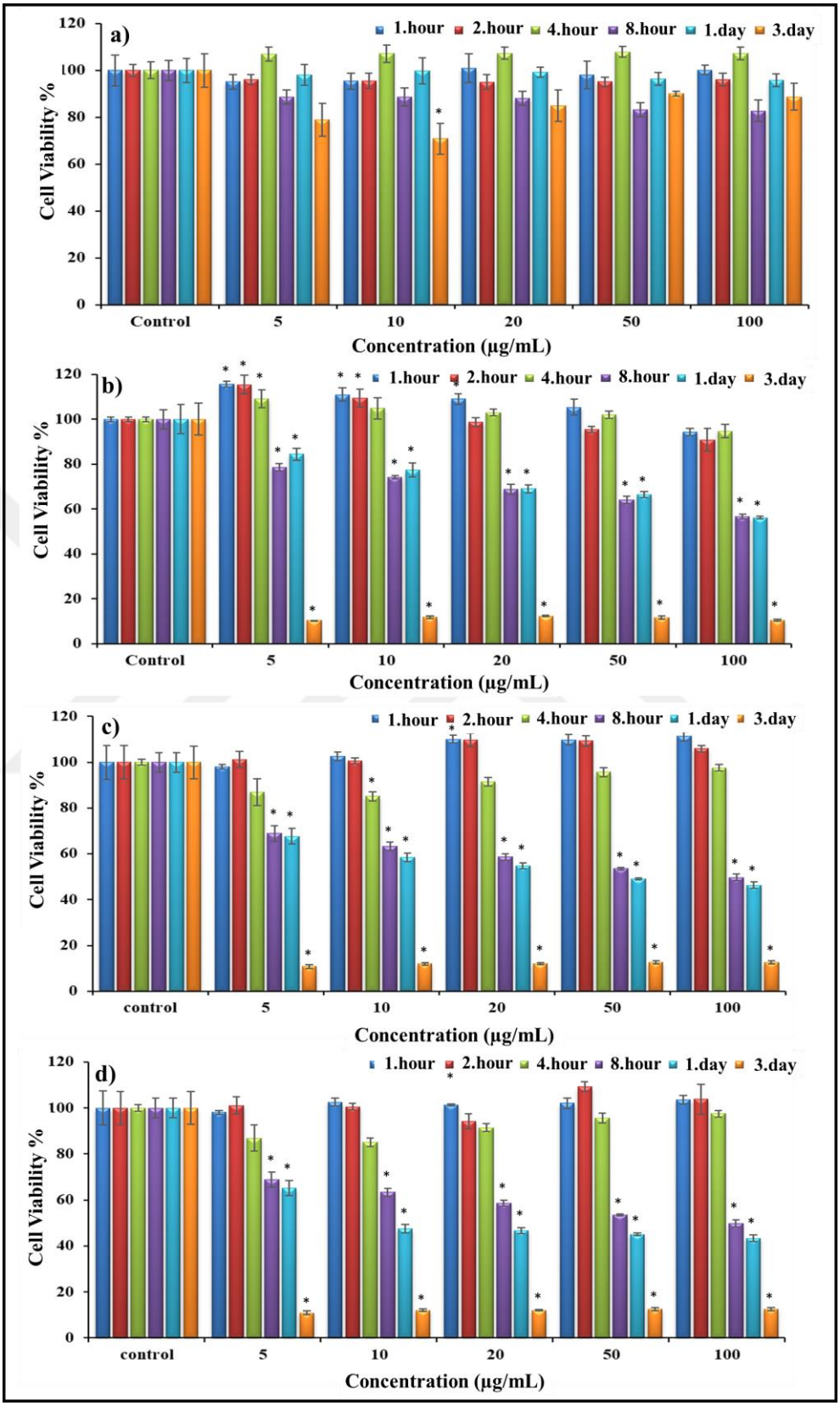

Figure 4.36. Cell viability assessment of HUVECs incubated with BNNTs (a), free Dox (b), Dox–BNNTs (c) and F–Dox–BNNTs (d). (* $p < 0.05$)

Although it is assumed that drug molecules adhere to the surface of BNNTs, the increased loading efficiency of BNNTs suggests that it is possible that neutral Dox molecules can enter into the nanotubes. The average diameter of BNNTs is estimated as 40 nm as stated earlier. When the size of the Dox molecules is considered, which is theoretically estimated as 3 nm, trapping of Dox molecules inside the hollow nanotubes is possible. Increased loading efficiency of Dox at neutral and higher pH values is a further hint that supports this hypothesis.

4.4. TRANSFERRIN-MEDIATED GLIOBLASTOMA CELL TARGETING OF hBNs

This part of study aims at addressing drug delivery issues and therapeutic challenges by proposing a BN-based drug and boron delivery system. In the rest of study, with an easy and catalyst free synthesize method, hBNs were synthesized and used both a nanocarrier and boron source. As shown in Figure 4.37, hBNs were functionalized with the DSPE-PEG-NH_2 phospholipid through hydrophobic interaction between hBNs and the phospholipid tails of the DSPE-PEG-NH_2. The DSPE-PEG-NH_2 functionalization of the hBNs increased their dispersibility in water and provided -NH_2 active ends for binding BBB targeting agent such as transferrin and insulin molecules. Besides, the PEG molecules in the structure increases their blood circulation duration, thus enhancing their BBB transfer possibility. Further, the DSPE-PEG-hBNs structure were dispersed in small sizes (< 100 nm) to increase their cellular penetration capacity through the BBB. Thereafter, DSPE-PEG-hBNs were functionalized with specific ligands that recognize BBB receptors such as transferrin (TfR-DSPE-PEG-hBNs) thanks to the active -NH_2 ends in the DSPE-PEG-NH_2 structure wrapping the hBNs.

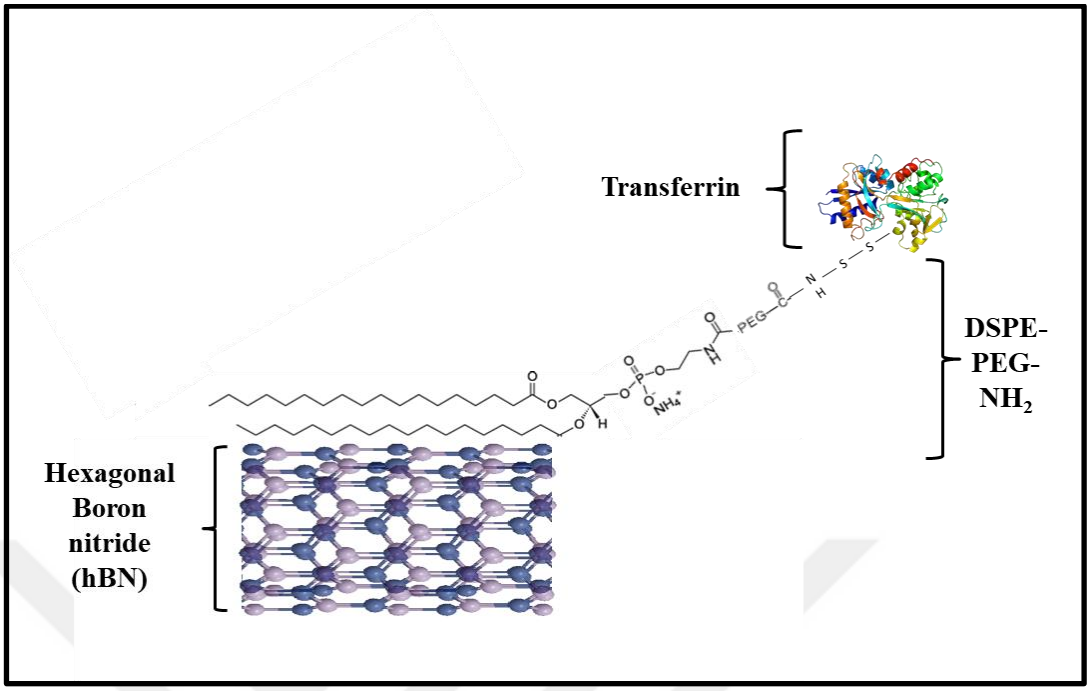

Figure 4.37. Schematic illustration of TfR-DSPE-PEG-hBNs.

4.4.1. Characterization of DSPE-PEG-hBNs

The hBNs were complexed with DSPE-PEG-NH_2 molecules, that have two hydrophobic fatty acid chains and a hydrophilic PEG structure that includes also -NH_2 end for further covalent functionalization. The interaction occurred between the side walls of the hBNs and the hydrophobic fatty acid chains of the DSPE-PEG-NH_2 molecules. The bare hBNs and DSPE-PEG-hBNs were comparatively characterized using UV/Vis spectroscopy as shown in Figure 4.38. The UV/Vis spectra of DSPE-PEG-hBNs shows characteristic absorption peak of the hBNs, originated from B-N bonds, around 210 nm wavelength, while the DSPE-PEG-NH_2 specific absorption peaks were observed around 200 and 280 nm.

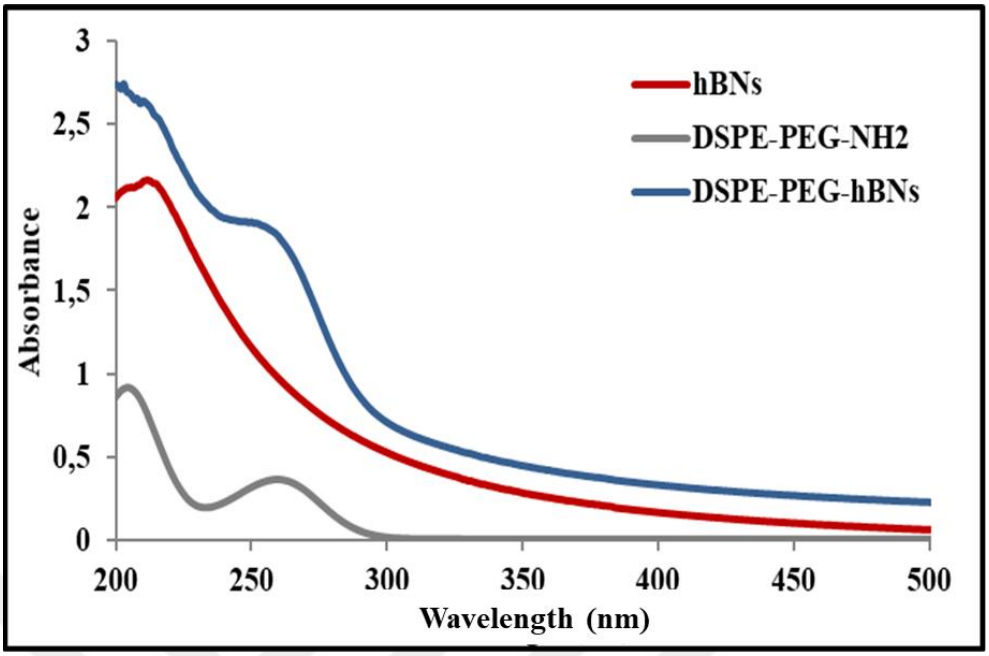

Figure 4.38. UV/Vis spectroscopy of hBNs, DSPE-PEG-NH_2, and DSPE-PEG-hBNs.

The DSPE-PEG-NH_2 interaction yield with hBNs was moreover quantified using TGA analysis as shown in Figure 4.39. Due to the high thermal stability of the hBNs, the 12 per cent weight loss of the DSPE-PEG-hBNs around 240-400^{o}C shows the interaction yield of DSPE-PEG-NH_2 molecules. Therefore, it can be said that the 12 per cent of DSPE-PEG-hBNs weight belongs to DSPE-PEG-NH_2.

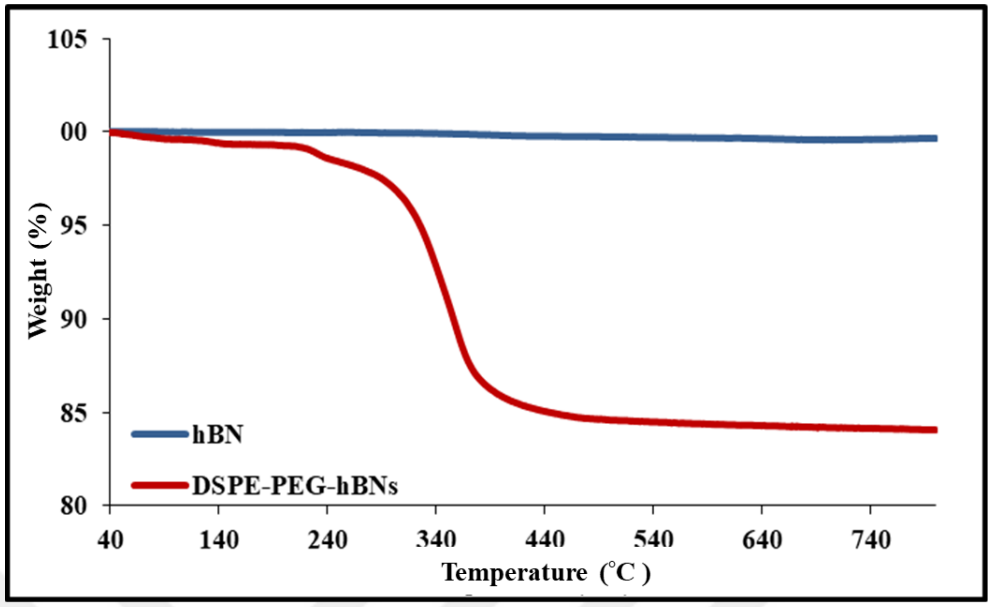

Figure 4.39. TGA analysis of hBNs and DSPE-PEG-hBNs.

4.4.2. Colloidal Stability of DSPE-PEG-hBNs

The hydrophobic nature of the hBNs limits their use in biological applications because of the poor colloidal stability in aqueous media. Therefore, one of the aims of DSPE-PEG-NH_2 functionalization was providing hydrophilic surface around the hBNs, thus increasing their colloidal stability. The colloidal stability of hBNs and DSPE-PEG-hBNs was comparatively investigated with DLS by measuring their particle size distribution at different time points (0, 1 and 24 h) following dispersion (Figure 4.40). The size distribution of DSPE-PEG-hBNs was found to be between 120 and 230 nm and their average size was approximately 164 nm, while the hBNs size distribution was between 120 and 290 and their average size was approximately 190 nm just after the interaction (Figure 4.40a). After 1 h of interaction, the size distribution of the DSPE-PEG-hBNs was found to be between 100 and 290 nm and their average size approximately was 190 nm, while hBNs size distribution was between 60 and 540 and average size approximately 255 nm, as shown in Figure 4.40b. After 24 of interaction, the size distribution of the DSPE-PEG-hBNs was found to be between 100 and 390 nm and their average size was approximately 220 nm, while hBNs size distribution was between 60 and 660 and average size was approximately 260 nm as shown in Figure 4.40c. It has been observed that the size distribution of DSPE-PEG-hBNs is narrower at each time

points of measurement as compared to that one of the plain hBNs, indicating a higher colloidal stability of DSPE-PEG-hBNs in aqueous environment with respect to the bare form of hBNs. Moreover, the lower average size of the DSPE-PEG-hBNs with respect to hBNs further confirms their higher dispersion capacity.

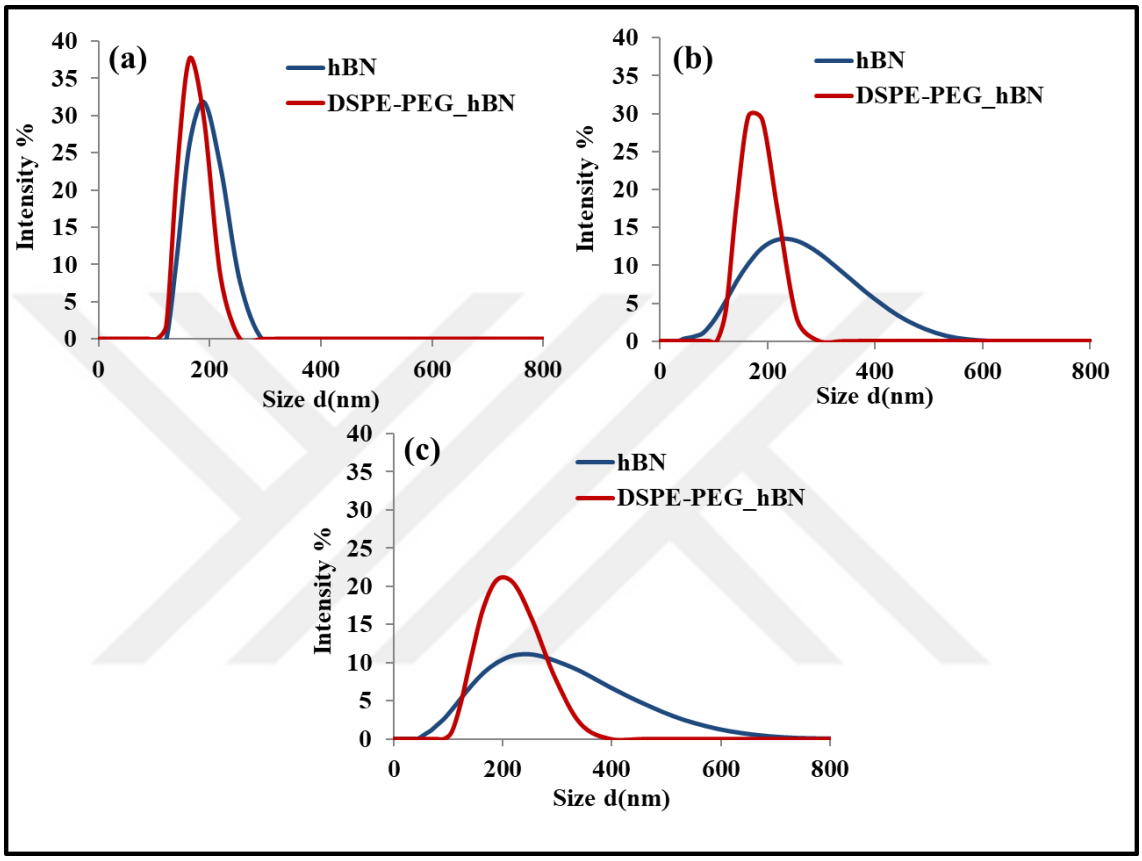

Figure 4.40. Size distribution of hBNs and DSPE-PEG-hBNs at 0 (a), 1 (b) and 24 h (c) after the dispersion.

4.4.3. Characterization of TfR-DSPE-PEG-hBNs

Transferrin-functionalized DSPE-PEG-hBNs were spectroscopically characterized using FT-IR as shown in Figure 4.41. The FT-IR spectra of the hBNs shows the broad B-N characteristic peaks around 1340 and 630 cm^{-1}, which were suppressed by the DSPE-PEG-NH_2 and by the transferrin molecules following the functionalization process. The transferrin-originated broad peaks in the range of 3000–3600 cm^{-1} is attributed to the -NH_2

and -OH groups that were revealed in the TfR-DSPE-PEG-hBNs structures. The small peaks in the TfR-DSPE-PEG-hBNs structures around 2926, 2853, 1250 and 1465 cm^{-1} are attributed to the C-H bonds originated from transferrin and DSPE-PEG-NH_2. Moreover, transferrin conjugation indicated peaks around 1650-1550 cm^{-1}, that are attributed to the C=C and C=N bonds in TfR-DSPE-PEG-hBNs structures. The results confirm that the transferrin functionalization of the DSPE-PEG-hBNs was performed successfully. Moreover, the binding efficiency was investigated using BCA protein quantification tests, and results indicated 1 per cent binding efficiency of transferrin.

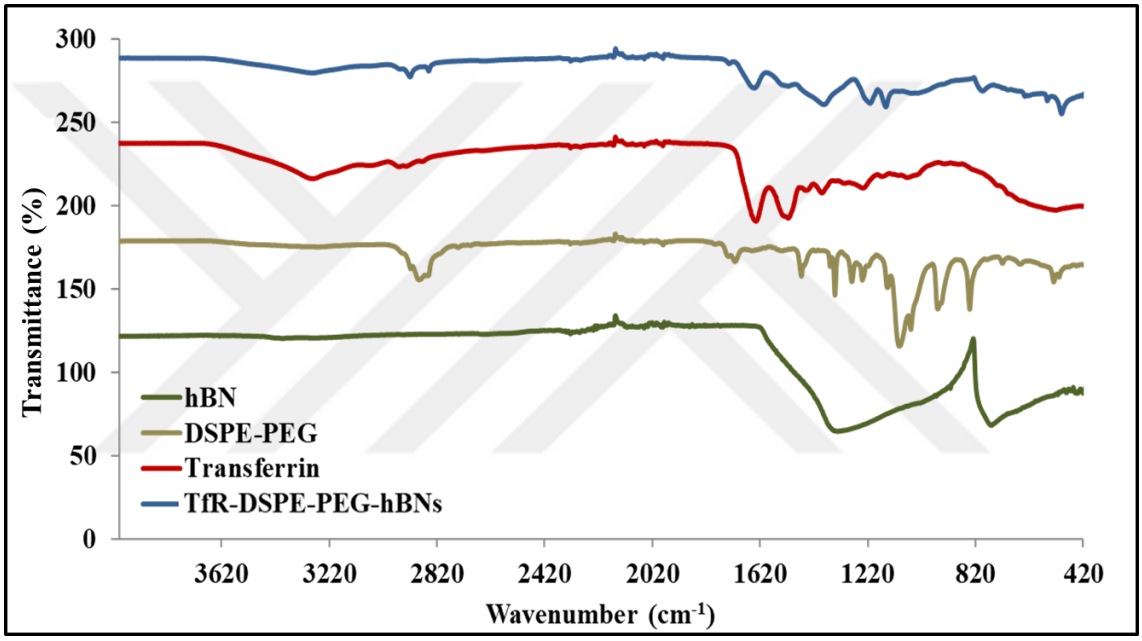

Figure 4.41. FT-IR spectra of hBNs, DSPE-PEG-NH_2, transferrin and TfR-DSPE-PEG-hBNs.

4.4.4. Biocompatibility and Cellular Uptake of TfR-DSPE-PEG-hBNs

In this study, glioblastoma multiforme cells (U87MG) were chosen as a model brain cancer cells with overexpressed transferrin receptors on the cell surface [206]. The cells were exposed to hBNs, DSPE-PEG-NH_2, DSPE-PEG-hBNs, transferrin, and TfR-DSPE-PEG-hBNs. Their biocompatibility was investigated using WST-1 colorimetric assay as shown in Figure 4.42. According to these results, while the viability of the hBN-exposed cells increased to the 105 per cent, the DSPE-PEG-NH_2 and DSPE-PEG-hBNs exposed cell

viability decreased to 87 per cent and 84 per cent at the highest tested concentration (100 µg/mL). However, the TfR-DSPE-PEG-hBNs exposed cell viability was significantly decreased to the 49 per cent at the highest tested concentration (100 µg/mL), most probably because of the toxic nature of the transferrin at high concentrations [206].

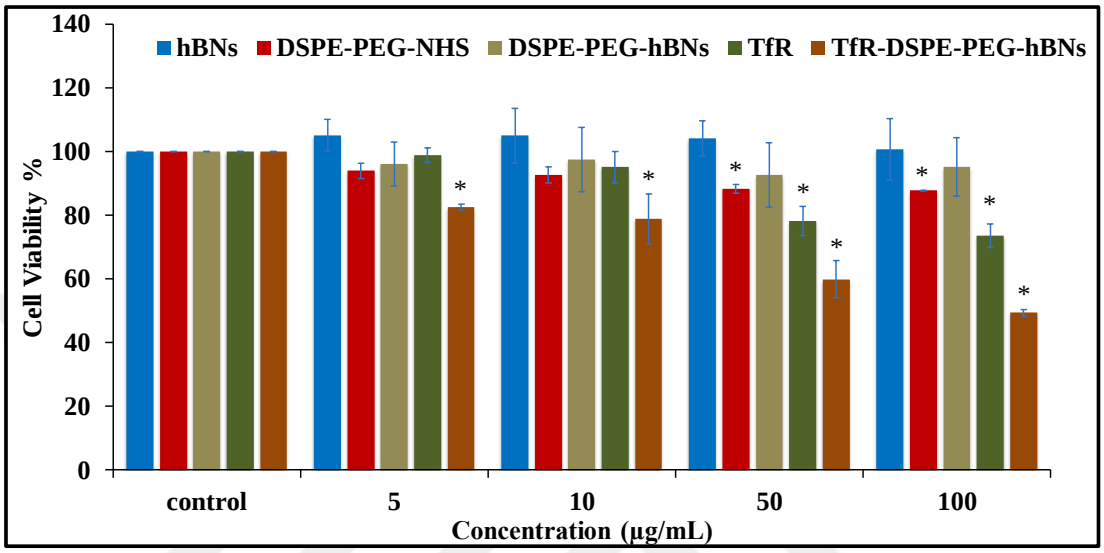

Figure 4.42. Cell viability assay of hBNs, DSPE-PEG-NH_2, DSPE-PEG-hBNs, transferrin, and TfR-DSPE-PEG-hBNs exposed glioblastoma cells. (analyzed with student *t*-test $^{*}p < 0.05$)

The cellular uptake of hBNs, DSPE-PEG-hBNs, and TfR/DSPE-PEG/hBNs was comparatively analyzed by measuring the side scattering of the cells using flow cytometer as shown in Figure 4.43. The internalization of structures was analyzed by considering the cellular uptake of TfR-DSPE-PEG-hBNs at the 24 h of incubation as a reference. Therefore, TfR-DSPE-PEG-hBNs uptake is considered to be 100 per cent at 24 h of incubation. Relatively, the hBN uptake of the cells regularly increases up to 80 per cent, while the DSPE-PEG-hBNs up to 71 per cent after 24 h of incubation. Moreover, the uptake of the hBNs and DSPE-PEG-hBNs continued to increase up to 96 per cent and 91 per cent while the uptake of the TfR-DSPE-PEG-hBNs decreased to 91 per cent after 48h of incubation. The results also explain the significantly increased cellular uptake of TfR-DSPE-PEG-hBNs up to 24 h of incubation indicates increased uptake of the structures due to transferrin functionalization, and this provides important clues about the stimulation of active transport system of the cells have overexpressed transferrin receptors on their surface. Additionally, the toxic nature of

high doses of transferrin decreases the cell viability. Thus, it is estimated that the cellular uptake of the TfR-DSPE-PEG-hBNs decreased after 48 h of incubation.

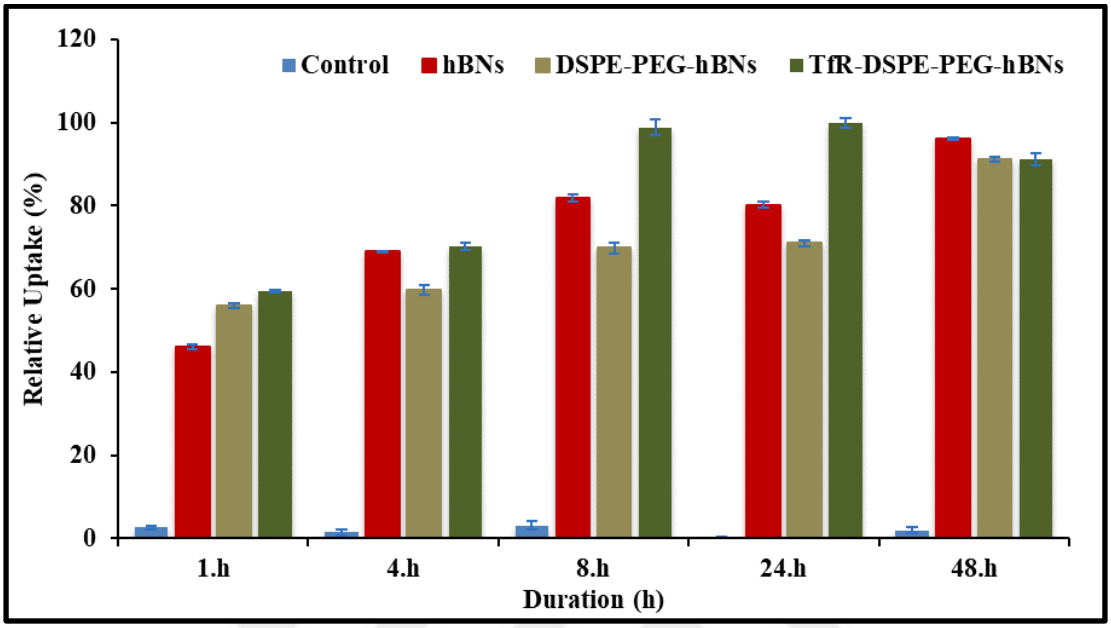

Figure 4.43. Cellular uptake of hBNs, DSPE-PEG-hBNs and TfR-DSPE-PEG-hBNs.

Confocal microscopy images were acquired to observe the internalization of free FITC, TfR-FITC-DSPE-PEG-hBNs (10 µg/mL), and TfR-FITC-DSPE-PEG-hBNs (100 µg/mL) by the cells after 4 h of incubation. The fluorescence originating from FITC allowed tracking uptake of the TfR-FITC-DSPE-PEG-hBNs by glioblastoma cells, as shown in Figure 4.44. As seen in the figure, the free FITC and TfR-FITC-DSPE-PEG-hBNs structures were successfully internalized into the cells and distributed in the cytosol. It is also seen that the both concentration of TfR-FITC-DSPE-PEG-hBNs exposed cells have apoptotic bodies in the nucleus, while the 100 µg/mL of TfR-FITC-DSPE-PEG-hBNs exposed cells lost their cellular integrity. All the cellular experiments clearly indicate the TfR-DSPE-PEG-hBNs have a superior cellular uptake capacity, that is the reason of the strong cell viability decrease of glioblastoma cancer cells.

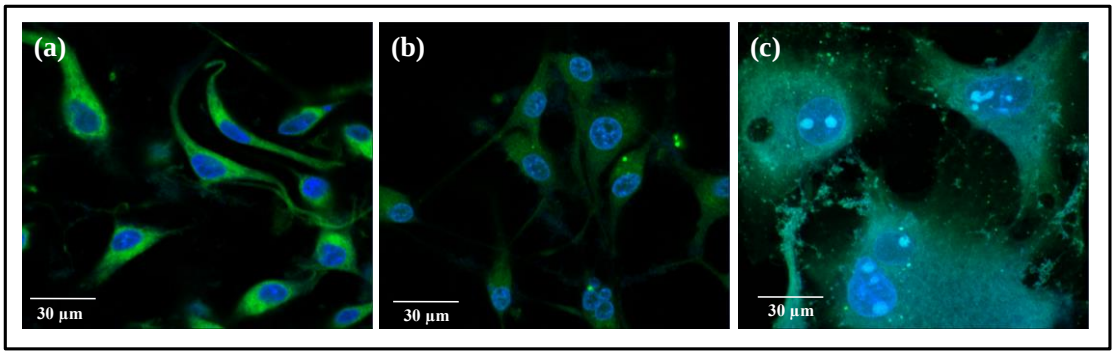

Figure 4.44. Confocal images of glioblastoma cells exposed to FITC (a), TfR-FITC-DSPE-PEG-hBNs (10 µg/mL) (b) and TfR-FITC-DSPE-PEG-hBNs (100 µg/mL) (c).

4.5. hBNs AS A PROSTATE CANCER INHIBITION AGENT

4.5.1. Determination of the Concentration and Cellular Sensitivity for hBNs

The dose dependent anti-proliferative and -metastatic effects of hBNs investigated on androgen independent (DU145 and PC3) prostate cancer cells, and it was comparatively investigated with healthy cells (PNT1A) as shown in Figure 4.45, 4.46 and 4.47, respectively. The cell viability was measured using WST1 colorimetric assay to reveal dose dependent hBN effects. The results indicated the importance of long-term effects of the structures on cells. Despite the viability of hBN-exposed DU145 cells increased around 101 per cent the first day of incubation, their viability dramatically decreased around 10 per cent at the third day of incubation as shown in Figure 4.45a, while the viability of BA-exposed DU145 cells increased around 118 per cent and decreased around 19 per cent at the third day of incubation (Figure 4.45b). The result indicates that the hBN and BA sensitivity of DU145 cells are similar at the third day of incubation at high concentrations (500 and 1000 µg/mL).

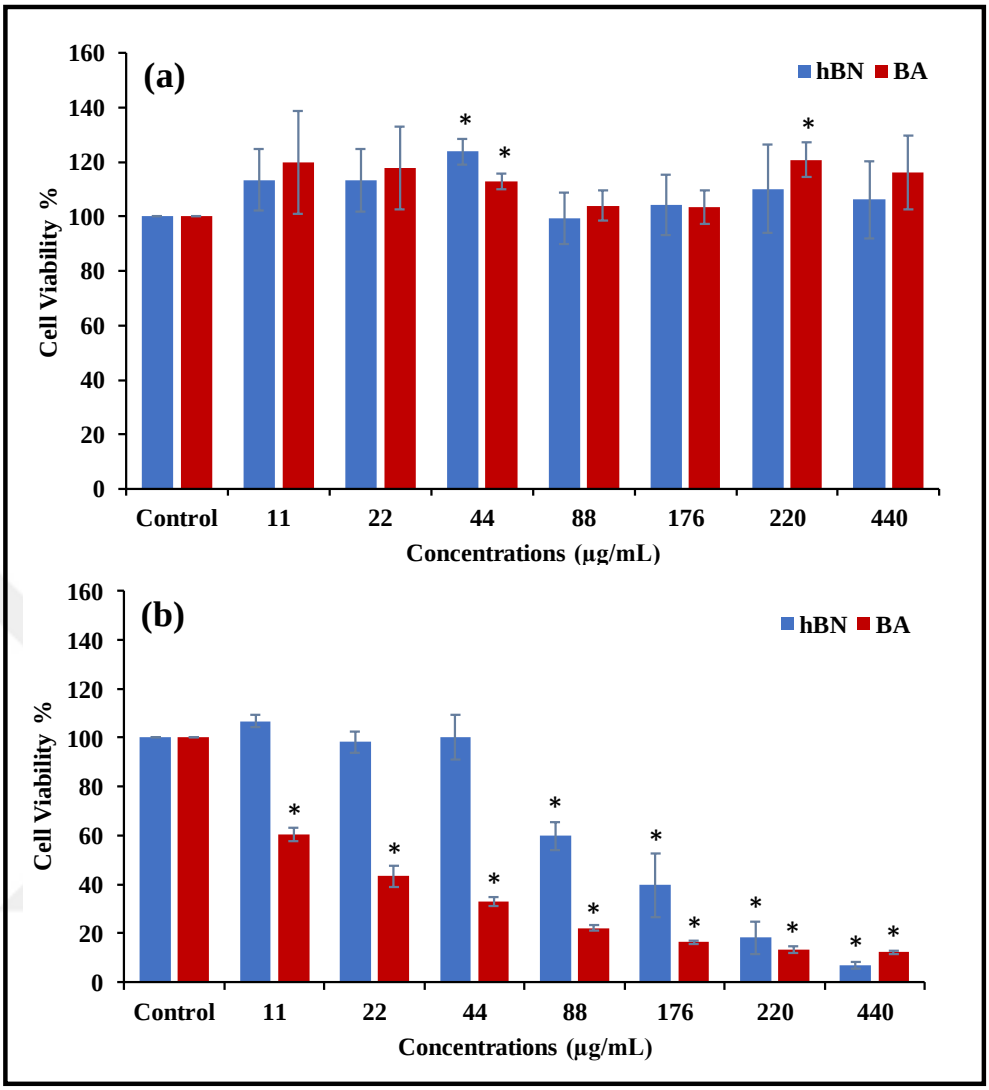

Figure 4.45. Viability of DU145 cells exposed to hBN and BA at the first (a) and third (b) days of incubation. (analyzed with student *t*-test $^{*}p < 0.05$)

The viability of hBN exposed PC3 cells was around 80 per cent at the first and third days of incubation (Figure 4.46a), but BA-exposed PC3 cell viability was 42 per cent at the first day and 18 per cent at third day of incubation as shown in Figure 4.46b. The result indicated that the PC3 cells show higher sensitivity against BA, especially at the increased incubation times.

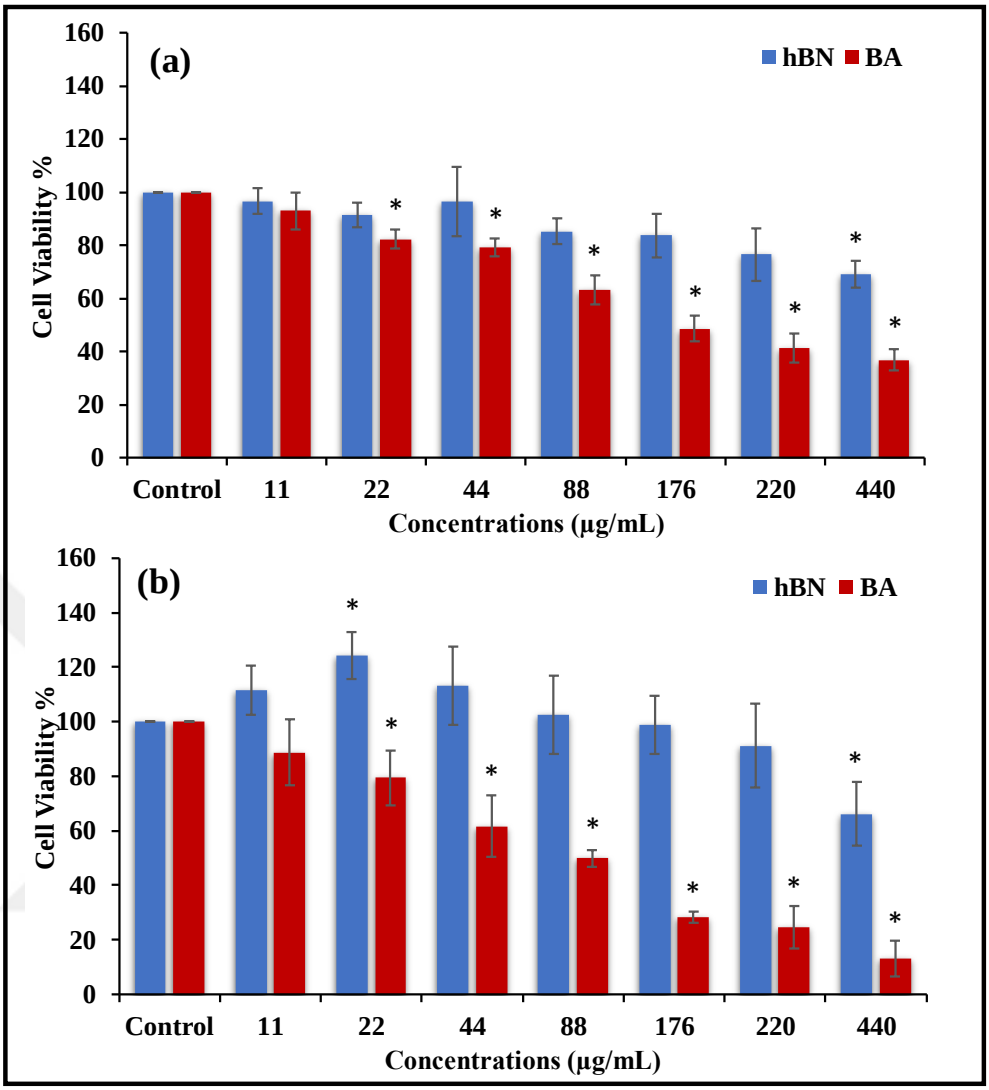

Figure 4.46. Viability of PC3 cells exposed to hBN and BA at the first (a) and third (b) days of incubation. (analyzed with student *t*-test $^{*}p < 0.05$)

The viability of hBN-exposed healthy prostate (PNT1A) cells was increased around 125 per cent (Figure 4.47a) and their viability was around 100 per cent up to 1000 µg/mL of hBNs concentrations at the third day of incubation (Figure 4.47b). However, BA-exposed PNT1A viability was decreased around 32 per cent at the third day of incubation, even it was around 127 per cent at the first day. According to these results DU145 cells seem as the most hBN sensitive cell line, while the PC3 has shown the maximum sensitivity against BA at the long incubation time. Moreover, the lack of negative effects on PNT1A cells up to 1000 µg/mL of hBNs indicates their safe applications in prostate cancer therapies.

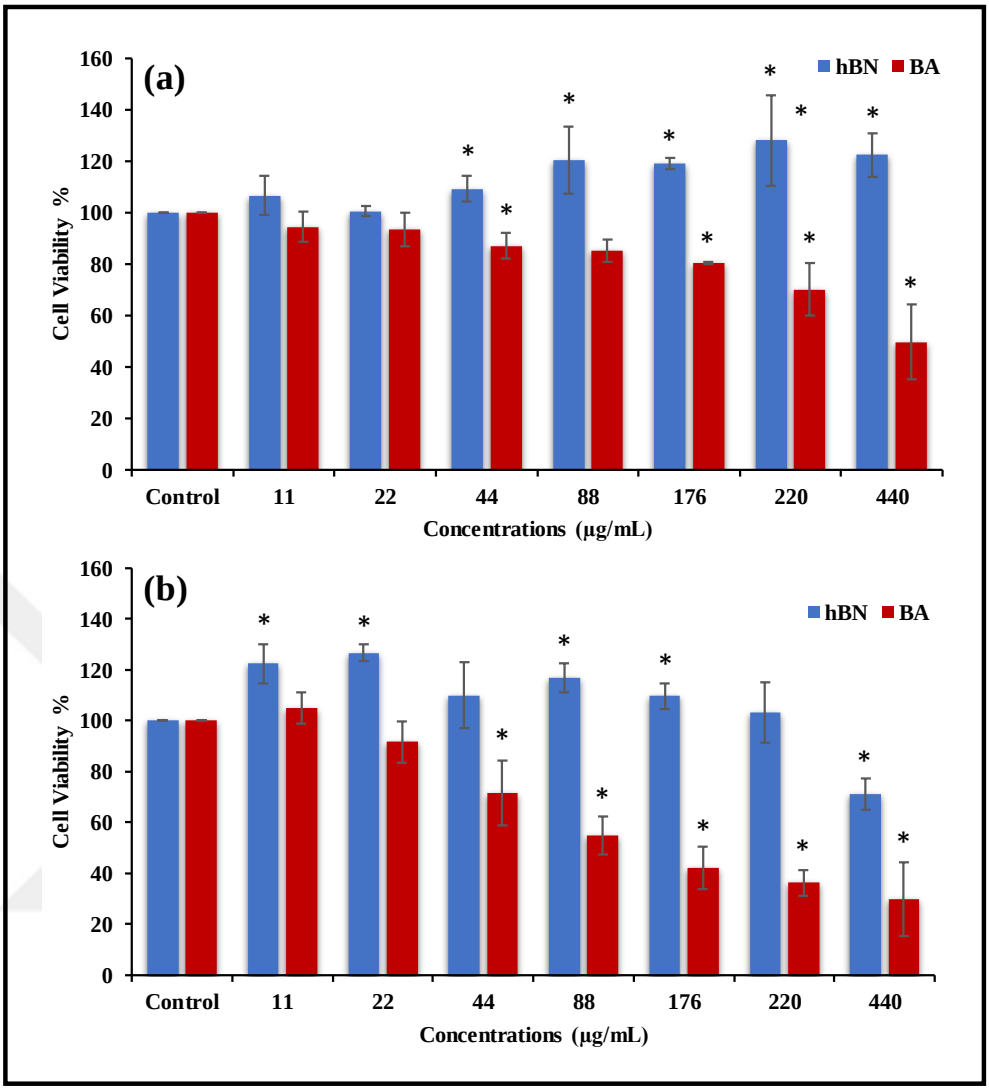

Figure 4.47. Viability of PNT1A cells exposed to hBN and BA at the first (a) and third (b) days of incubation. (analyzed with student *t*-test $^{*}p < 0.05$)

4.5.2. Cellular Uptake and Intracellular Degradation of hBNs

Cellular uptake of hBNs was comparatively investigated on DU145 cancer and PNT1A healthy prostate cells by measuring the side scattering of cells using flow cytometer as shown in Figure 4.48. The concentrations were limited as 22, 44, 88 and 176 µg/mL of boron including hBN and BA, as they are doses at which hBNs show optimum lethal effect on DU145 cells yet being completely safe for PNT1A cells. The internalization of hBNs was relatively analyzed by considering the maximum concentration (176 µg/mL) of boron

including hBN at the third day of incubation. The results show the hBN uptake significantly increased from 47 per cent to 94 per cent at increased concentrations in DU145 cells while they are increased from 26 per cent to 88 per cent at PNT1A cells at the first day of incubation as shown in Figure 4.48a. Next, the cellular internalization of the hBNs increased regularly from 61 per cent to 100 per cent at DU145 cells while it increased from 34 per cent to 98 per cent at PNT1A cells at the third day of incubation (Figure 4.48b). The results indicate that the hBN uptake of the DU145 cells significantly higher than the PNT1A cells up to 200 µg/mL of concentration however their uptake performances were same at 400 µg/mL of hBN concentrations. The higher cellular uptake performance of hBNs, even at the low concentrations, by DU145 cells, could be explained with their high nutrition requirements. Therefore, the hBN concentrations below 400 µg/mL could be chosen for safe accumulation in cancer cells which is up taken significantly lower by healthy cells.

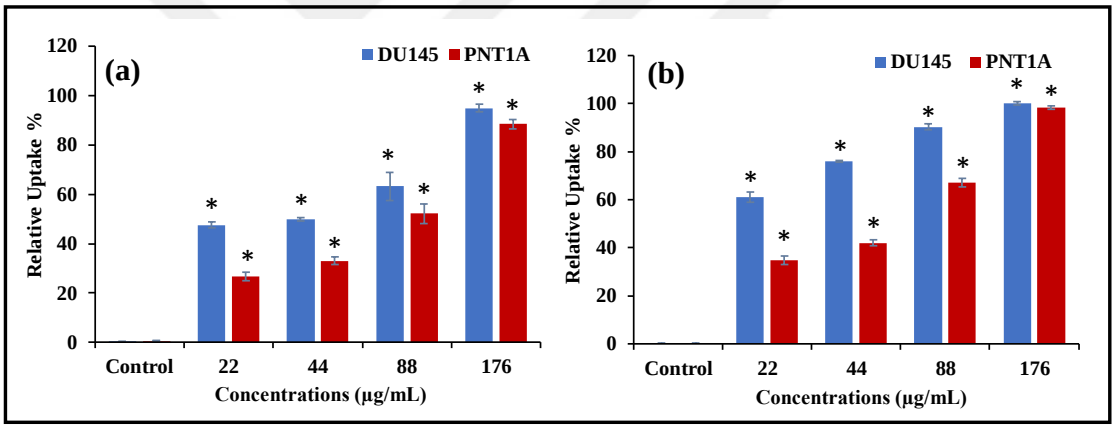

Figure 4.48. Cellular Uptake of hBNs at first (a) and third (b) days of incubation measured by flow cytometer (analyzed with student *t*-test $^{*}p < 0.05$)

Intracellular degradation of the hBNs in DU145 and PNT1A cells was measured using ICP-MS as shown in Figure 4.49. Following hBN and BA treatment of DU145 and PNT1A cells, the cells were lysed in order to release all B^{11} amount. The results indicate that the B^{11} amount was increased around 6 ppm in DU145 cells while a less increment (2 ppm) in PNT1A cells was found as compared to the control samples at the 22 µg/mL of concentration. Then the B^{11} release was increased around 13 and 15 ppm in DU145 cell while it was around 15 and 19 ppm in PNT1A cell at 44 and 88 µg/mL boron included hBN concentrations, respectively. According to the results, the hBNs were more efficiently degraded in PNT1A cells as compared to DU145 cells. Moreover, for the fate of BA there

are two possibilities: BA was not up taken by cells or eliminated from the cells in three days of incubation. Whichever is the option, we can conclude that BA is not useful agent for long term therapy of boron.

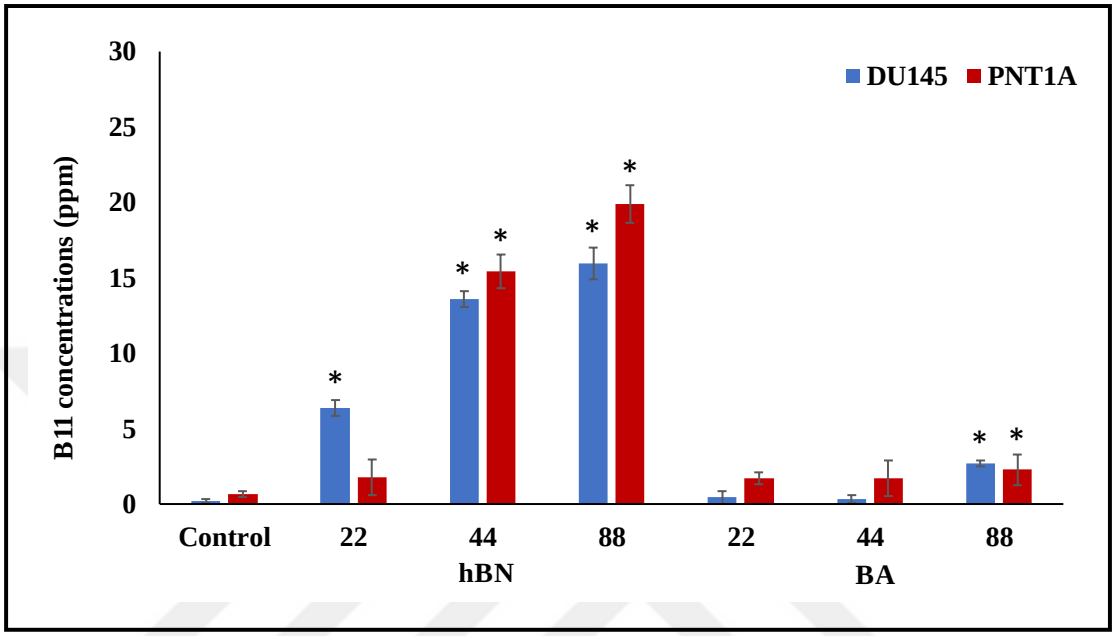

Figure 4.49. Intracellular degradation of hBNs at the third days of incubation measured with ICP-MS. (analyzed with student *t*-test $^{*}p < 0.05$)

4.5.3. Cell Cycle Analysis

The cell cycle in normal cells is controlled by series of signaling pathways that regulates cell growth, replication, and dividing; however, the mutations in cancer cell DNA can cause uncontrolled cell dividing due to the error in signaling pathways. While the GO/G1 phases of cells indicate the growth and the preparation for division, S or G2/M phases indicate normally dividing or arrested cells in DNA replication, or cell in division phase [207]. In this study, effect of hBNs on the phases of DU145 and PNT1A cell cycle were investigated at first and third days of incubation as shown in Figure 4.50 and 4.51. The percentage of hBN exposed DU145 cells in G2/M phase increased from 17 per cent to 23 per cent while the per cent of cells in G2/M phase of BA exposed cultures increased from 32 per cent to 46 per cent at the highest concentration (Figure 4.50a and b). Then, the percentage of hBN

exposed PNT1A cells in G2/M phase increased from 26 per cent to 33 per cent, while the G2/M phase per cent of BA exposed cells decreased from 39 per cent to 28 per cent at the highest concentrations as shown in Figure 4.50c and d. The results show that the BA is more effective on DU145 and PNT1A cell cycle than the hBN exposed cells while the hBN does not show any significant difference in accumulation of cell cycle G2/M phase at the first day of incubation.

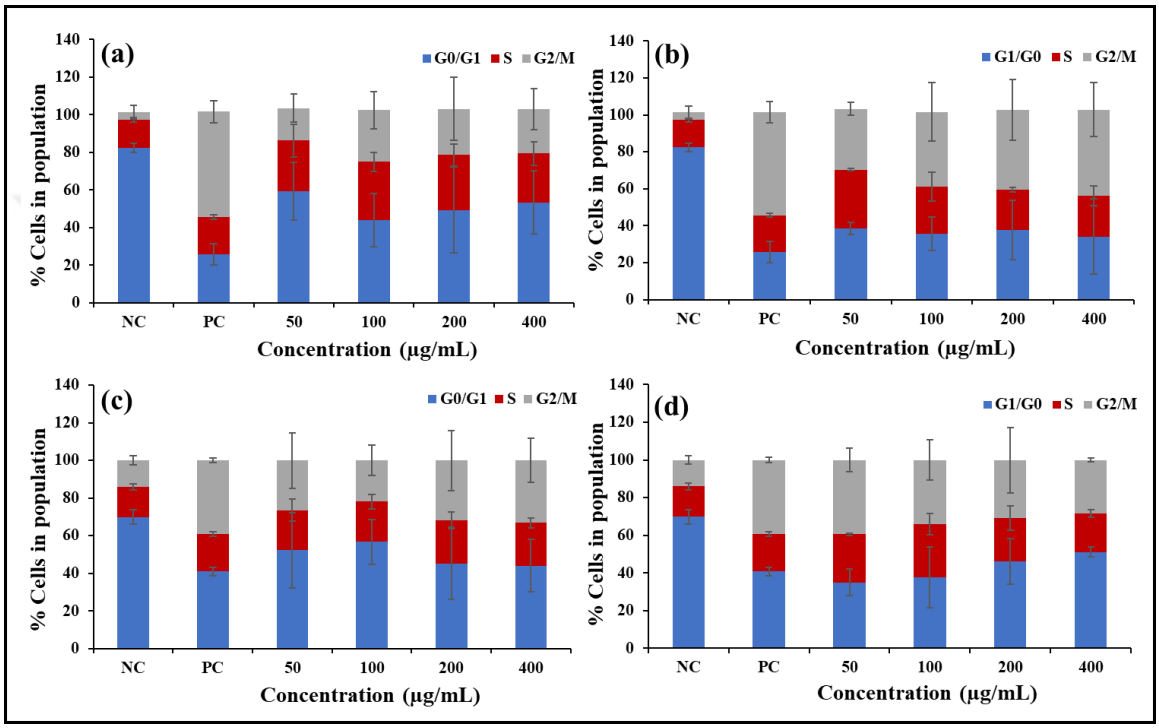

Figure 4.50. Cell cycle analysis of hBN and BA exposed DU145 cells (a and b) and PNT1A cells (c and d) at the first day of incubations, respectively.

In this part of the study, the results indicate that the per cent of arrested cells in G2/M phase increased directly proportionally to the increased hBN and BA concentrations at the third day of incubation as shown in Figure 4.51. The percentage of hBN exposed DU145 cells in G2/M phase increased from 17 per cent to 53 per cent, while the per cent of cells in G2/M phase of BA exposed cultures increased from 42 per cent to 63 per cent at the highest concentration and incubation times (Figure 4.51a and b). Then, the percentage of BA exposed PNT1A cells in G2/M phase increased from 9 per cent to 32 per cent, while the G2/M phase per cent of BA exposed cells decreased from 48 per cent to 55 per cent at the highest concentrations (Figure 4.51c and d). The results indicate that the hBNs show

relatively low accumulation as compared to BA exposed cells at G2/M phase of cell cycle in each concentration. Moreover, the G2/M phase accumulation of the hBN exposed DU145 and PNT1A cell cycle were quite similar to each other.

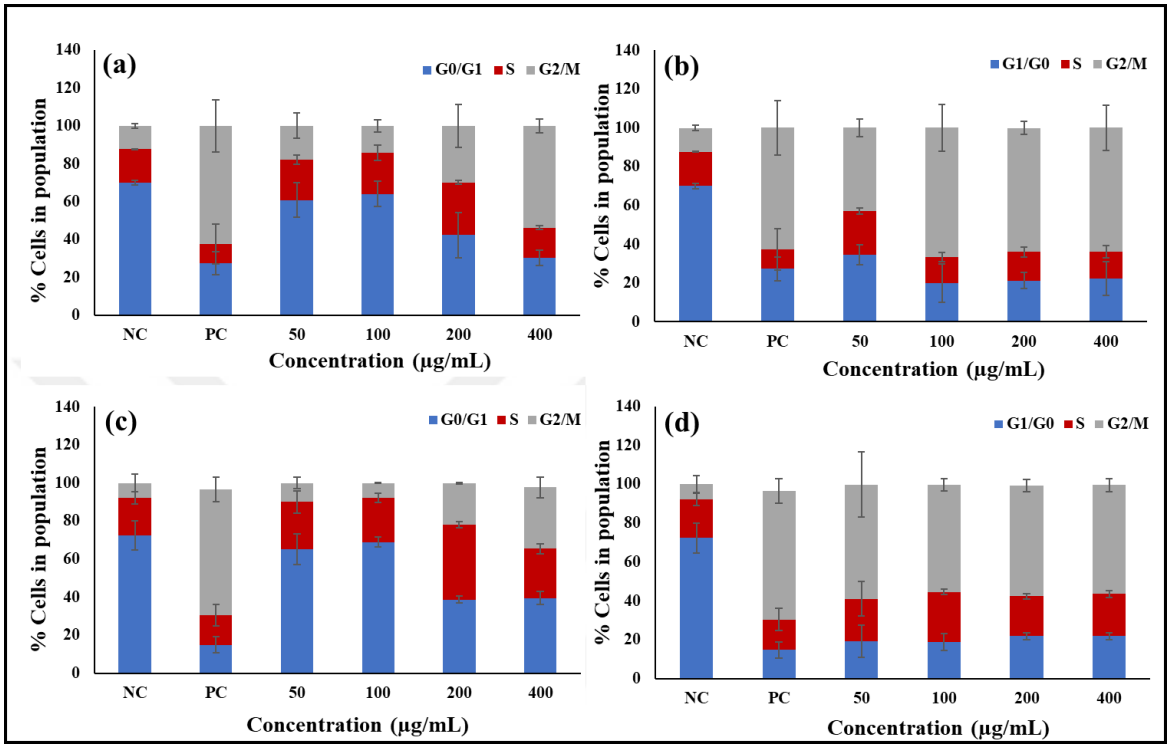

Figure 4.51. Cell cycle analysis of hBN and BA exposed DU145 cells (a and b) and PNT1A cells (c and d) at the third day of incubations, respectively.

As an indicator, G2/M phase accumulation of cells reveals significant information about the hBNs and BA on cell proliferation performance. The results indicate that the hBNs exposed DU145 and PNT1A cell proliferation was similar while BA exposed ones show higher cell proliferation decrease in each cell line as coherent with cell viability data shown in WST1 experiment results and reported in Figure 4.45, 4.46 and 4.47.

4.5.4. Mitochondrial Functionality

Since the essential functions of the mitochondria in cells, investigating their alteration following hBN internalization is very important to clarify the role of hBNs on cell metabolism. Therefore, mitochondrial function of cells was investigated. In this study, the mitochondrial disfunction of hBN and BA exposed DU145 and PNT1A cells were calculated

with respect to the normal mitochondrial function of the cells as shown in Figure 4.51. The results indicated that hBN and BA did not show any negative effect on mitochondrial functions of DU145 and PNT1A cells at the first day of incubation as seen in Figure 4.51a and b. However, the mitochondrial disfunction was significantly increased up to 5 per cent at maximum hBN concentration and 3 per cent at 88 µg/mL boron including BA concentration exposed DU145 cells as shown in Figure 4.51c. Moreover, the mitochondrial function of the PNT1A cells was not significantly affected at the third day of incubation as shown in Figure 4.51d. The results indicate that the hBN cause more mitochondrial disfunction then BA on DU145 cells at the third day of incubation, while the PNT1A cell mitochondria have normal functions at each time of incubation. Besides, the viability of the PNT1A cells and first day of DU145 cells could be accepted as reliable however the decrease in mitochondrial function of DU145 cell cause some incorrect viability results at the third day of incubation (Figure 4.45). Moreover, the decrease in mitochondrial function in DU145 cells at the third day of incubation stimulates the apoptosis of cells.

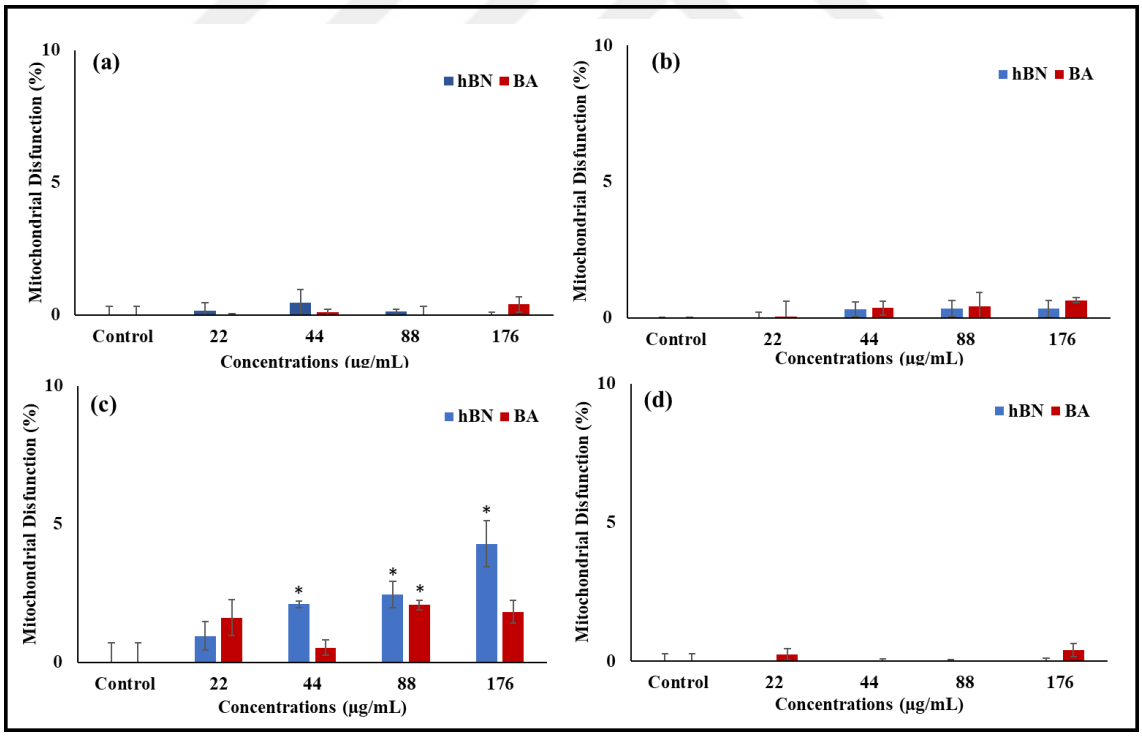

Figure 4.52. Mitochondrial dysfunction measurements on DU145 and PNT1A cells at the first (a and b) and third (c and d) days of incubation, respectively. (analyzed with student t-test $^{*}p < 0.05$)

4.5.5. ROS Production

Cells tend to increase ROS production when they are exposed to foreign substances as a result of defense mechanism. The increased ROS levels in mitochondria cause cellular stress that further stimulates ROS production. High ROS levels in the cells causes damages in the structure of many critical cell components such as proteins, membrane lipids, and DNA, that hinder cellular functions and activates apoptosis processes [208]. In this study, the ROS level of hBN and BA exposed DU145 and PNT1A cells were investigated at the first and third days of incubations as shown in Figure 4.52. The results indicate that the significant increment in ROS level of hBN exposed DU145 cells at the maximum concentration was around 51 per cent, while it was around 20 per cent in PNT1A cells at the first day of incubation as shown in Figure 4.52a and b. Then, the maximum ROS level was around 62 per cent in DU145 cells, while it was around 50 per cent in PNT1A cells at the 3 day of incubation as shown in Figure 4.52c and d. Besides, it is clearly seen that the ROS production of BA-exposed DU145 and PNT1A cells was at the same level in line with the negative control at the first day of incubation. The ROS level just increased in DU145 cells (around 10 per cent) at the third day of incubation. The results indicate that the DU145 cells show more reaction against hBN as compared to PNT1A cells by producing high level of ROS. Conversely, the BA cause a minimal ROS production in PNT1A cells.

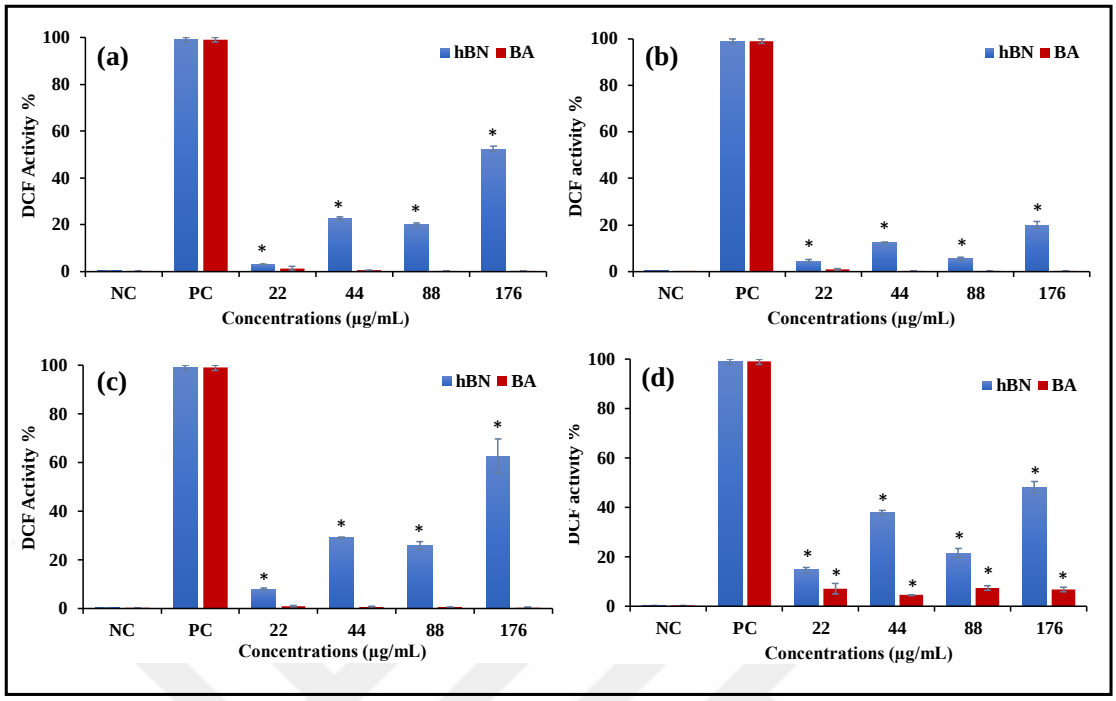

Figure 4.53. ROS production in hBN and BA exposed DU145 and PNT1A cells after 1 first (a and b) and 3 (c and d) days of incubation, respectively. (analyzed with student t-test $^{*}p < 0.05$)

4.5.6. Death Mechanism of Cells

Death mechanism of cells is affected by many parameters in the organism, including surrounding milieu, cell type, physiological state of the cells during the stimulation, stimulation agent type, and its concentration [209]. However, the process seems so much complicated, the optimal conditions were provided in *in vitro* conditions that mimics the organism. In this study, hBNs and BA exposed DU145 and PNT1A cells were labelled with anexin-V and PI as indicators of apoptosis and necrosis as seen in Figure 4.53, respectively. The results indicate that the just 28 per cent of DU145 cells was alive, while the 52 per cent, 11 per cent and 7 per cent of cells were in late apoptosis, apoptosis, and necrosis (Figure 4.53a), respectively. Moreover, 83 per cent of BA-exposed DU145 cells were alive, while 9 per cent of the cells were in apoptosis at the first day of incubation (Figure 4.53b). Then, the hBN exposed PNT1A cell death mechanism was shown in Figure 4.53c and d. The results indicate that the 39 per cent of PNT1A cells was alive while the 11 per cent of cells necrosis,

6 per cent of cells apoptosis and 42 per cent of cells were in late apoptosis. Moreover, 77 per cent of BA exposed PNT1A cells were alive while the 20 per cent of cells was in apoptosis.

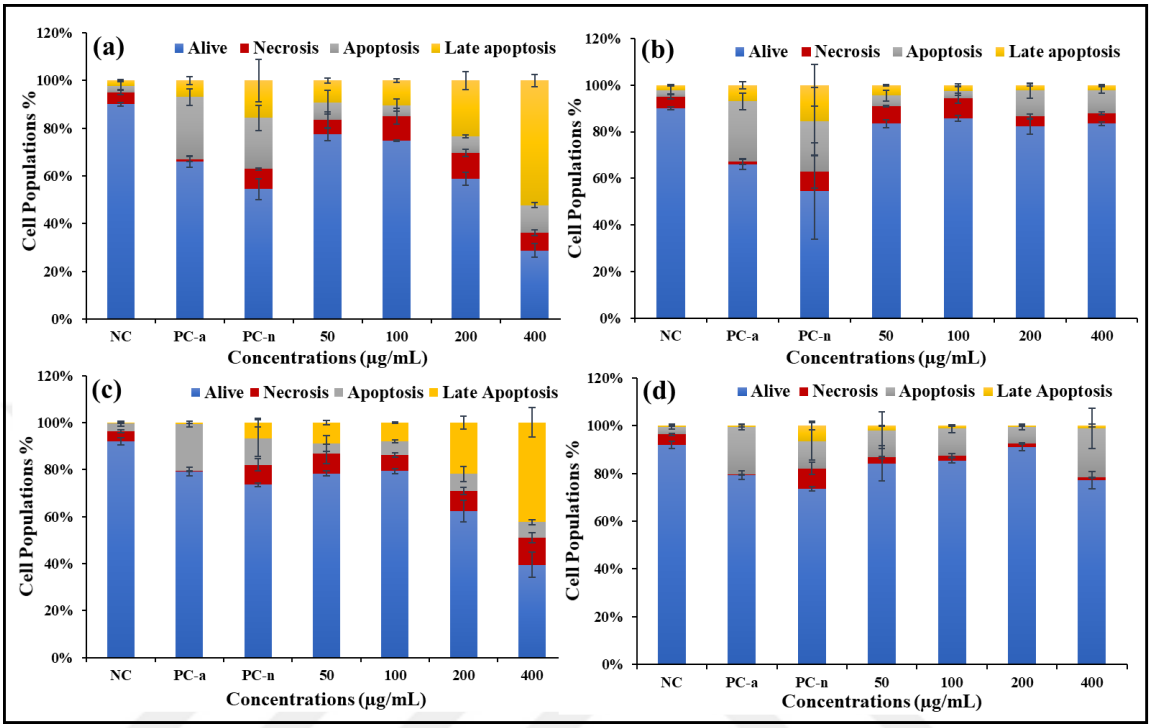

Figure 4.54. Cell death mechanism investigation in hBN and BA exposed DU145 cells (a and b) and PNT1A cells (c and d) at the first days of incubations, respectively.

At the third day of incubation, 20 per cent of hBN exposed DU145 cells was alive while 13 per cent of cells was in apoptosis and 63 per cent of cells in late apoptosis. Moreover, 64 per cent of BA exposed DU145 cells was alive while 24 per cent of the cells was in apoptosis as shown in Figure 4.55a and b. Then, 29 per cent of BA exposed DU145 cells was alive while 11 per cent of cells was in necrosis and 56 per cent of cells in late apoptosis. Moreover, 81 per cent of BA exposed DU145 cells was alive while 9 per cent of the cells was in apoptosis as shown in Figure 4.55c and d. The results indicate that the hBN cause serious late apoptotic phenomena in DU145 cells, that means intracellular phosphatidylserines were detected by Annexin-V and also PI intercalated into the DNA due to the permeabilization of cell membrane. Therefore, it is obvious that the DU145 cells are killed by hBNs relatively more then PNT1A cells with apoptosis mechanism as desired in cancer therapy applications.

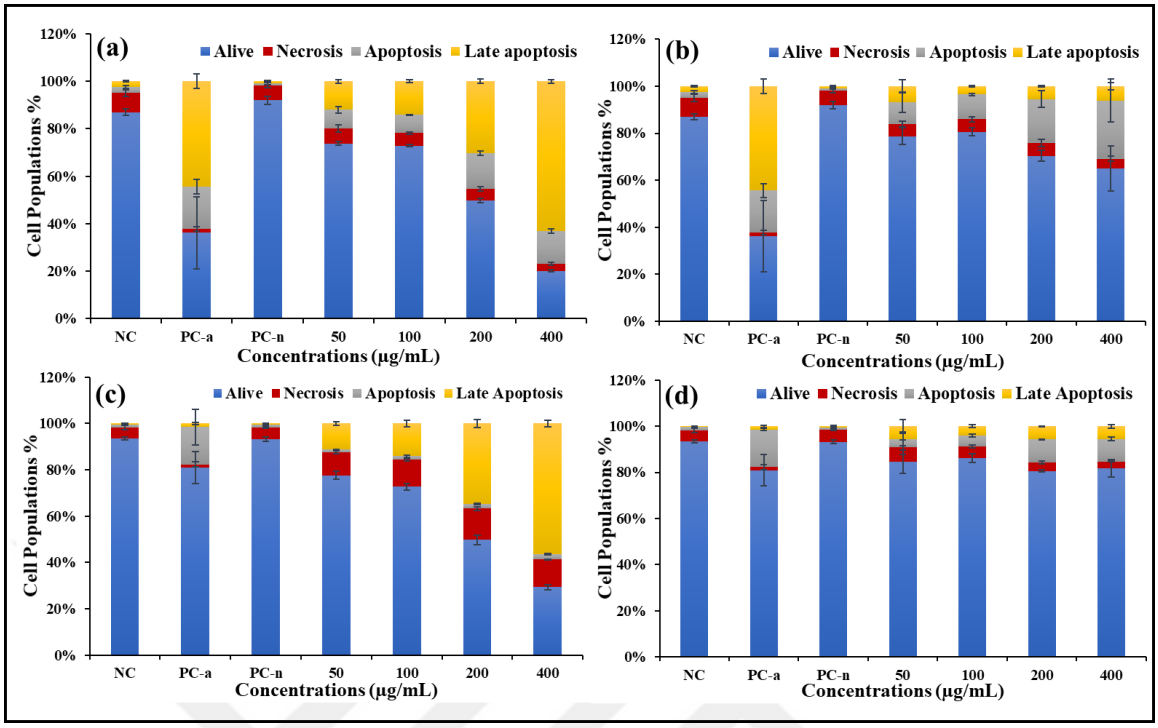

Figure 4.55. Cell death mechanism investigation in hBN and BA exposed DU145 cells (a and b) and PNT1A cells (c and d) at the third days of incubations respectively.

4.5.7. DNA Fragmentation

Double-strand breaks in nuclear DNA of cells are visible as fragments in gel electrophoresis. This kind of DNA breaks are consistent with apoptotic cell death [210]. Therefore, the DNA fragmentation experiment was performed on hBN and BA exposed DU145 and PNT1A cells as shown in Figure 4.54 to reveal the underlying reason of their deaths. As seen in the image, high concentration of hBNs (400 µg/mL) cause DNA fragmentation as light smear shape in the Figure 4.54.

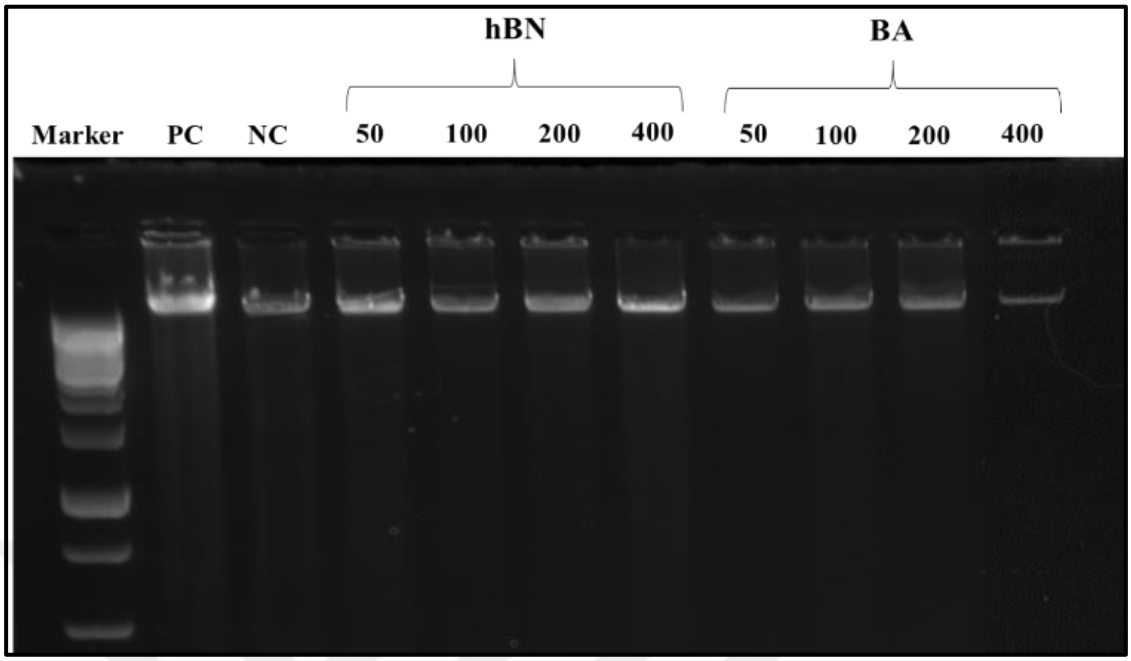

Figure 4.56. DNA fragmentation measurement in hBN and BA-exposed DU145 cells.

4.5.8. Cell Cytoskeleton Evaluation

Cytoskeleton of the cells serves in the metastasis and invasion of cancer cells by providing strong forces for movement [211]. F-actin is the major protein in cytoskeleton that plays crucial role in the “finger-like” shapes required to generate filopodia of cells, the structures that are responsible for cell movements. F-actin proteins also regulate intracellular trafficking [212]. In this study, hBN and BA exposed DU145 cell cytoskeleton and nucleus were observed by labelling f-actin with phalloidin and cell nucleus with DAPI (Figure 4.55). The images of cells exposed to hBN and BA show no significant difference from control cell cytoskeleton at the first day of incubation. However, the high number of ring-shaped f-actin filaments close to cellular membrane of hBN exposed cells could be attributed to the strong effort of the cells to excrete the hBNs accumulated in the cells. This result suggests that the f-actin is involved in hBN trafficking.

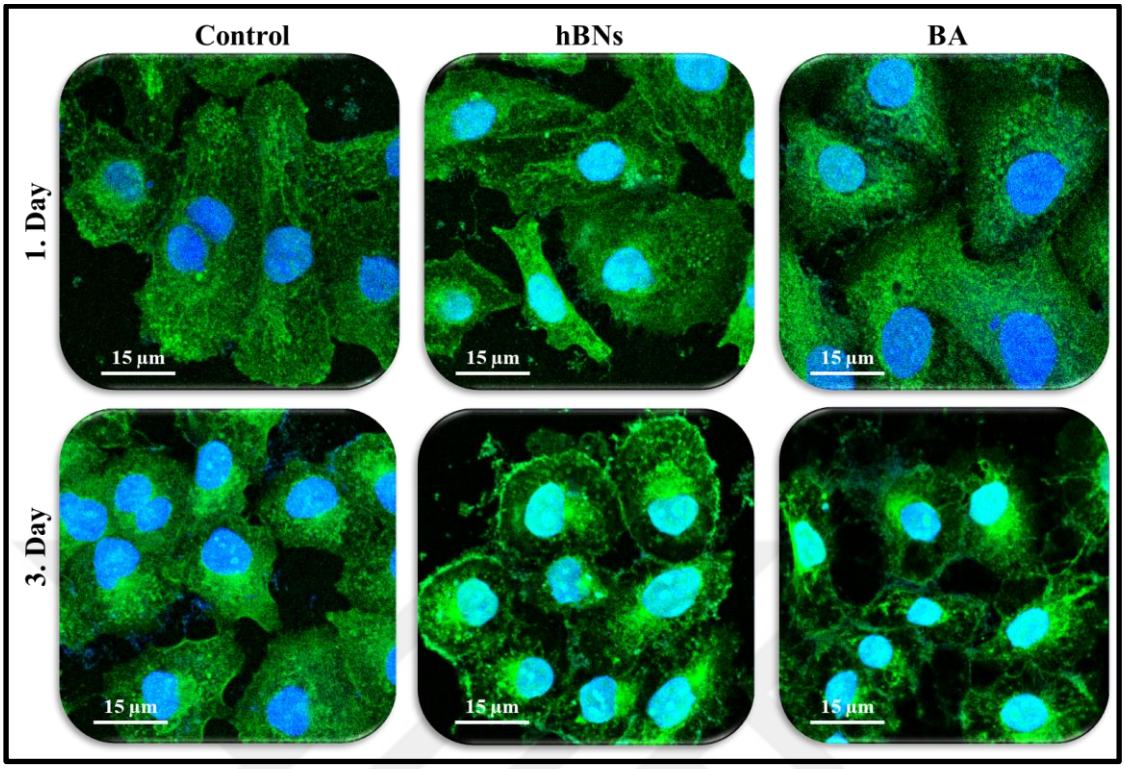

Figure 4.57. Confocal microscopy images of hBN and BA exposed DU145 cells cytoskeleton at the first and third day of incubations (f-actin in green, nuclei in blue).

From all results, as a most hBN sensitive cell line, DU145 cells efficiently up taken the hBNs and degraded the hBNs. The high concentrations of hBNs (200 and 400 µg/mL) seriously induced apoptosis by causing an increase at the ROS levels in cells. With the internalization of the hBNs, a rearrangement of the cytoskeleton was observed in a non-metastatic direction. However, the BA just induces cell viability decrease in cell metabolism which is attributed to their negative effects on cell proliferation.

5. CONCLUSIONS AND FUTURE PERSPECTIVES

The investigation of boron nitride nanotubes and hexagonal boron nitrides as a drug nanocarriers and as active agent in cancer treatment were demonstrated in the present work with promising results. Furthermore, four original research articles were published as outcomes as it can be found in the references [131, 213, 214 and 215], as well as a book chapter about biocompatibility of BNNTs [216]. Actually, through the time span of this thesis, from 2012 to 2018, a large number of promising studies was published about the potential use of BNNTs and hBNs as nanocarrier in cancer treatment [137, 153]. A study also was published about the usage of hBNs as an active anticancer agent in prostate cancer treatment [90], which definitely deserves their further evaluation. In this thesis, the biocompatibility of BNNTs and hBNs were investigated to reveal their potential biomedical use without any damage to healthy cells.

BNNTs were hydroxylated and modified with carbohydrates to increase their dispersibility in aqueous media and their cellular uptake by cancer cells. The cellular uptake of BNNTs, h-BNNTs, and m-BNNTs was investigated using confocal microscopy following the labeling with DAPI. The confocal microscopy images indicated that unmodified BNNTs, h-BNNTs and m-BNNTs were more efficiently internalized by A549 cells rather than HDF cells. The influence of BNNTs, h-BNNTs and m-BNNTs on viability, ROS generations and genotoxicity was evaluated using A549 cells and HDF cell lines. The results indicated that the unmodified BNNTs, h-BNNTs and m-BNNTs had no negative effects on viability of HDFs, whereas BNNTs and h-BNNTs were highly cytotoxic on A549 cells at high concentrations (100–200 g/mL). The ROS generation in BNNTs and h-BNNTs exposed A549 cells was seriously increased and revealed to be directly proportional to their genotoxic effect on this cell line at higher concentrations (100–200 g/mL), confirming the cell viability results. The difference in the toxicity results of BNNTs on HDFs and A549 cells can be attributed to the higher cellular uptake capacity of the cancer cells as compared to the healthy cells. However, the high cellular viability could be attributed to the positive effects of the carbohydrate modification on cancer cell proliferation. This study suggests that BNNTs, h-BNNTs, but especially m-BNNTs, can be safely used as drug carrying agents. Moreover, they could be exploited as therapeutic agents owing to the cytotoxic effects on cancer cells at higher concentrations.

Moreover, the biocompatibility of h-BNNTs was studied on microorganisms (*saccharomyces cerevisiae*) decorated with h-BNNTs and pairs of biocompatible polyelectrolytes. The LbL coating of PEs around the yeast facilitates the effective immobilization of the h-BNNTs on the yeast cell walls. The viability test results show that the h-BNNTs do not reduce the physiological activity in the cells. We believe that the Pes/h-BNNT-coated yeast can be considered as a good candidate to fabricate living cell-based biosensors which are sensitive to hydrophobic toxic agents in the environment.

Then, the biocompatibility of the hBNs was investigated with cell viability experiments and the results indicated their biocompatible nature up to very high concentrations. Therefore, hBNs could be accepted as a good candidate for the potential biomedical applications of drug carrying and as therapeutic agent.

Moreover, a comparative study to explore the potentials of BNNTs and hBNs as novel nanocarriers was conducted. It was found that a higher concentration of Dox could be loaded onto BNNTs compared with hBNs. It was clear that the pH of the medium at the time of loading and release was an important factor. The optimal loading was achieved at neutral and basic pH values, threefold higher with respect to acidic pH. The decreased pH triggered the increased release of the drug from BNNTs. This can be an important point for effective release in intracellular acidic compartments after uptake into the cells. Further, the conjugation of Dox–BNNTs with folate helps effective targeting to cancer cells. The results also indicate that the genotoxic Dox molecules also accumulate in the nucleus of the cells as desired even though they were conjugated with the carrier BNNT structures. This study suggests that BNNTs are a potential candidate as an effective carrier of aromatic ring containing chemotherapy drugs to improve their therapeutic efficiency and to reduce their side effects.

Then, hBNs were synthesized in the absence of a catalyst, a potential contaminant and used in the rest of the study. The hBNs were intended to be generated as a boron-based active agent for BNCT applications. Due to the hydrophobic nature of the hBNs, they were first functionalized with DSPE-PEG-NH_2 to increase dispersibility in aqueous media and to provide reactive -NH_2 ends for further functionalization. Then, the transferrin protein as a brain cancer cell targeting agent was covalently bound to the active ends of the DSPE-PEG-hBNs. The comparatively performed characterization studies indicated an optimal DSPE-PEG-NH_2 interaction. Promisingly, the transferrin functionalization of the hBNs

significantly increased their cellular uptake and caused a dose-dependent cell viability decrement in glioblastoma cancer cells.

As a promising agent, the therapeutic efficiency of hBNs against prostate cancer was investigated in comparison to BA on cancer and healthy cells. First of all, several prostate cancer cells and healthy prostate cell viabilities were tested to reveal the hBN and BA sensitivity that resulted with cellular death. According to the results, the hormone-independent DU145 prostate cancer cells showed highest sensitivity against hBNs whereas the healthy cells do not show significant sensitivity against hBN exposure. Then, the cellular uptake and intracellular degradation studies of hBNs indicated their slow degradation following efficient cellular uptake. Moreover, the sensitivity studies were supported with cell cycle analysis. In agreement with the sensitivity results, cycle of the DU145 cells were arrested in mitosis phase in long incubation times with hBN and BA. Besides, the mitochondrial response of the cells gives important clues about the cellular response following the hBN uptake. Based on the data, mitochondrial disfunction and ROS generation significantly increased in hBN-treated DU145 cells, resulting into a seriously increased late apoptosis at the long-term incubation. Concerning the cytoskeleton, structures of cells plays very important role in cancer metastasis, ring formation of f-actin filaments in hBN treated conditions indicates the constructed vesicular structures as a priority of cells in place of metastasis.

Although the findings of this study indicate these nanomaterials quite promising as drug carrier and therapeutic agent, their further evaluation is necessary. First, their degradation profile in biological conditions should be investigated. Then, the cellular uptake mechanism can be studied in order to clarify the underlying reason of higher cellular uptake by cancer cells that might give some clues to increase the uptake profile by cancer cells selectively.

Overall, it is possible to carry chemotherapeutic drugs to the target cancerous cells by loading onto BNNTs and thereafter release at precise pH values. Moreover, cellular investigations demonstrated that hBNs can be good candidates for boron-based structure accumulation in the target cells for possible BNCT applications in virtue of their biocompatible nature. In the light of the present study, the apoptotic stimulation and the metastasis preventive effect of the hBNs encourage us to continue to the next step of *in vivo* testing for their role in cancer therapy.

REFERENCES

1. Ewart W. The use of creosoted oil for the expulsion of tracheal false membranes after tracheotomy; and of intranasal injections of oil in various affections. *British Medical Journal.* 1952;1:1381-1383.

2. Rodriguez A, Tatter SB, Debinski W. Neurosurgical techniques for disruption of the blood-brain barrier for glioblastoma treatment. *Pharmaceutics.* 2015;7(3):175-87.

3. Calias P, Banks WA, Begley D, Scarpa M, Dickson P. Intrathecal delivery of protein therapeutics to the brain: A critical reassessment. *Pharmacology and Therapeutics.* 2014;144(2):114-122.

4. Kadoch C, Li J, Wong VS, Chen L, Cha S, Munster P, Lowell CA, Shuman MA, Rubenstein JL. Complement activation and intraventricular rituximab distribution in recurrent central nervous system lymphoma. *Clinical Cancer Research.* 2014;20(4):1029-1041.

5. Ram Z, Culver KW, Oshiro EM, Viola JJ, DeVroom HL, Otto E, Long Z, Chiang Y, McGarrity GJ, Muul LM, Katz D, Blaese RM, Oldfield EH. Therapy of malignant brain tumors by intratumoral implantation of retroviral vector-producing cells. *Nature Medicine.* 1997;3(12):1354-1361.

6. Paoli EE, Ingham ES, Zhang H, Mahakian LM, Fite BZ, Gagnon MK, Tam S, Kheirolomoom A, Cardiff RD, Ferrara KW. Accumulation, internalization and therapeutic efficacy of neuropilin-1-targeted liposomes. *Journal of Control Release.* 2014;178:108-117.

7. Zou LL, Ma JL, Wang T, Yang TB, Liu CB. Cell-penetrating peptide-mediated therapeutic molecule delivery into the central nervous system. *Current Neuropharmacology.* 2013;11:197-208.

8. Ben-Zvi A, Lacoste B, Kur E, Andreone BJ, Mayshar Y, Yan H, Gu C. Mfsd2a is critical for the formation and function of the blood-brain barrier. *Nature.* 2014;509(7501):507-511.

9. Jones AR, Shusta EV. Blood-brain barrier transport of therapeutics via receptor-mediation. *Pharmaceutical Research.* 2007;24(9):1759-1771.

10. Pardridge WM. The Blood-brain barrier: Bottleneck in brain drug development. *NeuroRx.* 2005;2:3-14.

11. McDannold N, Vykhodtseva N, Raymond S, Jolesz FA, Hynynen K. MRI-guided targeted blood-brain barrier disruption with focused ultrasound: histological findings in rabbits. *Ultrasound in Medicine and Biology.* 2005;31(11):1527-1537.

12. Cowles AL, Fenstermacher JD, Sartorelli AC, Johns DG. Theoretical considerations in the chemotherapy of brain tumors. *Antineoplastic and Immunosuppressive Agents 1.* 1974;38:319-329.

13. Riina HA, Fraser JF, Fralin S, Knopman J, Scheff RJ, Boockvar JA. Superselective intraarterial cerebral infusion of bevacizumab: a revival of interventional neuro-oncology for malignant glioma. *Journal of Experimental Therapeutics and Oncology*. 2009;8:145-150.

14. Laske DW, Youle RJ, Oldfield EH. Tumor regression with regional distribution of the targeted toxin TF- CRM107 in patients with malignant brain tumors. *Nature Medicine.* 1997;3:1362–1368.

15. Parsons LH, Justice JB. Quantitative approaches to in vivo brain microdialysis. *Critical Reviews in Neurobiology.* 1994;8:189–220.

16. Lipinski CA, Lombardo F, Dominy BW, Feeney PJ. Experimental and computational approaches to estimate solubility and permeability in drug discovery and development settings. *Advanced Drug Delivery Reviews.* 2001;46:3–26.

17. Pandey PK, Sharma AK, Gupta U. Blood brain barrier: An overview on strategies in drug delivery, realistic in vitro modeling and in vivo live tracking. *Tissue Barriers.* 2016;4(1)e1129476.

18. Li Y, He H, Jia X, Lu WL, Lou J, Wei Y. A dual-targeting nanocarrier based on poly(amidoamine) dendrimers conjugated with transferrin and tamoxifen for treating brain gliomas. *Biomaterials*. 2012;33(15):3899-3908.

19. Gupta Y, Jain A, Jain SK, Transferrin-conjugated solid lipid nanoparticles for enhanced delivery of quinine dihydrochloride to the brain. *Journal of Pharmacy and Pharmacology*. 2007;59:935-940.

20. Huang RQ, Qu YH, Ke WL, Zhu JH, Pei YY, Jiang C. Efficient gene delivery targeted to the brain using a transferrin-conjugated polyethyleneglycol-modified polyamidoamine dendrimer. *The FASEB Journal*. 2007;21(4):1117-1125.

21. Lowe SW, Ruley HE Jacks T, Housman DE. P53-dependent apoptosis modulates the cytotoxicity of anticancer agents. *Cell.* 1993;74(6):957-967.

22. Chari RVJ. Targeted cancer therapy: Conferring specificity to cytotoxic drugs. *Accounts of Chemical Research.* 2008;41(1):98-107.

23. Nitiss JL. Targeting DNA topoisomerase II in cancer chemotherapy. *Nature Reviews Cancer.* 2009;9(5):338-350.

24. Cheung-Ong K, Giaever G, Nislow C. DNA-damaging agents in cancer chemotherapy: serendipity and chemical biology. *Chemistry and Biology.* 2013;20(5):648-659.

25. Xia Y. Nanomaterials at work in biomedical research. *Natural Materials.* 2008;7:758-760.

26. Wang J, Lee CH, Bando Y, Golberg D, Yap YK. Multiwalled boron nitride nanotubes: growth, properties, and applications, in: B-C-N nanotubes and related nanostructures. *Springer.* 2009;23-44.

27. Zhou Y, Peng Z, Seven ES, Leblanc RM. Crossing the blood-brain barrier with nanoparticles. *Journal of Control Release.* 2018;28(270):290-303.

28. Qiao W, Wang B, Wang Y, Yang L, Zhang Y, Shao P. Cancer therapy based on nanomaterials and nanocarrier systems. *Journal of Nanomaterials.* 2010;21:7-16.

29. Torchilin VP. Micellar nanocarriers: pharmaceutical perspectives. *Pharmaceutical Research.* 2007;24(1):1-16.

30. Dhanikula RS, Hildgen P. Synthesis and evaluation of novel dendrimers with a hydrophilic interior as nanocarriers for drug delivery. *Bioconjugate Chemistry.* 2006;17(1):29-41.

31. Chen T, Zhao T, Wei D, Wei Y, Li Y, Zhang H. Core shell nanocarriers with ZnO quantum dots-conjugated Au nanoparticle for tumor-targeted drug delivery. *Carbohydrate Polymers.* 2013;92(2):1124-1132.

32. Liu Z, Fan AC, Rakhra K, Sherlock S, Goodwin A, Chen X, Yang Q, Felsher DW, Dai H. Supramolecular stacking of doxorubicin on carbon nanotubes for in vivo cancer therapy. *Angewandte Chemie International Edition.* 2009;48(41):7668-7672.

33. Gu X, Ding J, Zhang Z, Li Q, Zhuang X, Chen X. Polymeric nanocarriers for drug delivery in osteosarcoma treatment. *Current Pharmaceutical Design.* 2015;21(36):5187-5197.

34. Ghosh P, Han G, De M, Kim CK, Rotello VM. Gold nanoparticles in delivery applications. *Advanced Drug Delivery Reviews.* 2008;60(11):1307-1315.

35. Gref R, Domb A, Quellec P, Blunk T, Müller RH, Verbavatz JM, Langerf R. The controlled intravenous delivery of drugs using PEG-coated sterically stabilized nanospheres. *Advanced Drug Delivery Reviews.* 1995;16:215-233.

36. Abbott NJ, Patabendige AAK, Dolman DEM, Yusof SR, Begley DJ. Structure and function of the blood–brain barrier. *Neurobiology of Disease.* 2010;37:13-25.

37. Wang ZH, Wang ZY, Sun CS, Wang CY, Jiang TY, Wang SL. Trimethylated chitosan-conjugated PLGA nanoparticles for the delivery of drugs to the brain. *Biomaterials.* 2010;31:908-915.

38. Provenzale JM, Mukundan S, Dewhirst M. The role of blood-brain barrier permeability in brain tumor imaging and therapeutics. *American Journal of Roentgenology.* 2005;185:763-767.

39. Mamot C, Drummond DC, Greiser U, Hong K, Kirpotin DB, Marks JD, Park JW. Epidermal growth factor receptor (EGFR)-targeted immunoliposomes mediate

specific and efficient drug delivery to EGFR- and EGFRvIII-overexpressing tumor cells. *Cancer Research.* 2003;63(12):3154-3161.

40. Zhang W, Zhang Z, Zhang Y. The application of carbon nanotubes in target drug delivery systems for cancer therapies. *Nanoscale Research Letters.* 2011;6(1):555-576.

41. Ciofani G, Del Turco S, Genchi GG, D'Alessandro D, Basta G, Mattoli V. Transferrin-conjugated boron nitride nanotubes: protein grafting, characterization, and interaction with human endothelial cells. *International Journal of Pharmaceutics.* 2012;436(1-2):444-453.

42. Heister E, Neves V, Tîlmaciu C, Lipert K, Beltrána VS, Coley HM, Silva SRP, McFadden J. Triple functionalisation of single-walled carbon nanotubes with doxorubicin, a monoclonal antibody, and a fluorescent marker for targeted cancer therapy. *Carbon.* 2009;47(9):2152-2160.

43. Dinan NM, Atyabi F, Rouini M-R, Amini M, Golabchifar A-A, Dinarvand R. Doxorubicin loaded folate-targeted carbon nanotubes: preparation, cellular internalization, in vitro cytotoxicity and disposition kinetic study in the isolated perfused rat liver. *Materials Science and Engineering: C.* 2014;39:47-55.

44. Lvov Y, Wang W, Zhang L, Fakhrullin R. Halloysite clay nanotubes for loading and sustained release of functional compounds. *Advanced Materials.* 2016;28(6):1227-1250.

45. Ciofani G, Raffa V, Menciassi A, Cuschieri A. Folate functionalized boron nitride nanotubes and their selective uptake by glioblastoma multiforme cells: implications for their use as boron carriers in clinical boron neutron capture therapy. *Nanoscale Research Letters.* 2009;4(2):113-121.

46. Ferreira TH, Marino A, Rocca A, Liakos I, Nitti S, Athanassiou A, Mattoli V, Mazzolai B, de Sousa EM, Ciofani G. Folate-grafted boron nitride nanotubes: possible exploitation in cancer therapy. *International Journal of Pharmaceutics. 2015*;481:56-63.

47. Burger PC, Vogel FS, Green SB, Strike TA. Pathologic Criteria and Prognostic Implications. *Cancer.* 1985;56:1106-1111.

48. Zinn PO, Majadan B, Sathyan P, Singh SK, Majumder S, Jolesz FA, Colen RR. Radiogenomic Mapping of Edema/Cellular Invasion MRI-Phenotypes in Glioblastoma Multiforme. *PLOS ONE.* 2011;7(2):101371.

49. Gallego O. Nonsurgical treatment of recurrent glioblastoma. *Current Oncology.* 2015;22:273-281.

50. Hanif F, Muzaffar K, Perveen K, Malhi SM, Simjee SU. Glioblastoma multiforme: a review of its epidemiology and pathogenesis through clinical presentation and treatment. *Asian Pacific Journal of Cancer Prevention.* 2017;18(1):3-9.

51. Castro MG, Cowenc R, Williamson IK, David A, Jimenez-Dalmaroni MJ, Yuan X, Bigliari A, Williams JC, Hu J, Lowenstein PR. Current and future strategies for the treatment of malignant brain tumors. *Pharmacology and Therapeutics. 2003*;98:71-108.

52. Krex D, Klink B, Hartmann C, Deimling A, Pietsch T, Simon M, Sabel M, Steinbach JP, Heese O, Reifenberger G, Weller M, Schackert G. Long-term survival with glioblastoma multiforme. *Brain.* 2007;130:2596-2606.

53. Cheng Y, Morshed R, Auffinger B, Tobias AL, Lesniak MS. Multifunctional Nanoparticles for Brain Tumor Diagnosis and Therapy. *Advanced Drug Delivery Reviews.* 2014;0:42-57.

54. Mirimanoff RO, Gorlia T, Mason W, Van den Bent MJ, Kortmann RD, Fisher B, Reni M, Brandes AA, Curschmann J, Villa S, Cairncross G, Allgeier A, Lacombe D, Stupp R. Radiotherapy and temozolomide for newly diagnosed glioblastoma: recursive partitioning analysis of the EORTC 26981/22981-NCIC CE3 phase III randomized trial. *Journal of Clinical Oncology.* 2006;24(16):2563-2569.

55. Laperriere N, Zuraw L, Cairncross G. Radiotherapy for newly diagnosed malignant glioma in adults: A systematic review. *Radiotherapy and Oncology.* 2002;64:259-273.

56. Walker MD, Green SB, Byar DP. Randomized comparisons of radiotherapy and nitrosoureas for the treatment of malignant glioma after surgery. *The New England Journal of Medicine.* 1980;303:1323-29.

57. Sheehan JP, Shaffrey ME, Gupta B, Larner J, Rich JN, Park DM. Improving the radiosensitivity of radioresistant and hypoxic glioblastoma. *Future Oncology.* 2010;6:1591-601.

58. Newhauser WD, Durante M. Assessing the risk of second malignancies after modern radiotherapy. *Nature Reviews Cancer.* 2011;11(6):438-448.

59. Johnson DR, O'Neill BP. Glioblastoma survival in the United States before and during the temozolomide era. *Journal of Neuro-Oncology.* 2012;107:359-364.

60. Stupp R, Dietrich PY, Ostermann Kraljevic S, Pica A, Maillard I, Maeder P, Meuli R, Janzer R, Pizzolato G, Miralbell R, Porchet F, Regli L, Tribolet N, Mirimanoff RO, Leyvraz S. Promising survival for patients with newly diagnosed glioblastoma multiforme treated with concomitant radiation plus temozolomide followed by adjuvant temozolomide. *Journal of Clinical Oncology.* 2002;20:1375-1382.

61. Pazdur R, Coia LR, Hoskins WJ, Wagman LD. Cancer management: a multidisciplinary approach. *Journal Oncology.* 2007;21:9-10.

62. Vigliani MC, Duyckaerts C, Hauw JJ, Poisson M, Magdelenat H, Delattre JY. Dementia following treatment of brain tumors with radiotherapy administered alone or in combination with nitrosourea-based chemotherapy: a clinical and pathological study. *Journal of Neuro-Oncology.* 1999;41:137-149.

63. Stupp R, Hegi ME, Mason WP, van den Bent MJ, Taphoorn MJB, Janzer RC, Ludwin SK, Allgeier A, Fisher B, Belanger K, Hau P, Brandes AA, Gijtenbeek J, Marosi C, Vecht CJ, Mokhtari K, Wesseling P, Villa S, Eisenhauer E, Gorlia T. Effects of radiotherapy with concomitant and adjuvant temozolomide versus radiotherapy alone on survival in glioblastoma in a randomised phase III study: 5-year analysis of the EORTC-NCIC trial. *Neurological Surgery.* 2009;10:459-466.

64. Moss RL. Critical review, with an optimistic outlook, on boron neutron capture therapy (BNCT). *Applied Radiation and Isotopes.* 2014;88:2-11.

65. Gregory CW, He B, Johnson RT, Ford OH, Mohler JL, French FS, Wilson EM. A mechanism for androgen receptor-mediated prostate cancer recurrence after androgen deprivation therapy. *Cancer Research.* 2001;61:4315-4319.

66. Parkin DM, Bray F, Ferlay J, Pisani P. Global cancer statistics. CA: *A Cancer Journal for Clinicians.* 2005;55:74-108.

67. Eskicorapci SY, Türkeri L, Karabulut E, Çal Ç, Akpınar H, Baltacı S, Baykal K, Kattan MW, Özen H. Validation of two preoperative kattan nomograms predicting recurrence after radical prostatectomy for localized prostate cancer in turkey: a multicenter study of the uro-oncology society. *Urology.* 2009;74(6):1289-1295.

68. Braeckman J, Michielsen D. Prognostic factors in prostate cancer. *Recent Results in Cancer Research.* 2007;175:25-32.

69. Stamey TA, Caldwell M, McNeal JE, Nolley R, Hemenez M, Downs J. The prostate specific antigen era in the United States is over for prostate cancer: what happened in the last twenty years? *Journal of Urology.* 2004;172(4):1297-1301.

70. Sobin LH, Wittekind C. *UICC TNM classification of malignant tumours.* New York: John Wiley & Sons; 2002.

71. D'Amico AV, Whittington R, Malkowicz SB, Schultz D, Blank K, Broderick GA, Tomaszewski JE, Renshaw AA, Kaplan I, Beard CJ, Wein A. Biochemical outcome after radical prostatectomy, external beam radiation therapy, or ınterstitial radiation therapy for clinically localized prostate cancer. *JAMA.* 1998;280(11):969-974.

72. Gregory CW, He B, Johnson RT, Ford OH, Mohler JL, French FS, Wilson EM. A mechanism for androgen receptor-mediated prostate cancer recurrence after androgen deprivation therapy. *Cancer Research.* 2001;61:4315-4319.

73. Dotan ZA, Ramon J. Staging of prostate cancer. *Recent Results in Cancer Research. 2007*;109-130.

74. Cheng L, Zincke H, Blute ML, Bergstralh EJ, Scherer B, Bostwick DG. Risk of prostate carcinoma death in patients with lymph node metastasis. *Cancer.* 2001;91:66-73.

75. Kyprianou N, English HF, Isaacs JT. Programmed cell death during regression of pc-82 human prostate cancer following androgen ablation. *Cancer Research.* 1990;50:3748-3753.

76. Ghosh A, Heston WDW. Tumor target prostate specific membrane antigen (PSMA) and its regulation in prostate cancer. *Journal of Cellular Biochemistry.* 2004;91(3):528-539.

77. Dhar S, Gu FX, Langer R, Farokhzad OC, Lippard SJ. Targeted delivery of cisplatin to prostate cancer cells by aptamer functionalized Pt(IV) prodrug-PLGA–PEG nanoparticles. *PNAS.* 2008;105(45):17356-17361.

78. Patri AK, Myc A, Beals J, Thomas TP, Bander NH, Baker JR. Synthesis and in vitro testing of J591 antibody−dendrimer conjugates for targeted prostate cancer therapy. *Bioconjugate Chemistry.* 2004;15(6):1174-1181.

79. Kumar A, Huo S, Zhang X, Liu J, Tan A, Li S, Jin S, Xue X, Zhao YY, Ji T, Han L, Liu H, Zhang XN, Zhang J, Zou G, Wang T, Tang S, Liang XJ. Neuropilin-1-targeted gold nanoparticles enhance therapeutic efficacy of platinum(iv) drug for prostate cancer treatment. *ACS Nano.* 2014;8(5):4205-4220.

80. Banerjee R, Tyagi P, Li S, Huang L. Anisamide-targeted stealth liposomes: A potent carrier for targeting doxorubicin to human prostate cancer cells. *International Journal of Cancer.* 2004;112:693-700.

81. Uhrich KE, Cannizzaro SM, Langer RS, Shakesheff KM. Polymeric systems for controlled drug release. *Chemical Reviews.* 1999;99(11):3181-3198.

82. Le Broc-Ryckewaert D, Carpentier R, Lipka E, Daher S, Vaccher C, Betbeder D, Furman C. Development of innovative paclitaxel-loaded small PLGA nanoparticles: study of their antiproliferative activity and their molecular interactions on prostatic cancer cells. *International Journal of Pharmaceutics.* 2013;454(2):712-719.

83. Dhar S, Kolishetti N, Lippard SJ, Farokhzad OC. Targeted delivery of a cisplatin prodrug for safer and more effective prostate cancer therapy in vivo. *PNAS.* 2011;108(5):1850-1855.

84. Shukla R, Bansal V, Chaudhary M, Basu A, Bhonde RR, Sastry M. Biocompatibility of gold nanoparticles and their endocytotic fate inside the cellular compartment: a microscopic overview. *Langmuir.* 2005;21(23):10644-10654.

85. Dreaden EC, Berkley EG, Lauren AA, Brice TD, Steven CH, Min P, Quarles LD, Adegboyega KO, Mostafa AE. Antiandrogen gold nanoparticles dual-target and overcome treatment resistance in hormone-insensitive prostate cancer cells. *Bioconjugate Chemistry.* 2012;23(8):1507-1512.

86. Li X, Wang X, Zhang J, Hanagata N, Wang X, Weng Q, Ito A, Bando Y, Golberg D. Hollow boron nitride nanospheres as boron reservoir for prostate cancer treatment. *Nature Communications.* 2017;6(8):13936.

87. Ramroop JR, Stein MN, Drake JM. Impact of phosphoproteomics in the era of precision medicine for prostate cancer image. *Frontiers in Oncology.* 2018;8:1-18.

88. Van Duin M, Peters J, Kieboom A, Van Bekkum H. Studies on borate esters 1: the pH dependence of the stability of esters of boric acid and borate in aqueous medium as studied by 11B NMR. *Tetrahedron.* 1984;40(15):2901-2911.

89. Hausdorf G, Kruger K, Kuttner G, Holzhutter HG, Frommel C, Hohne WE. Oxidation of a methionine residue in subtilisin-type proteinases by the hydrogen peroxide/borate system--an active site-directed reaction. *Biochimica et Biophysica Acta.* 1988;952(1):20-26.

90. Raven J. Short- and long-distance transport of boric acid in plants. *New Phytologist.* 1980;84(2):231-249.

91. Grill E, Himmelbach A. ABA signal transduction. *Current Opinion in Plant Biology.* 1998;1(5):412-418.

92. Ralston NVC, Hunt CD. Diadenosine phosphates and S-adenosylmethionine:novel boron binding biomolecules detected by capillary electrophoresis. *Biochimica et Biophysica Acta.* 2001;1527:20-30.

93. Loenen WAM. S-adenosylmethionine: jack of all trades and master of every-thing? *Biochemical Society Transactions.* 2006;34:330-333.

94. Scorei IR. Boron compounds in the breast cancer cells chemoprevention and chemotherapy. *Breast Cancer: Current and Alternative Therapeutic Modalities.* 2011;91-114.

95. Hakki SS, Bozkurt BS, Hakki EE. Boron regulates mineralized tissue-associated proteins in osteoblasts (MC3T3-E1). *Journal of Trace Elements in Medicine and Biology.* 2010;24(4):243-250.

96. Penland JG. Quantitative analysis of EEG effects following experimental mag-nesium and boron deprivation. *Magnesium Research.* 1995;8:341-358.

97. Hunt CD, Nielsen FH. Interaction between boron and cholecalciferol in the chick. Trace element metabolismin man and animals (TEMA-4). *Canberra: Australian Academy of Science.* 1981;597-600.

98. Hunt CD. Dietary boron modified the effects of magnesium and molybdenumon mineral metabolism in the cholecalciferol-deficient chick. *Biological Trace Element Research.* 1989;22:201-220.

99. Hegsted M, Keenan MJ, Siver F, Wozniak P. Effect of boron on vitamin D deficientrats. *Biological Trace Element Research.* 1991;28:243-255.

100. Scorei RI, Popa R. Boron-containing compounds as preventive and chemotherapeutic agents for cancer. *Anti-cancer Agents in Medicinal Chemistry.* 2010;10(4):346-351.

101. Korkmaz M, Uzgoren E, Bakirdere S, Aydin F, Ataman OY. Effects of dietary boron on cervical cytopathology and on micronucleus frequency in exfoliated buccal cells. *Environmental Toxicology.* 2007;22(1):17-25.

102. DeLuca HF. Is there more to learn about functional vitamin D metabolism? *The Journal of Steroid Biochemistry and Molecular Biology*. 2015;148:3-6.

103. Barranco WT, Eckhert CD. Boric acid inhibits human prostate cancer cell proliferation. *Cancer Letters.* 2004;216:21-29.

104. McAuley EM, Bradke TA Plopper GE. Phenylboronic acid is a more potent inhibitor than boric acid of key signaling networks involved in cancer cell migration. *Cell Adhesion and Migration.* 2011;5(5):382-386.

105. Coderre JA, Morris GM. The radiation biology of boron neutron capture therapy. *Radiation Research.* 1999;151:10-18.

106. Kawabata S, Miyatake S, Kuroiwa T, Yokoyama K, Doi A, Iida K, Miyata S, Nonoguchi N, Michiue H, Takahashi M, Inomata T, Imahori Y, Kirihata M, Sakurai Y, Maruhashi A, Kumada H, Ono K. Clinical study on modified boron neutron capture therapy for newly diagnosed glioblastoma. *Journal of Radiation Research.* 2009;50(1):51-60.

107. Barth RF, Graca M, Vicente H, Harling OK, Kiger WS, Riley KJ, Binns PJ, Wagner FM, Suzuki M, Aihara T, Kato I, Kawabata S. Current status of boron neutron capture therapy of high-grade gliomas and recurrent head and neck cancer. *Radiation Oncology.* 2012;7:146-166.

108. Cha S, Lupo JM, Chen MH, Lamborn KR, McDermott MW, Berger MS, Nelson SJ, Dillon WP. Differentiation of glioblastoma multiforme and single brain metastasis by peak height and percentage of signal intensity recovery derived from dynamic susceptibility-weighted contrast enhanced perfusion mr imaging. *American Journal of Neuroradiology.* 2007;28:1078-1084.

109. Locher GL. Biological effects and therapeutic possibilities of neutrons. *American Journal of Roentgenol Radium Therapy.* 1936;36:1-13.

110. Godwin JT, Farr LE, Sweet WH, Robertson JS. Pathological study of eight patients with glioblastoma multiforme treated by neutron-capture therapy using boron^{10}. *Cancer.* 1955;8:601-615.

111. Slatkin DN. A history of boron neutron capture therapy of brain tumors. *Brain.* 1991;114:1609-1629.

112. Asbury AK, Nielson SL, Sweet WH. Neuropathologic study of fourteen cases of malignant brain tumor treated by boron-10 slow neutron capture therapy. *Journal of Neuropathological Expression Neurology.* 1972;31:278-303.

113. Barth RF, Coderre JA, Gra M, Vicente H, Blue TE. Boron neutron capture therapy of cancer: current status and future prospects. *Clinical Cancer Research.* 2005;11:3987-4002.

114. Nakamura H, Kirihata M. Boron compounds: new candidates for boron carriers in BNCT. *Neutron Capture Therapy: Principles and Applications.* 2012; 99-116.

115. Maeda H. The enhanced permeability and retention (EPR) effect in tumor vasculature: the key role of tumor-selective macromolecular drug targeting. *Advances in Enzyme Regulation.* 2001;41:189-207.

116. Erreni M, Solinas G, Brescia P, Osti D, Zunino F, Colombo P, Destro A, Roncalli M, Mantovani A, Draghi R, Levie D, Baena RR, Gaetani P, Pelicci G, Allavena P. Human glioblastoma tumours and neural cancer stem cells express the chemokine CX3CL1 and its receptor CX3CR1. *European Journal of Cancer.* 2010;46(18):3383-3392.

117. Snyder HR, Reedy AJ, Lennarz WJ. Synthesis of aromatic boronic acids, aldehydo boronic acids and a boronic acid analog of tyrosine. *Journal of American Chemical Society.* 1958;80:835-838.

118. Soloway AH, Hatanaka H, Davis MA. Penetration of brain and brain tumor. VII.Tumor-binding sulfhydryl boron compounds. *Journal of Medicinal Chemistry.* 1967;10:714-717.

119. Hatanaka H, Karin ABMF, Laws E. Boron neutron capture therapy for brain tumors. *Springer-Verlag.* 1991;233-249.

120. Hatanaka H. Boron-neutron capture therapy for tumors. *Glioma.* 1986; 233-249.

121. Miyatake S, Kawabata S, Kajimoto Y, Aoki A, Yokoyama K, Yamada M, Kuroiwa T, Tsuji M, Imahori Y, Kirihata M, Sakurai Y, Masunaga S, Nagata K, Maruhashi A, Ono K. Clinical results of modified BNCT for malignant glioma using two boron. *Congress on Neutron Capture Therapy.* 2004;11-15.

122. Bergland R, Elowitz E, Coderre JA, Joel D, Chadha M, Mishima Y. A phase1trial of intravenous boronophenylalaninefructose complex in patients with glioblastoma multiforme. *Cancer Neutron Capture Therapy.* 1996;739-746.

123. Nedunchezhian K, Aswath N, Thiruppathy M, Thirugnanamurthy S. Boron neutron capture therapy. *Journal of Clinical and Diagnostic Research.* 2016;10(12):1-4.

124. Olsson P, Gedda L, Goike H, Liu L, Collins VP, Pontén J, Carlsson J. Uptake of a boronated epidermal growth factor-dextran conjugate in CHO xenograftswi th and without human EGF-receptor expression. *Anticancer Drug Design.* 1998;13:279-289.

125. Capala J, Barth RF, Bendayan M, Lauzon M, Adams DM, Soloway AH, Fenstermaker RA, Carlsson J. Boronated epidermal growth factor as a potential targeting agent for boron neutron capture therapy of brain tumors. *Bioconjugate Chemistry.* 1996;7(1):7-15.

126. Doi A, Kawabata S, Iida K, Yokoyama K, Kajimoto Y, Kuroiwa T, Shirakawa T, Kirihata M, Kasaoka S, Maruyama K, Kumada H, Sakurai Y, Masunaga SI, Ono K, Miyatake SI. Tumor-specific targeting of sodium borocaptate (BSH) to malignant glioma by transferrin-PEG liposomes: a modality for boron neutron capture therapy. *Journal of Neuro-Oncology.* 2008;87(3):287-294.

127. Chopra NG, Luyken RJ, Cherrey K, Crepsi VH, Cohen ML, Louie SG, Zettl A. Boron nitride nanotubes. *Science.* 1995;269:966-967.

128. S Iijima. Helical microtubules of graphitic carbon. *Nature.* 1991;354:56-58.

129. Han WQ. Anisotropic hexagonal boron nitride nanomaterials: synthesis and applications. *Biofanctionalization of Nanomaterials.* 2010.

130. Arenal R, Wang MS, Xu Z, Loiseau A Golberg D. Young modulus, mechanical and electrical properties of isolated individual and bundled single-walled boron nitride nanotubes. *Nanotechnology.* 2011;22(26):265704.

131. X Chen, P Wu, M Rousseas, D Okawa, Z Gartner, CR Zettl, A Bertozzi. Boron nitride nanotubes are noncytotoxic and can be functionalized for interaction with proteins and cells. *Journal of the American Chemical Society.* 2009;131:890-891.

132. Kim JH, Pham TV, Hwang JH, Kim CS, Kim MJ. Boron nitride nanotubes: synthesis and applications. *Nano Convergence.* 2018;5(17):1-13.

133. Lahiri D, Singh V, Benaduce AP, Seal S, Kos A, Agarwala L. Boron nitride nanotube reinforced hydroxyapatite composite: mechanical and tribological performance and in-vitro biocompatibility to osteoblasts. *Journal of the Mechanical Behavior of Biomedical Materials.* 2011;4(1):44-56.

134. Islam MS, Kouzani AZ, Dai XJ, Michalski WP. Design and analysis of a cantilever biosensor based on a boron nitride nanotube. *TENCON Proceedings of the 2010 IEEE Region 10 Conference;*2010:IEEE, Piscataway.

135. Raffa V, Ciofani A, Cuschieri G. Enhanced low voltage cell electropermeabilization by boron nitride nanotubes. *Nanotechnology.* 2009;20(7):075104.

136. Gao Z, Zhi C, Golberg D, Takeshi BY. Noncovalent functionalization of boron nitride nanotubes in aqueous media. *Nanobiomedicine.* 2014;1:7-20.

137. Ferreira TH, Sousa EMB. Applications and perspectives of boron nitride nanotubes in cancer therapy. *Boron Nitride Nanotubes in Nanomedicine*. 2016;95-109.

138. Ciofani G, Turco SD, Genchi GG, D'Alessandro D, Basta G, Mattoli V. Transferrin-conjugated boron nitride nanotubes: Protein grafting, characterization, and interaction with human endothelial cells. *International Journal of Pharmaceutics.* 2012;436(2):444-453.

139. Nakamura H, Koganei H, Miyoshi T, Sakurai Y, Ono K, Suzuki M. Antitumor effect of boron nitride nanotubes in combination with thermal neutron irradiation on BNCT. *Bioorganic and Medicinal Chemistry Letters.* 2015;25(2):172-174.

140. Ciofani G, Raffa V, Menciassi A, Cuschieri A. Folate functionalized boron nitride nanotubes and their selective uptake by glioblastoma multiforme cells: implications for their use as boron carriers in clinical boron neutron capture therapy. *Nanoscale Research Letters.* 2008;4:113-121.

141. Kalay S, Yilmaz Z, Sen O, Emanet M, Kazanc E, Çulha M. Synthesis of boron nitride nanotubes and their applications. *Beilstein Journal of Nanotechnology.* 2015;6:84-102.

142. Golberg, D, Han, W, Bando, Y, Bourgeois L, Kurashima K, Sato T.J. Fine structure of boron nitride nanotubes produced from carbon nanotubes by a substitution reaction. *Journal of Applied Physics.* 1999;86(4):2364-2366.

143. Golberg D, Bando Y, Eremets M, Takemura K, Kurashima K, Yusa H. Nanotubes in boron nitride laser heated at high pressure. *Applied Physics Letters.* 1996;69:2045-2047.

144. Lourie OR, Jones CR, Bartlett MB, Gibbons PC, Ruoff RS, Buhro WE. CVD growth of boron nitride nanotubes. *Chemical Materials.* 2000;12:1808-1810.

145. Pakdel A, Zhi C, Bando Y, Nakayama N, Golberg D. A comprehensive analysis of the CVD growth of boron nitride nanotubes. *Nanotechnology.* 2012;23:215601.

146. Chen H, Chen Y, Liu Y, Fu L, Huang C, Llewellyn D. Over 1.0 mm-long boron nitride nanotubes. *Chemical Physical Letters.* 2008;463:130-133.

147. Kalay S, Yilmaz Z, Çulha M. Synthesis of boron nitride nanotubes from unprocessed colemanite. *Beilstein Journal of Nanotechnology.* 2013;4:843-851.

148. Li Y, Chen LH. Superhydrophobic properties of nonaligned boron nitride nanotube films. *Langmuir.* 2010;26:5135-5140.

149. Li LH, Chen AM, Glushenkova Y. Boron nitride nanotube films grown from boron ink painting. *Journal of Materials Chemistry.* 2010;20(43):9679-9683.

150. Lee CH, Bhandari S, Tiwari B, Yapici N, Zhang D Yap YK. Boron nitride nanotubes: Recent advances in their synthesis, functionalization, and applications. *Molecules.* 2016;21(7):922-941.

151. Ciofani G, del Turco S, Rocca A, Vito G, Cappello V, Yamaguchi M, Li X, Mazzolai B, Basta G, Gemmi M, Piazza V, Golberg V, Mattoli D. Cytocompatibility evaluation of gum Arabic-coated ultra-pure boron nitride nanotubes on human cells. *Nanomedicine.* 2014;9:773-788.

152. Lau YTR, Yamaguchi M, Li X, Bando Y, Golberg D, Winnik FM. Facile and mild strategy toward biopolymer-coated boron nitride nanotubes via a glycine-assisted interfacial process. *The Journal of Physical Chemistry C.* 2013;117(38):19568-19576.

153. Li X, Zhi C, Hanagata N, Yamaguchi M, Bando Y, Golberg D. Boron nitride nanotubes functionalized with mesoporous silica for intracellular delivery of chemotherapy drugs. *Chemical Communications.* 2013;49:7337-7339.

154. Li X, Hanagata N, Wang X, Yamaguchi M, Yi W, Bando Y, Golberg D. Multimodal luminescent-magnetic boron nitride nanotubes@$NaGdF_4$:Eu structures for cancer therapy. *Chemical Communications.* 2014;50(33):4371-4374.

155. Ciofani G, Raffa V, Menciassi A, Cuschieri A. Cytocompatibility, interactions, and uptake of polyethyleneimine-coated boron nitride nanotubes by living cells: confirmation of their potential for biomedical applications. *Biotechnology and Bioengineering.* 2008;101(4):850-858.

156. Ciofani G, Del Turco S, Genchi GG, D'Alessandro D, Basta V, Mattoli G. Transferrin-conjugated boron nitride nanotubes: protein grafting, characterization, and interaction with human endothelial cells. *International Journal of Pharmaceutics.* 2012;436(2):444-453.

157. Ciofani G, Danti S, D'Alessandro D, Moscatoc A, Menciassi S. Assessing cytotoxicity of boron nitride nanotubes: Interference with the MTT assay. *Biochemical and Biophysical Research Communications.* 2010;394(2):405-411.

158. Ferreira TH, Soares DCF, Moreira LMC, Silva PRO, Santos EMB, Sousa RG. Boron nitride nanotubes coated with organic hydrophilic agents: Stability and cytocompatibility studies. *Materials Science and Engineering C-Materials for Biological Applications.* 2013;33:4616-4623.

159. Ferreira T, Silva PRO, Santos EMB, Sousa RG. A novel synthesis route to produce boron nitride nanotubes for bioapplications. *Journal of Biomaterials and Nanobiotechnology*. 2011;2:426-434.

160. Horvath L, Magrez A, Golberg D, Chunyi Z, Bando Y, Samajda R, Horvath E, Forro L, Schwaller B, In vitro investigation of the cellular toxicity of boron nitride nanotubes. *ACS Nano.* 2011;5(5):3800-3810.

161. Ciofani G, Danti S, Genchi GG, D'Alessandro D, Pellequer JL, Odorico M, Mattoli V, Giorgi M. Pilot in vivo toxicological investigation of boron nitride nanotubes. *International Journal of Nanomedicine.* 2012;7:19-24.

162. Ciofani G, Danti S, Nitti S, Mazzolai B, Mattoli V, Giorgi M. Biocompatibility of boron nitride nanotubes: an up-date of in vivo toxicological investigation. *International Journal of Pharmaceutics.* 2013;444(2):85-88.

163. Salwetti A, Rossi L, Iacopetti P, Li X, Nitti S, Pellegrino T, Mattoli V, Golberg D, Ciofani G. In vivo biocompatibility of boron nitride nanotubes: effects on stem cell biology and tissue regeneration in planarians. *Nanomedicine.* 2015;10(12):1911-1922.

164. Arenal R, Bezanilla AL. Boron nitride materials: an overview from 0D to 3D (nano) structures. *Wiley Interdisciplinary Reviews: Computational Molecular Science.* 2015;5(4):299-309.

165. Lipp A, Schwetz KA, Hunold K. Hexagonal boron nitride: fabrication, properties and applications. *Journal of the European Ceramic Society.* 1989;5(1):3-9.

166. Han WQ. Anisotropic hexagonal boron nitride nanomaterials: synthesis and applications. *Nanotechnologies for the Life Sciences.* 2010;411-461.

167. Hart JN, Allan NL Claeyssens F. Predicting crystal structures ab initio: group 14 nitrides and phosphides. *Physical Chemistry Chemical Physics.* 2010;12(30):8620-8631.

168. Cumings J, Zettl A. Mass-production of boron nitride double-wall nanotubes and nanococoons. *Chemical Physics Letters.* 2000;316:211-216.

169. Wood GL, Janik JF, Pruss EA, Dreissig D, Kroenke WJ, Habereder T, Noth H, Paine RT. Aerosol synthesis of spherical morphology boron nitride powders from organoborate precursors. *Chemical Materials.* 2006;18:1434-1442.

170. Tang C, Bando Y, Huang Y, Zhi C, Golberg D. Synthetic routes and formation mechanisms of spherical boron nitride nanoparticles. *Advanced Functional Materials.* 2008;18:3653-3661.

171. Lian G, Zhang X, Zhu L, Tan M, Cui D, Wang Q. A facile solid-state reaction route towards nearly monodisperse hexagonal boron nitride nanoparticles. *Journal of Materials Chemistry.* 2010;20:3736-3742.

172. Suryavanshi U, Balasubramanian VV, Lakhi KS, Mane GP, Ariga K, Choy J, Park DH, Al-Enizid AM, Vinu A. Mesoporous BN and BCN nanocages with high surface area and spherical morphology. *Physical Chemistry Chemical Physics.* 2014;16:23554-23557.

173. Russier J, Ménard-Moyon C, Venturelli E, Gravel E, Marcolongo G, Meneghetti M, Doris E, Bianco A. Oxidative biodegradation of single- and multiwalled carbon nanotubes. *Nanoscale.* 2011;3:893-896.

174. Sam S, Touahir L, Andresa JS, Allongue P, Chazalviel JN, Gouget-Laemmel AC, Henry de Villeneuve C, Moraillon A, Ozanam F, Gabouze N, Djebbar S. Semiquantitative study of the EDC/NHS activation of acid terminal groups at modified porous silicon surfaces. *Langmuir.* 2010;26(2):809-814.

175. Bhatia S. Nanoparticles types, classification, characterization, fabrication methods and drug delivery applications. *Natural Polymer Drug Delivery Systems.* 2016;33-93.

176. Reimer L. *Scanning electron microscopy: physics of image formation and microanalysis.* Springer; 1998.

177. Falqui A, Rodighiero S, Sogne E, Torre B, Ruffilli R, Francolini M, Cagnoli C, Fabrizio E. Indium-tin-oxide (ITO) as stable and effective coating material for correlative confocal and immuno-scanning electron microscopy studies. *Microscopy and Microanalysis.* 2015;21:1501-1502.

178. Williams DB, Carter CB. The transmission electron microscope. *Transmission Electron Microscopy.* 1996;3-17.

179. Burghardt RC, Droleskey R. Transmission electron microscopy. *Current Protocols.* 2006;3(1):1-39.

180. Meyer E. Atomic force microscopy. *Progress in Surface Science.* 1992;41(1):3-49.

181. Förster H. UV/VIS Spectroscopy. *Characterization.* 2004;337-426.

182. Barth A. Infrared spectroscopy of proteins. *Biochimica et Biophysica Acta*. 2007;1767(9):1073-1101.

183. Colthup N. *Introduction to Infrared and Raman Spectroscopy.* Academic Press; 2012.

184. Holthoff H, Egelhaaf SU, Borkovec M, Schurtenberger P, Sticher H. Coagulation rate measurements of colloidal particles by simultaneous static and dynamic light scattering. *Langmuir.* 1996;12 (23):5541-5549.

185. Chen X, Wu P, Rousseas M, Okawa D, Gartner Z, Zettl A, Bertozzi CR. Boron nitride nanotubes are noncytotoxic and can be functionalized for interaction with proteins and cells. *Journal of the American Chemical Society.* 2009;131(3):890-891.

186. Li L, Li LH, Ramakrishnan S, Dai XJ, Nicholas K, Chen Y, Chen Z, Liu X. Controlling wettability of boron nitride nanotube films and improved cell proliferation. *The Journal of Physical Chemistry C.* 2012;116:18334-18339.

187. Kang B, Opatz T, Landfester K, Wurm FR. Carbohydrate nanocarriers in biomedical applications: functionalization and construction. *Chemical Society Reviews.* 2015;44:8301-8325.

188. Zhang X, Zhu Y, Li J, Zhu Z, Li J, Li Q, Huang W. Tuning the cellular uptake and cytotoxicity of carbon nanotubes by surface hydroxylation. *Journal of Nanoparticle Research.* 2011;13:6941-6952.

189. Bae YS, Oh H, Rhee SG, Yoo YD. Regulation of reactive oxygen species generation in cell signaling. *Molecules and Cells.* 2011;32(6):491-509.

190. Christen Y. Oxidative stress and Alzheimer disease. *The American Journal of Clinical Nutrition.* 2000;71(2):621-629.

191. Bustos-Obregn E, Goicochea RI. Pesticide soil contamination mainly affects earthworm male reproductive parameters. *Asian Journal of Andrology.* 2002;4:195-199.

192. Lesage G, Bussey H. Cell wall assembly in Saccharomyces cerevisiae. *Microbiology and Molecular Biology Reviews.* 2006;70(2):317-343.

193. Kollár R, Reinhold BB, Petráková E, Yeh HJC, Ashwell G, Drgonová J, Kapteyn JC, Klis FM Cabib E. Architecture of the yeast cell wall β(1→6)-glucan interconnects mannoprotein, β(1→3)-glucan, and chitin. *The Journal of Biological Chemistry.* 1997;272:17762-17775.

194. Wang B, Liu P, Jiang W, Pan H, Xu X, Tang R. Biomimetic construction of cellular shell by adjusting the interfacial energy. *Biotechnology and Bioengineering.* 2014;111(2):386-395.

195. Zhang Y, Chen Y, Westerhoff P, Hristovski K, Crittenden JC. Stability of commercial metal oxide nanoparticles in water. *Water Research.* 2008;42:2204-2212.

196. Salvetti A, Rossi L, Iacopetti P, Li X, Nitti S, Pellegrino T, Mattoli V, Golberg D, Ciofani G. In vivo biocompatibility of boron nitride nanotubes: effects on stem cell

biology and tissue regeneration in planarians. *Nanomedicine.* 2015;10(12):1911-1922.

197. Yousefpour P, Atyabi F, Farahani EV, Sakhtianchi R, Dinarvand R. Polyanionic carbohydrate doxorubicin-dextran nanocomplex as a delivery system for anticancer drugs: in vitro analysis and evaluations. *International Journal of Nanomedicine.* 2011;6:1487-1496.

198. Liu Z, Sun X, Nakayama-Ratchford N, Dai H. Supramolecular chemistry on water-soluble carbon nanotubes for drug loading and delivery. *ACS Nano.* 2007;1(1):50-56.

199. Beijnen J, Van Der Houwen O, Underberg W. Aspects of the degradation kinetics of doxorubicin in aqueous solution. *International Journal of Pharmaceutics.* 1986;32(2):123-131.

200. Kaushik D, Bansal G. Four new degradation products of doxorubicin: an application of forced degradation study and hyphenated chromatographic techniques. *Journal of Pharmaceutical and Biomedical Analysis.* 2015;5(5):285-295.

201. Ali-Boucetta H, Al-Jamal KT, Mccarthy D, Prato M, Bianco A, Kostarelos K. Multiwalled carbon nanotube-doxorubicin supramolecular complexes for cancer therapeutics. *Chemical Communications.* 2008;4:459-461.

202. Li J, Pant A, Chin CF, Ang WH, Ménard-Moyon C, Nayak TR, Gibson D, Ramaprabhu S, Panczyk T, Bianco A, Pastorin G. In vivo biodistribution of platinum-based drugs encapsulated into multi-walled carbon nanotubes. *Nanomedicine.* 2014;10(7):1465-1475.

203. Manocha B, Margaritis A. Controlled release of doxorubicin from doxorubicin/γ-polyglutamic acid ionic complex. *Journal of Nanomaterials.* 2010;12:1-9.

204. Mindell JA. Lysosomal acidification mechanisms. *Annual Review of Physiology.* 2012;74:69-86.

205. Bright GR, Fisher GW, Rogowska J, Taylor DL. Fluorescence ratio imaging microscopy: temporal and spatial measurements of cytoplasmic pH. *The Journal of Cell Biology*. 1987;104(4):1019-1033.

206. Patra CR, Bhattacharya R, Mukherjee P. Fabrication and functional characterization of gold nanoconjugates for potential application in ovarian cancer. *Journal of Materials Chemistry*. 2010;20(3):547-554.

207. Ponka P, Lok CN. The transferrin receptor: role in health and disease. *The International Journal of Biochemistry & Cell Biology*. 1999;31:1111-1137.

208. Lee, SE Moore JK, Holmes A, Umezu K, Kolodner RD, Haber JE. Saccharomyces Ku70, Mre11/Rad50, and RPA Proteins Regulate Adaptation to G2/M Arrest after DNA Damage. *Cell.* 1998;94(3):399-409.

209. Murphy MP. How mitochondria produce reactive oxygen species. *Biochemical Journal.* 2009;417:1-13.

210. Fink SL, Cookson BT. Apoptosis, pyroptosis, and necrosis: Mechanistic description of dead and dying eukaryotic cells. *Infection and Immunity.* 2005;73(4):1907-1916.

211. Itoh G, Tamura J, Suzuki M, Suzuki Y, Ikeda H, Koike M, Nomura M, Jie T, Ito K. DNA fragmentation of human infarcted myocardial cells demonstrated by the nick end labeling method and DNA agarose gel electrophoresis. *The American Journal of Pathology.* 1995;146(6):1325-1331.

212. Friedl P, Wolf K. Tumor-cell invasion and migration: diversity and escape mechanisms. *Nature Reviews Cancer*. 2003;3:362-374.

213. Ito T, Erdmann KS, Roux A, Habermann B, Werner H, De Camilli P. Dynamin and the actin cytoskeleton cooperatively regulate plasma membrane invagination by bar and f-bar proteins. *Developmental Cell.* 2005;9(6):791-804.

214. Emanet M, Sen Ö, Cobandede Z, Culha M. Interaction of carbohydrate modified boron nitride nanotubes with living cells. *Colloids and Surfaces B: Biointerfaces.* 2015;134:440-446.

215. Emanet M, Fakhrullin R, Culha. Boron nitride nanotubes and layer-by-layer polyelectrolyte coating for yeast cell surface engineering. *ChemNanoMat*. 2016;2:426-429.

216. Emanet M, Şen Ö, Çulha M. Evaluation of boron nitride nanotubes and hexagonal boron nitrides as nanocarriers for cancer drugs. *Nanomedicine.* 2017;12(7):797-810.

217. Sen Ö, Emanet M, Çulha M. Biocompatibility evaluation of boron nitride nanotubes. *Boron Nitride Nanotubes in Nanomedicine.* 2016;41-55.